

**High-resolution X-ray spectral
diagnostics of shell type
Supernova Remnants**

Cover : “Starry Night” by Vincent van Gogh
With thanks to Joeri van Leeuwen

High-resolution X-ray spectral diagnostics of shell type Supernova Remnants

Röntgen-spectraaldiagnostiek met hoog scheidend vermogen van
schil-type supernovarestanten
(met een samenvatting in het Nederlands)

Proefschrift

ter verkrijging van de graad van doctor aan
de Universiteit Utrecht op gezag van de
Rector Magnificus, Prof. Dr. W.H. Gispen, ingevolge
het besluit van het College voor Promoties in het
openbaar te verdedigen op
maandag 2 februari 2004 des middags te 2.30 uur

door

Kurt Josias van der Heyden
geboren op 30 oktober 1971, te Kimberley (Zuid Afrika)

promotor : Prof. Dr. Ir. J.A.M. Bleeker
Faculteit Natuur- en Sterrenkunde, Universiteit Utrecht

co-promotor : Dr. J.S. Kaastra
Stichting Ruimteonderzoek Nederland

Contents

1	Introduction	1
1.1	Motivation	1
1.2	SNR progenitors	2
1.3	SNR evolution	4
1.4	Thermal X-ray Emission	5
1.5	Thesis Outline	7
2	<i>XMM-Newton</i> & High Resolution Spectroscopy	11
2.1	<i>XMM-Newton</i>	11
2.1.1	Reflection Grating Spectrometer	12
2.2	Plasma diagnostics	14
2.2.1	He-like ions	17
2.2.2	Elemental Abundance	20
2.2.3	Thermal Doppler Broadening	23
2.2.4	Optical Depth Effect	24
2.3	Accuracy of atomic physics	25
3	Cassiopeia A: on the origin of the hard X-ray continuum and the implication of the observed O VIII Ly-α/Ly-β distribution	29
3.1	Introduction	30
3.2	Observations	30
3.3	The hard X-ray data	31
3.3.1	The X-ray spectrum above 4.0 keV	31
3.3.2	X-ray images above 4.0 keV	34
3.3.3	The Fe K emission	34
3.3.4	Discussion	35
3.4	High-resolution spectroscopic data	36

3.4.1	Analysis & results	36
3.4.2	Discussion	38
4	X-ray spectral imaging and Doppler mapping of Cassiopeia A	41
4.1	Introduction	42
4.2	Spectral Fitting Analysis	43
4.3	Doppler mapping	45
4.4	Key results	48
4.5	Ionisation structure and abundance ratios	52
4.6	Dynamics	53
4.7	Discussion	58
5	Detection of X-ray line emission from the shell of SNR B 0540–69.3 with <i>XMM-Newton</i> <i>RGS</i>	63
5.1	Introduction	63
5.2	Observations & Data Reduction	64
5.3	Analysis and Results	65
5.3.1	Location of emitting region	65
5.3.2	Spectral analysis	66
5.4	Discussion	68
5.5	Conclusions	73
6	High-Resolution X-ray imaging and spectroscopy of N 103B	75
6.1	Introduction	76
6.2	Observation and Data Reduction	76
6.3	Data Analysis	77
6.3.1	<i>XMM-Newton</i> Spectra	77
6.3.2	<i>Chandra</i> Images	81
6.4	Discussion	83
6.4.1	Ionisation equilibrium	83
6.4.2	Density, age, and dynamics	88
6.4.3	Elemental abundances and type of progenitor	89
6.5	Summary & Conclusions	91
7	High resolution spectroscopy and emission line imaging of DEM L 71 with <i>XMM-Newton</i>	95
7.1	Introduction	96
7.2	Observation and Reduction	96
7.3	Analysis and Results	97

7.3.1	Spectra	97
7.3.2	Monochromatic images and single ion spectroscopy . . .	102
7.4	Discussion	105
7.4.1	Single Ion Spectroscopy	105
7.4.2	Abundances & Morphology	108
7.4.3	Mass estimates	109
7.5	Summary & Conclusions	110
8	Synoptic study of the SMC SNRs using <i>XMM-Newton</i>	113
8.1	Introduction	114
8.2	Observations and Reduction	114
8.3	Analysis and Results	115
8.3.1	Images	115
8.3.2	Spectral Analysis	116
8.4	Discussion	123
8.4.1	Progenitor Types	123
8.4.2	SMC Abundances	132
8.4.3	Physical parameters	132
8.4.4	Comments on SMC SN rates	134
9	Summary & Outlook	137
9.1	Synopsis	137
9.1.1	Cassiopeia A	138
9.1.2	The LMC SNRs	140
9.1.3	The SMC SNRs	141
9.2	Outlook	142
10	Nederlandse Samenvatting	147
10.1	Supernova's en Supernovarestanten	147
10.2	Dit proefschrift: Röntgenstraling van supernovarestanten	149

Chapter 1

Introduction

1.1 Motivation

Supernova remnants (SNRs) are intriguing because they relate many fields of physics and astrophysics. SNR investigations improve our understanding of fundamental physical phenomena such as collisionless shocks, hydrodynamical instabilities and equilibration in ionising plasmas.

There are three dominant physical processes expected to produce X-rays in an astrophysical setting, viz. thermal emission from a hot gas, synchrotron emission from relativistic electrons and blackbody radiation. All three mechanisms are encountered in the study of SNRs. Thermal X-rays are emitted after a shock wave from the supernova (SN) explosion heats the circumstellar gas, either the SN precursor's material or interstellar matter. Synchrotron emission is detected when electrons spiral around the compressed magnetic field in the SNR shell and/or pulsar wind nebulae. Blackbody radiation is expected from a newly formed, hot neutron star. The spectral signature of each mechanism is unique and can be readily detected using high-quality spectra.

The major focus of this thesis is on the thermal X-ray emission. This is an important part of SNR studies as most of the initial mechanical energy is radiated as thermal X-ray emission. The shocked environment and the interface between hot and cold gas give rise to X-ray plasma conditions unique to SNRs. Transient non-equilibrium ionisation (NEI) plasmas are expected to occur due to the low density and corresponding long average collision time. They have been unambiguously detected in young SNRs (e.g. N103B; chapter 6). Among

the most conspicuous spectroscopic manifestations of NEI plasmas are emission from open-shell ionic species and spectral lines that arise from inner-shell excitation and ionisation. These features are marginal in ionisation equilibrium plasmas. Along with high resolution imaging, spectroscopic measurements of SNRs provide many details on the emission mechanism, chemical structure, the ionisation state, and the atomic processes, which govern its behavior.

1.2 SNR progenitors

Supernova remnants are by definition the remains of exploded stars. Historically the supernova explosions leading to the SNRs have been divided into two classes based on their optical spectra. The basis for the classification consists of the presence (type II) or absence (type I) of H lines in the spectrum near maximum light. The light-curve also carries important information. Type I events display similar lightcurves, suggesting a common progenitor type. The intensity rises quickly to maximum ($\sim 10^9 L_{\odot}$) in about two weeks and then falls exponentially with a characteristic time of ≈ 55 days due to the radioactive decay of ^{56}Ni ($\rightarrow^{56}\text{Co} \rightarrow^{56}\text{Fe}$). Type II SNe rise more slowly to a maximum and are generally 2 magnitudes less luminous. The maximum is broader and the decay occurs on less regular timescales. The great variety in characteristics of type II SNe implies a diversity in the progenitor stars or explosion characteristics. Together with the fact that type II SNe are predominantly seen in spiral galaxies, these differences imply that the progenitors of type II SNe are massive stars and are associated with ongoing star formation.

The current basic SN classification scheme, as shown in Fig. 1.1, is also based on the optical spectra. Subclasses of type I have been identified and are distinguished by the presence or absence of Si and He lines (see Harkness & Wheeler 1990).

Type II SNe are the result of the core collapse of massive stars ($> 8 M_{\odot}$). At the end of its lifetime ($\approx 10^6$ yr) the star is stratified into onion-like layers. The central core is composed of Fe, which is surrounded by a shell of Si and S, then a shell of Ne and O, followed by shells of C, He and H in the outermost shell. When the core contains essentially just Fe, it has nothing left to fuse. Fusion in the core ceases and gravity eventually overwhelms the electron pressure. Within milliseconds the core collapses until nuclear density is reached. The repulsive force between the nuclei overcomes the force of gravity, and the core recoils out in an explosive shock wave. As the shock encounters material in the star's outer layers, the material is heated, fusing to form new elements and radioactive

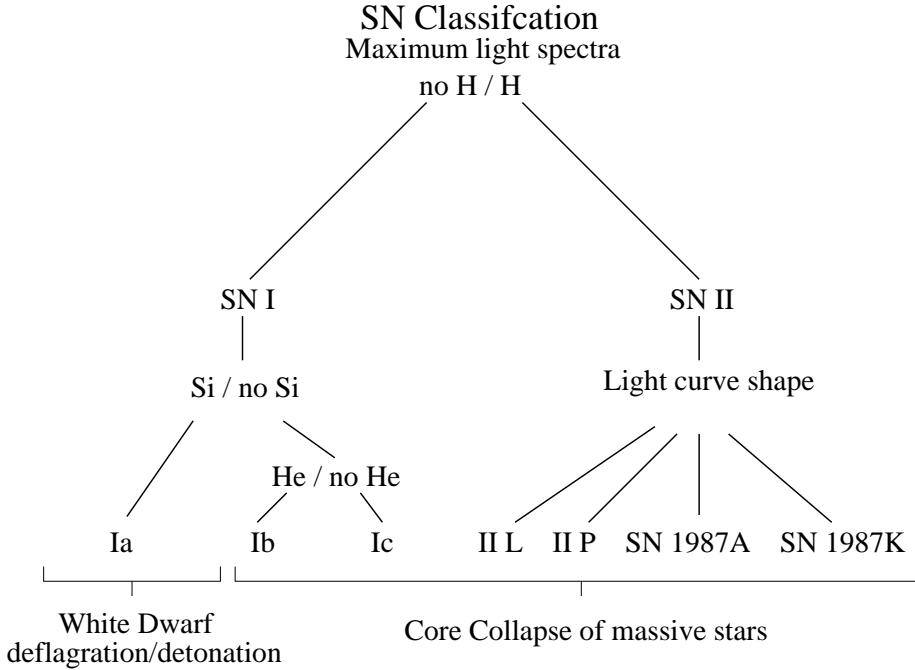


Figure 1.1: Classification scheme of supernovae (Harkness & Wheeler 1990).

isotopes (i.e. explosive nucleosynthesis). The shock then propels the matter out into space. A neutron star or black hole is left as stellar remnant.

Type Ia supernovae are due to low-mass, old population stars with a zero-age main sequence (ZAMS) mass of $4\text{--}6 M_{\odot}$. There are observational and theoretical indications that type Ia SNe are thermonuclear explosions of accreting white dwarfs (e.g. Nomoto et al. 1997), however, the exact binary evolution has not been identified. Material is accreted onto the white dwarf until the mass is sufficiently high for gravity to overcome the resistance of the degenerate electron gas. The resulting collapse raises the temperature to levels hot enough to fuse C and O in core. This creates a deflagration wave, i.e. an explosion which proceeds without initiation by a shock wave. The deflagration wave propagates through the core in seconds, resulting in nuclear fusion reactions, which creates about a solar mass of radioactive ^{56}Ni (which decays to ^{56}Fe). The details of the explosion mechanism are exceedingly complicated involving turbulent

burning and the possible transition from deflagration (sub-sonic burning front) to detonation (a super-sonic shock wave). The explosion completely disrupts the star and no stellar remnant is left.

Type Ib or type Ic events, by contrast, appear to take place when more massive stars, typically with ZAMS masses $> 20 M_{\odot}$, somehow rid themselves of their outer, hydrogen-rich layers before blowing themselves up in a qualitatively similar manner to type II events. Possible progenitors are Wolf-Rayet stars that have shed their outer hydrogen envelope in their massive stellar wind (e.g. Conti et al. 1983) or stars that have lost their hydrogen envelopes due to mass transfer in a massive interacting binary system (Uomoto 1986). The stellar remnant remaining after the explosion could be a neutron star or possibly a black hole. The ejecta contain more Fe than type II SNe, but are dominated by O.

1.3 SNR evolution

The evolution of a supernova remnant begins when the ejecta from the supernova begin to interact with the surrounding circumstellar or interstellar medium (CSM or ISM). Indeed, if there were no surrounding medium then the ejecta would steadily cool as internal energy is converted to kinetic energy by adiabatic expansion. A SN explosion transmits about 10^{44} J of kinetic energy into the surrounding medium, consequently driving a shockwave (blastwave) into the CSM/ISM. The high pressure behind the blastwave in turn drives a reverse shock (in a co-moving frame) back into the ejecta (McKee 1974). The two shock regions are separated by a contact discontinuity, which is subject to Rayleigh-Taylor instabilities (Gull 1975).

The standard evolutionary picture of supernova remnants expanding in a uniform medium has four phases, as illustrated in Fig. 1.2. In the first stage (free expansion phase) the stellar ejecta expand unimpeded as the ISM/CSM has a very low density. This phase is characterised by the fact that the mass of the swept-up ISM is much smaller than the ejecta mass. The shock velocity is nearly constant during this phase and the SNR radius thus expands linearly with time.

During the next phase (adiabatic expansion or Sedov phase) the swept-up mass is larger than the ejected mass. This is an energy conserving phase in which the integrated energy loss due to radiation is small compared to the initial explosion energy. The expansion velocity decreases during this phase due to the increasing amount of swept-up ISM material. The adiabatic solution of

SNR evolution (Sedov 1959) gives $v \propto t^{-0.6}$, $r \propto t^{0.4}$, $T \propto t^{-1.2}$, $L \propto t^{0.6}$ for $T \gtrsim 2 \times 10^7$ K and $L \propto t^{1.2}$ for $T \lesssim 2 \times 10^7$ K. Here v is the shock velocity, t is time, r is the SNR radius, T is the mean plasma temperature and L is the X-ray luminosity. This shows the rapid cooling of the shock while the luminosity increases with time. These parameters also depend upon the initial explosion energy E and the instellar density n . Scaling laws show that for a fixed age $r \propto (E/n)^{0.2}$, $T \propto (E/n)^{0.4}$ and $L \propto n^{1.8} E^{0.2}$ for high temperatures ($T \gtrsim 2 \times 10^7$ K) and $L \propto n^{2.2} E^{-0.2}$ for low temperatures ($T \lesssim 2 \times 10^7$ K). The temperature and luminosity are not a strong function of explosion energy in this phase, but the X-ray luminosity is strongly related to the interstellar density.

During the third phase (snowplow or momentum conserving phase) radiative cooling contributes significantly to the reduction of the total shock energy. The radiative losses cause the gas behind the shock to cool rapidly and the expansion slows. Most of the remnants mass compresses into a thin, dense shell. In this phase the temperature is too low to produce X-rays. The same holds for the final phase (dispersal) when the shock velocity decreases so strongly that it becomes comparable to the sound speed of the local ISM.

One has to bear in mind though that SNRs do not interact with uniform ISM/CSM media and are generally not spherical. Different dynamical stages may thus occur simultaneously within a single remnant. This complexity limits our ability to decipher, both observationally and theoretically, critical issues such as age determination, initial explosion energy estimates and dynamics.

1.4 Thermal X-ray Emission

The thermal X-ray emission from SNRs arises from the optically thin, highly ionised plasma. The SNR shock instantaneously heats the plasma to temperatures $> 10^7$ K and at the same time compresses the gas to a density of $\gtrsim 4$ times the pre-shock density. This sudden change in temperature results in a deviation from a steady-state equilibrium and the plasma is considered to be in a transient state. The ionisation balance lags behind the temperature changes and as a result the plasma is under-ionised compared to the equilibrium state corresponding to the shock temperature. This has dramatic effects on the emergent X-ray spectrum. The plasma initially radiates thermal bremsstrahlung characteristic of the high temperature together with line emission (plus two-photon and free-bound emission) characteristic of the non-equilibrium ionisation structure. The line spectrum is therefore much softer than the bremsstrahlung continuum and as the gas ionises, the NEI enhancement of the soft X-rays will eventually

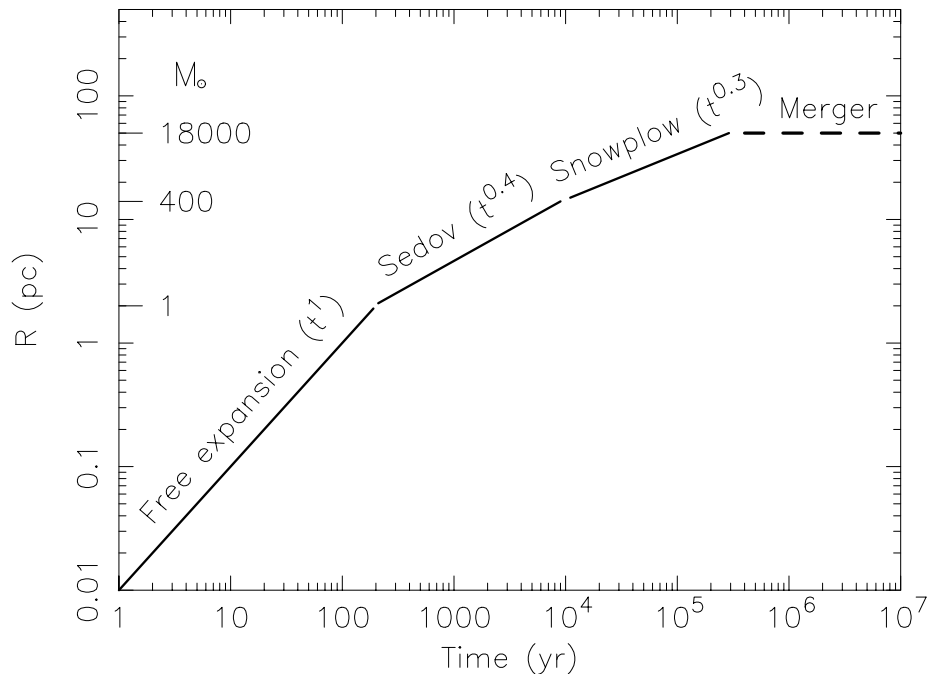


Figure 1.2: Schematic view of the explosion of a 10^{44} J supernova into a uniform medium of hydrogen density, $n_0 = 10^6 \text{ m}^{-3}$. The vertical axis shows the radius of the remnant in pc and the amount of swept-up material in solar mass (M_{\odot}). The horizontal axis shows the time after the explosion. Adapted from Cioffi (1990).

disappear, with spectral hardening occurring along the way.

The line emission that dominates the soft X-ray spectrum comes mainly from excitation by the impact of a free electron of an electronic transition between bound levels within a highly ionised atom, followed by the spontaneous radiative decay from the upper line level. The overall appearance of the X-ray spectrum will be dominated by the ionisation structure. The rate of change of the population density $N_{Z,z}$ of ion Z^{+z} from an element of atomic number Z is given by

$$\frac{dN_{Z,z}}{n_e dt} = N_{Z,z-1}S_{Z,z-1} - N_{Z,z}(S_{Z,z} + \alpha_{Z,z}) + N_{Z,z+1}\alpha_{Z,z+1}, \quad (1.1)$$

where $S_{Z,z}$ and $\alpha_{Z,z}$ are the total ionisation ($z \rightarrow z + 1$) and recombination ($z \rightarrow z - 1$) rate coefficients of ion Z^{+z} . In the case of a steady-state equilibrium the rate of change (left-hand side of eq. 1.1) can be set to zero. The main parameter that characterises the non-equilibrium state, however, is the time integral of the electron density $\int_0^t n_e dt \simeq n_e t$, also known as the ionisation parameter. X-ray emitting plasmas are out of equilibrium typically for $n_e t < 10^{18} - 10^{19} \text{ m}^{-3} \text{ s}$. Fig. 1.3 shows the evolution of the X-ray spectrum as a function of $n_e t$. More detailed discussions of NEI effects in SNRs are given by Shapiro & Moore (1976), Hamilton et al. (1983), Gronenschild & Mewe (1982), Itoh (1984) and Mewe (1984).

1.5 Thesis Outline

The launch of *XMM-Newton* and *Chandra* has brought with it, for the first time, the ability to spectroscopically detect a wide variety of physical effects, from essentially all types of cosmic X-ray sources. In this thesis advantages gained from the high sensitivity and spectral resolution of the instruments aboard *XMM-Newton* are exploited to probe the physical conditions and dynamics of SNRs. The objective of this study is not only to extend our knowledge of individual supernova remnants, but also to investigate the presence and potential of certain diagnostics which were not detectable with previous low spectral resolution instruments. While non-thermal SNRs are interesting X-ray emitters, there is little spectral structure to investigate with the high spectral resolution instruments currently available, given the featureless powerlaw spectrum. The focus of this thesis is, therefore, on the thermal emission.

A description of the *XMM-Newton* observatory is given in chapter 2, in particular the assesment of the suitability of the *RGS* for high resolution studies of SNRs. Spectroscopic diagnostics of interest are elaborated and the resolving power required to unlock these diagnostic potentials are derived. Subsequently the requirements are placed in the context of the spectroscopic capabilities of the *RGS*.

The medium resolution spatially resolved spectroscopy of Cassiopeia A with the solid state (*EPIC-MOS* and *EPIC-pn*) X-ray camera's of *XMM-Newton*, presented in chapters 3–4, provides a powerful tool to study in detail the dynamics, the distribution and the physical properties of the (reverse) shock heated plasma, while the bandwidth (up to 15 keV) offers an unique opportunity to assess the origin of the hard X-ray continuum. While I was not the “principle” investigator of this work, I have made a substantial contribution to the analysis.

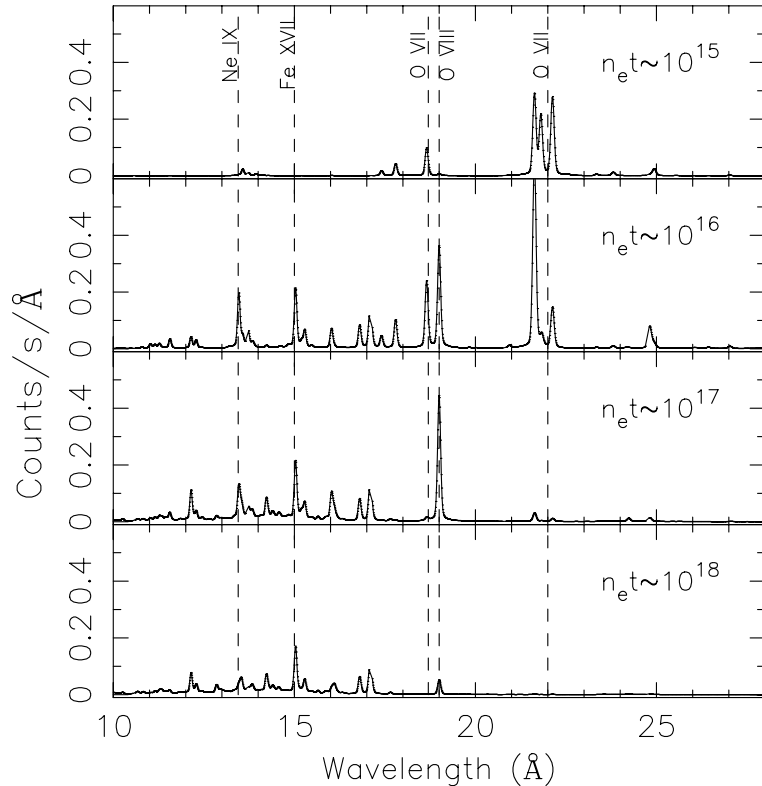


Figure 1.3: The effect of non-equilibrium ionisation on an optically thin plasma which has been instantaneously heated to $kT = 0.6$ keV. The spectra are labeled with the corresponding ionisation parameters ($n_e t$). The data are convolved with the *RGS* response.

I did the high resolution (i.e. *RGS*) analysis in chapter 3. In chapter 4 I did all the spectral analysis, which includes the temperature, ionisation age and abundance maps and also contributed in deriving the Doppler velocity maps.

In chapters 5–7 data on the remnants SNR B 0540-69.3, N 103B and DEM L 71 in the Large Magellanic Cloud (LMC) are presented. These remnants were chosen because of their small angular extent ($\leq 2'$) and relatively high intrinsic brightness. These qualities make them excellent candidates for high resolution *RGS* observations. Here we probe astrophysical quantities that affect line shape

and production, such as electron temperature, density, elemental abundance and resonance scattering. SNRs in the Small Magellanic Clouds (SMC) are fainter than their LMC counterparts and are thus not as well studied. In chapter 8 we utilise the large effective area and field-of-view of the *EPIC* cameras to do a synoptic spectral study of SNRs in the SMC.

References

- Cioffi, D.F., 1990, in *Physical Processes in hot Cosmic Plasmas*, p. 1, ed. W. Brinkmann et al., Dordrecht, Kluwer
- Conti, P.S., Garmany, C.D., de Lore, C., & Vanbeveren, D., 1983, *ApJ*, 274, 302
- Gronenschild, E.H.B.M., & Mewe, R., 1982, *A&ASS*, 48, 305
- Gull, S.F., 1975, *MNRAS*, 171, 237
- Hamilton, A.J.S., Sarazin, C.L.S., & Chevalier, R.A., 1983, *ApJS*, 51, 115
- Harkness, R.P., & Wheeler, J.C., 1990, in *Supernovae*, eds, p. 1, ed. A.G. Petschek, New York, Springer-Verlag
- Itoh, H., 1984, *Physica Scripta*, T7, 19
- McKee, C.F., 1974, *ApJ*, 188, 355
- Mewe, R., 1984, *A&AR*, 3, 127
- Nomoto, K., Hashimoto, M., Tsujimoto, T., et al., 1997, *Nucl. Phys. A*, 621, 467
- Sedov, L.I., 1959, *Similarity and Dimensionless Methods in Mechanics* (New York:Academic)
- Shapiro, P.R., & Moore, R.T., 1976, *ApJ*, 207, 460
- Uomoto, A., 1986, *ApJ*, 310, L35

Chapter 2

XMM-Newton & High Resolution Spectroscopy

2.1 *XMM-Newton*

The XMM-Newton X-ray observatory is the most powerful instrument for cosmic X-ray spectroscopy to date and particularly suited for spectral diagnostics of supernova remnants. The salient features for SNR research comprise: (i) an outstanding spectral grasp brought about by the large effective collecting area, bandwidth and spectral resolving power of the X-ray telescopes, (ii) an unprecedented high energy response which allows high quality X-ray imaging up to 15 keV, (iii) an unique capability for high resolution ($R > 100$) spectroscopy of moderately extended ($\Delta\theta \leq 2'$) sources. An additional asset is the ability to provide simultaneous observations with all instruments.

The core of the *XMM-Newton* observatory are three high-throughput, medium angular resolution (~ 15 arcsec half energy width) X-ray telescopes (see Fig. 2.1). They have a peak effective area of $\sim 1500 \text{ cm}^2$ at 1 keV, $\sim 500 \text{ cm}^2$ at 5 keV and sensitivity out to 15 keV. All three telescopes have CCD focal-plane cameras, collectively referred to as the European Photon Imaging Camera (*EPIC*). Two CCD cameras are metal oxide semiconductor (MOS) type devices (Turner et al. 2001) and the third is a pn-junction device (Strüder et al. 2001). Two of the telescopes are equipped with an array of reflection gratings, which, together with two dedicated CCD cameras at the spectroscopic focus, constitute the the Reflection Grating Spectrometer (RGS) experiment (den Herder et al. 2001).

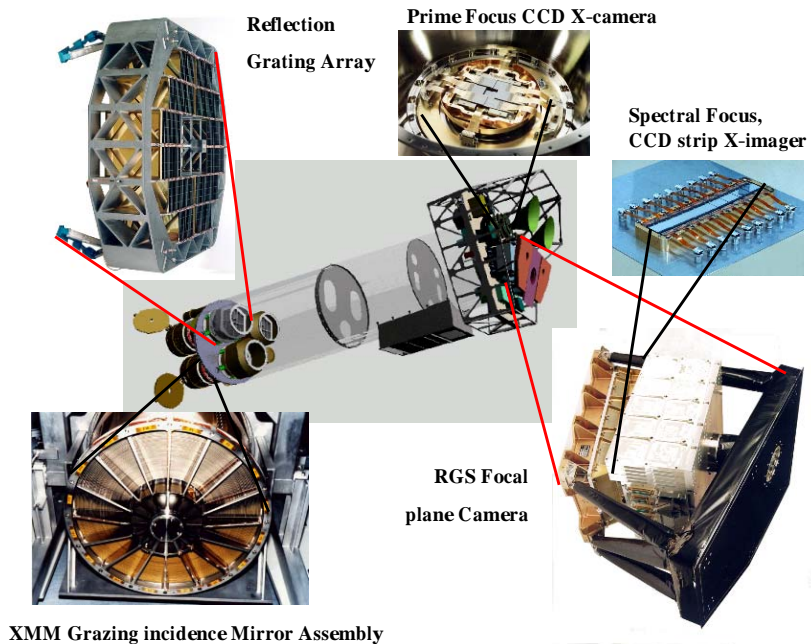


Figure 2.1: Sketch of the XMM-Newton payload. Blow ups of various components are also shown (Courtesy of J.A.M. Bleeker).

The Reflection Grating Arrays (RGA) are mounted permanently behind their mirror assemblies. The RGA intercepts approximately half the light for high-resolution spectroscopy ($5\text{--}38\text{ \AA}$ band), while the other half of the light goes to the *EPIC-MOS* detectors. A schematic of this is also shown in Fig. 2.2.

2.1.1 Reflection Grating Spectrometer

A detailed analysis of SNR spectra is impossible with the moderate CCD resolution. For instance, in CCD-resolution the eight charge states of Fe-L present in the observed wavelength band are totally blended and form a quasi-continuum. Resolving these Fe lines gives invaluable information on the temperature structure. This can be achieved only with a grating measurement. Moreover, the

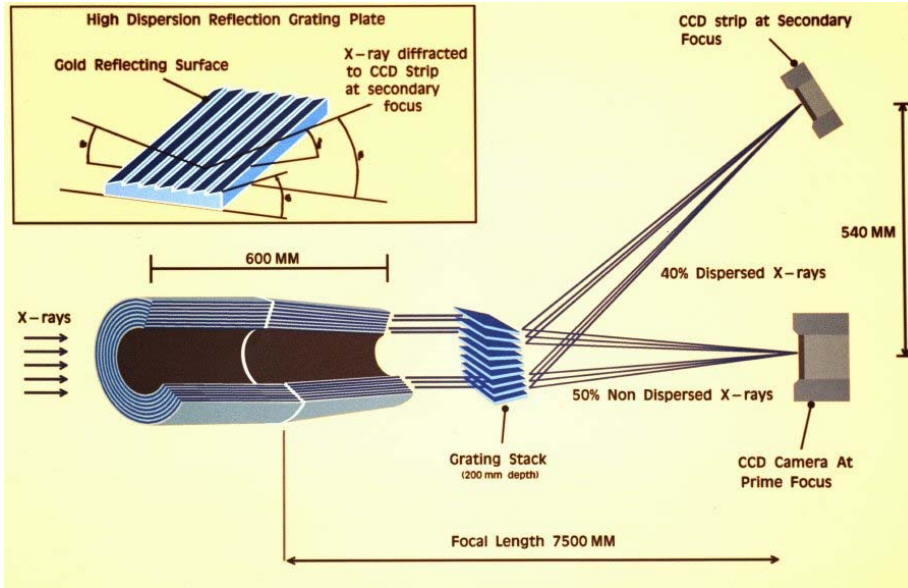


Figure 2.2: The light path in two X-ray telescopes on board XMM-Newton. Approximately half of the incoming light focused by the multi-shell grazing incidence mirrors is directed onto the camera at the prime focus, while the other half is dispersed by a grating array onto a linear strip of CCDs (Courtesy of J.A.M. Bleeker).

K-shell lines of H-like and He-like ions of N, O, Ne, and Mg are intense in the *RGS* wavelength band.

The dispersive spectrometers aboard the *XMM-Newton* (*RGS*) and *Chandra* (*HETG*, *METG* & *LETG*) observatories are nominally designed to study point sources. When used to study spatially extended sources, such as supernova remnants, the spectral resolution is generally degraded. This is because these instruments are slitless spectrometers, so any spatial extent is convolved with the spectral dispersion. However, useful information may still be extracted from extended source observations.

The *Chandra* gratings provide higher resolving power than the *RGS* for point source observations. When observing extended sources, however, the *RGS* has a significant advantage over contemporary dispersive spectrometers. This is il-

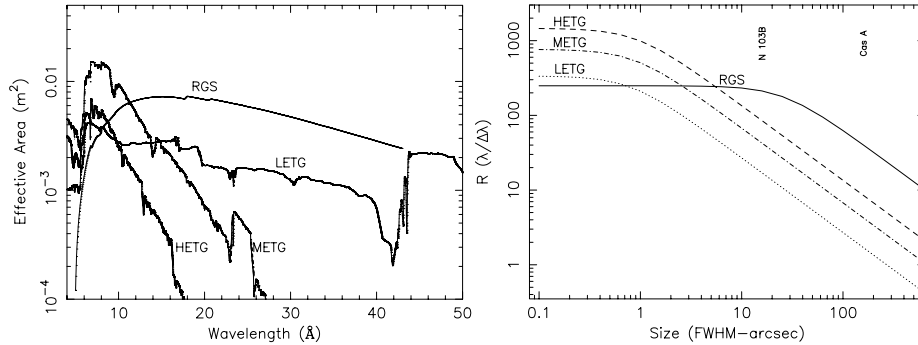


Figure 2.3: The effective area as a function of wavelength (left) and spectral resolution (at 15\AA) as a function of source extent (right) of the *XMM-Newton* *RGS* compared with to the three *Chandra* high-resolution spectrometers. The FWHM sizes of two well known supernova remnants (viz. N 103B and Cassiopeia A) are also indicated in the spectral resolution plot.

illustrated in Fig. 2.3. Here a comparison of the effective areas (left) and spectral resolving powers ($\lambda/\Delta\lambda$) at 15\AA (right) for the various grating spectrometers are given. Clearly, the *RGS* has a larger effective area in the spectral range of $10\text{--}35\text{\AA}$. Also note that at small sizes the *Chandra* spectrometers have higher spectral resolving power, but there is a crossover where the *RGS* starts to outperform them at $\sim 0.75''$, $\sim 2.5''$ and $\sim 5.5''$ for *LETG*, *METG* and *HETG* respectively.

SNRs are spatially extended sources with sizes typically ranging from a few tens of arcseconds to a few degrees. The *RGS* is thus the best suited instrument for high resolution studies of SNRs. Fig. 2.4 displays a simulated *METG* and *RGS* spectrum for a source extent of $30''$ FWHM. Fig. 2.4 shows that the *RGS* spectrum is of superior quality in terms of the spectral resolution and also in the number of photons collected.

2.2 Plasma diagnostics

High-resolution spectroscopy permits a diagnosis of a variety of plasma parameters such as temperature, ionisation parameter, emission measure, densities, abundances and velocities. As mentioned previously, the wavelength band $5\text{--}35\text{\AA}$ contains a number of prominent lines from abundant elements, including

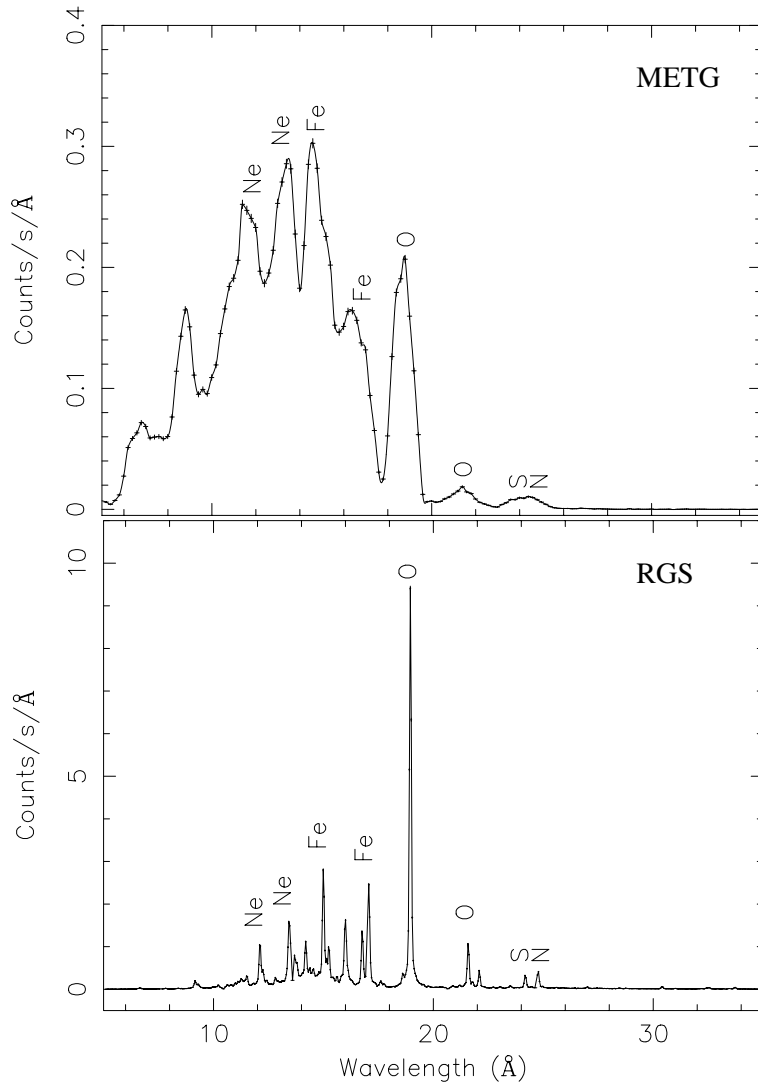


Figure 2.4: Simulated METG and *RGS* spectra for a source extent of $30''$ (FWHM).

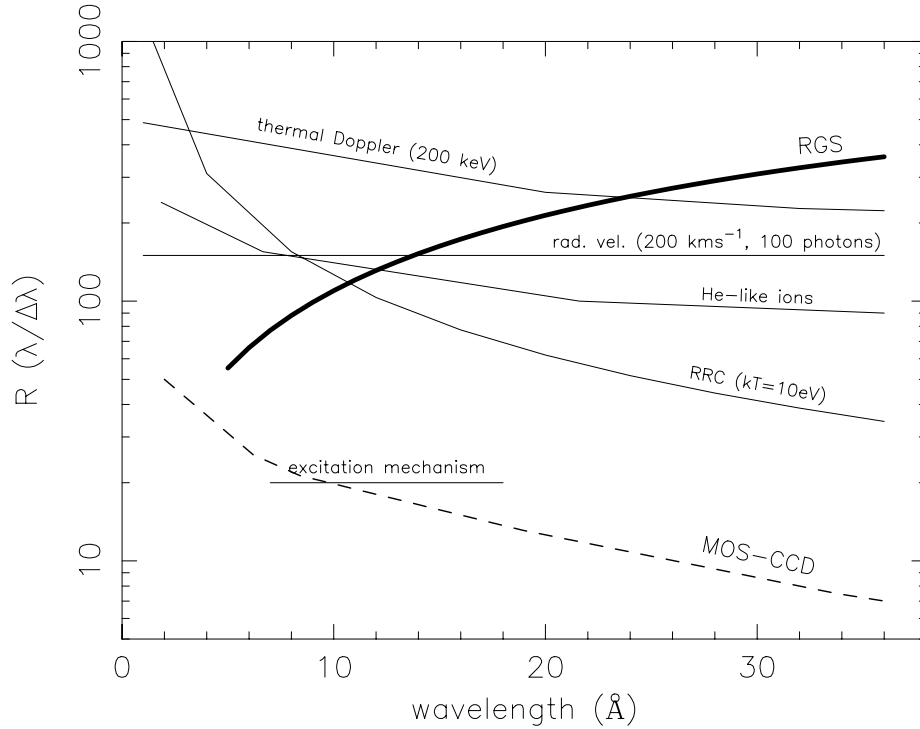


Figure 2.5: Resolving power required for some spectroscopic diagnostics, as a function of wavelength of the diagnostic feature. The *RGS* resolving power is for a source extent of $30''$. Adapted from Paerels (1997).

the K-shell transitions of carbon through to silicon and also L-shell transitions of iron. These lines are powerful diagnostics of plasma parameters because the line strengths are generally very sensitive to the electron temperature and the elemental abundances.

Fig. 2.5 displays some examples of spectroscopic diagnostics and the resolving power needed to exploit them. The resolving power of the *RGS*, at a source extent of $30''$ FWHM (comparable to SNR 1E0102-72), is also shown. The resolving power of the *EPIC-MOS* is shown for comparison. The wealth of spectroscopic features currently detectable with the *RGS* can be clearly seen in Fig. 2.5. Take the dominant line excitation mechanism, which is a very basic

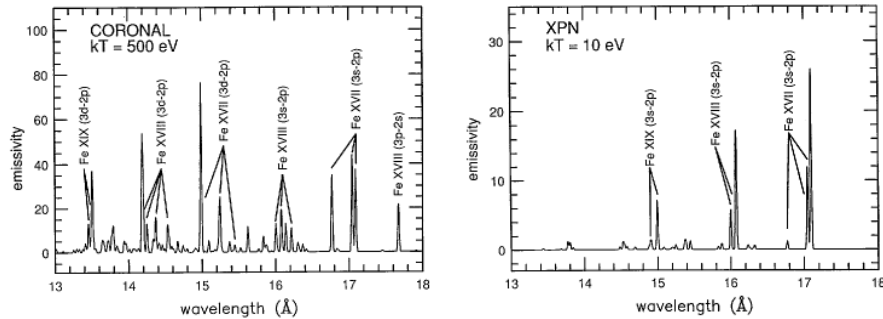


Figure 2.6: Line spectra emitted by Fe XVI–XIX under conditions of coronal (collisional) and photoionisation equilibrium. Adapted from Liedahl et al. (1990).

diagnostic, as an example. There are very clear differences between the emission spectra arising from collisionally and photoionised media. In the first case, line emission arises from radiative decays following collisional excitation, in the second case, radiative recombination dominates. The difference between these two cases can easily be distinguished in high resolution spectra. This is illustrated in Fig.2.6, which shows the spectra of Fe XVI–XIX under conditions of coronal (collisionally excited) and photoionisation equilibrium. In addition, for low enough electron temperatures the radiative recombination continua (RRC) appear as narrow, line-like features at the series limits. It has always been known that X-ray spectra from SNR are dominated by emission from collisionally ionised gas. However, it is only now that this can be unambiguously seen in high resolution spectra.

In the following subsections, some of the physical properties that can now be addressed with the spectral resolving power brought about by *RGS* are highlighted.

2.2.1 He-like ions

The electron temperature can be diagnosed from the intensity ratio of two lines with the same ionisation stage, but depending differently on electron temperature, e.g. two collisionally excited lines with different excitation energies such as the Lyman α and β lines. Alternatively, one can measure the ratio of lines at nearly the same wavelength for which the excitation functions have a different

dependence on T_e . The intensities in the $n = 2 \rightarrow 1$ transitions in the helium-like ions are suitable. This triplet consists of the resonance line (r) ($1s^2 \ ^1S_0 - 1s2p \ ^1P_1$), the intercombination line (i) ($1s^2 \ ^1S_0 - 1s2p \ ^3P_{1,2}$) and the forbidden line (f) ($1s^2 \ ^1S_0 - 1s2s \ ^3S_1$), respectively. The intensity ratio $(i + f)/r$ (G-ratio) varies with electron temperature (Gabriel & Jordan 1969). The He-like ions are also sensitive to the density of the plasma. Here the intensity ratio f/i (R-ratio) varies with electron density.

The use of the He-like ions for the diagnostic of NEI plasmas is more complicated than in the case of equilibrium plasmas. The G ratio, for example, becomes less sensitive as an electron temperature indicator at low $n_e t$. Used in combination, though, the G and R ratios are useful for estimates of $n_e t$ and T_e . In addition, the O VIII/O VII ratio is also a good indicator of $n_e t$. The spectral evolution of the He-like lines of O VII with temperature and $n_e t$ is shown in Fig. 2.7. O VII has been chosen since these lines are generally the brightest He-like transitions in the *RGS* spectra of SNRs. The r , i and f lines peak in the range $n_e t \sim 10^{15} - 10^{17} \text{ m}^{-3}\text{s}$ for $kT_e \gtrsim 0.5 \text{ keV}$ and $n_e t > 10^{15} \text{ m}^{-3}\text{s}$ for $kT_e \lesssim 0.5 \text{ keV}$. Note that these lines are only enhanced at low electron temperatures in equilibrium conditions, i.e. $n_e t \gtrsim 10^{18} \text{ m}^{-3}\text{s}$. In the case of extreme underionisation (i.e. $n_e t \lesssim 10^{15} \text{ m}^{-3}\text{s}$), the ratio plots yield a high $(i + f)/r$ ratio ($G > 2$) and low f/i ratio ($R < 2$).

The He-like ions are clearly valuable plasma diagnostic indicators, for electron temperature and NEI effects. In order to apply this diagnostic power, however, the r , i and f lines need to be resolved. The He-like lines have for the first time been used in a SNR plasma diagnostic analysis of the *RGS* spectra of SNR 1E0102-72 (Rasmussen et al. 2001) and SNR N 132D (Behar et al. 2001). In spite of the angular extent of these sources and the velocity broadening of the lines, the RGS is capable of resolving the He- α complexes of O VII and Ne IX sufficiently well to estimate contributions from the forbidden, intercombination and resonance transitions that provide robust diagnostics for the temperature and density of the emitting medium. Fig. 2.8 shows the He-like triplet of O VII & Ne IX of SNR 1E0102-72 and a model fit using the known line wavelengths, and the line velocity profile. The ratio f/i (density diagnostic) obtained for O VII equals 3.4 ± 0.6 and is consistent with the low density limit. The ratio $(i + f)/r$ (temperature diagnostic) is 0.55 ± 0.03 for O VII and 0.49 ± 0.05 for Ne IX. The electron temperatures corresponding to these ratios are $\sim 0.3 \text{ keV}$ and $\sim 0.65 \text{ keV}$ for O VII and Ne IX respectively, in agreement with electron temperature estimates derived from other methods (e.g. Ly- α /Ly- β ratios). The presence of bright emission lines from the H-like ions in the spectrum indicates

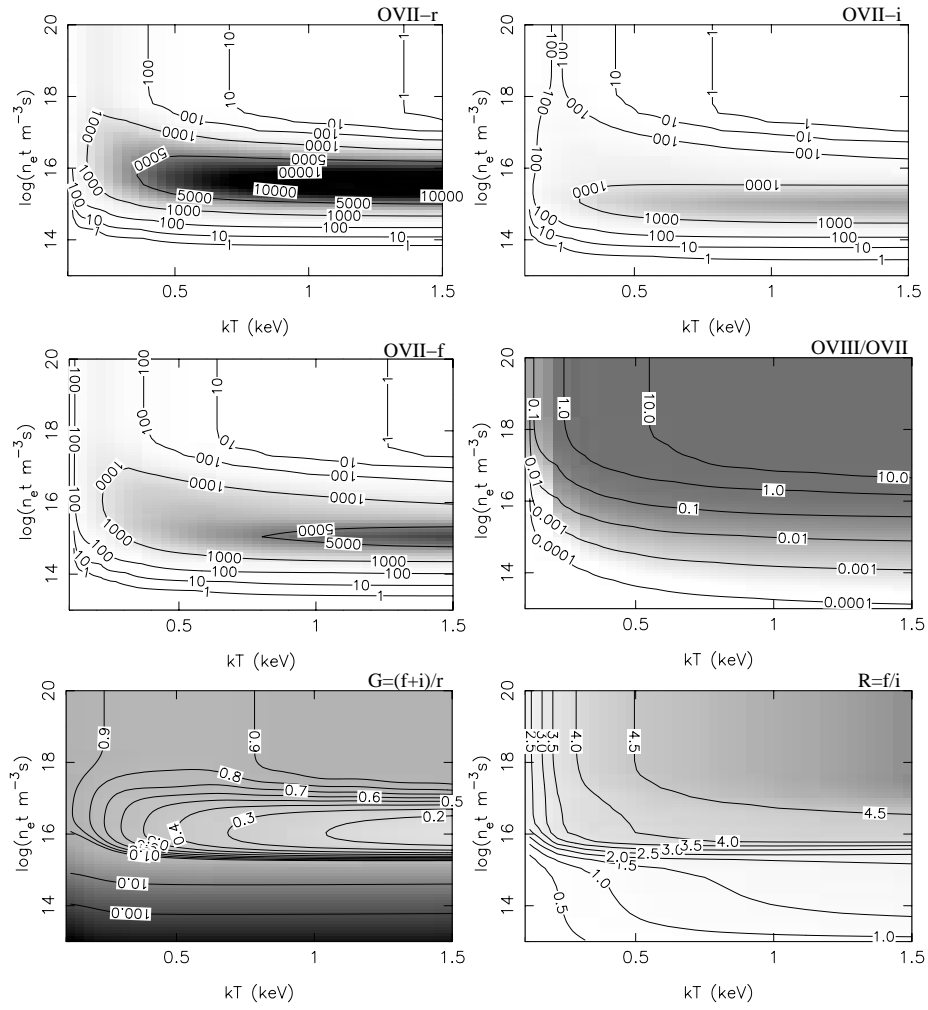


Figure 2.7: Relative intensities of the O VII *r*, *i* and *f* lines as a function of ionisation parameter and electron temperature. The O VIII/O VII, G ((*i* + *f*)/*r*) and R (*f*/*i*) ratios are also shown. The intensities are indicated by greyscale and overlaid contours.

that the He-like and H-like emission are from spatially distinct regions, since the neighbouring H-like charge states (O VIII and Ne X) are underpopulated at the electron temperatures and low $n_e t$ values inferred from the He-like emission lines. This is consistent with emission from (reverse) shock heated plasma, where the He-like emission is presumably from ejecta that has encountered the shock more recently.

2.2.2 Elemental Abundance

Abundance determination is an important part of SNR studies as remnants can be used to probe both the ISM elemental abundances and the abundances of elements produced during the supernova explosion. ISM elemental abundances can be determined by studying evolved remnants where the mass of swept up ISM material is much larger than the ejecta material. In young remnants most of the X-ray emission is from shock heated ejecta material. The abundances of the ejecta material not only give an indication of the supernova type, but can also assist in refining nucleosynthesis models. For example, the exact binary evolution of type Ia SN has not been identified. Nomoto et al. (1997) provided some constraints on the progenitor system from the viewpoint of nucleosynthesis. They presented nucleosynthesis results for various deflagration speeds to constrain the rate of accretion from the companion star. The explosive nucleosynthesis yields for fast deflagration (W7 & W70, where 7 & 70 indicate different deflagration speeds) and delayed detonation (WDD1,2&3, where 1,2&3 indicate the density at the deflagration-to-detonation transition) models of Nomoto et al. (1997) are given in table 2.1. Here the measurement of Si, S, Ar and Ca abundances is useful to distinguish the type Ia models. The nucleosynthesis yields presented by Woosley & Weaver (1995) for core-collapse SNe with 11, 12, 15 & 25 M_{\odot} (ZAMS mass) progenitors are also given in table 2.1.

In both equilibrium and non-equilibrium situations, ions of different elements which have similar ionisation potentials usually coexist in close proximity. Thus the ratios of the prominent emission lines from ions of different elements yield, in a relatively model-independent way, the elemental abundances. First the temperature and $n_e t$ distribution is obtained by analysing a suitable set of lines from one given element. Then the relative abundance can be determined by selecting lines from different elements. The absolute abundances can also be determined by comparing the line intensities to neighbouring, unblended, continuum bands. It is thus important to have good quality spectra in which individual emission lines and continuum can be clearly identified. This point is illustrated in the case of SNR N 103B (see chapter 6). N 103B has been designated as being the

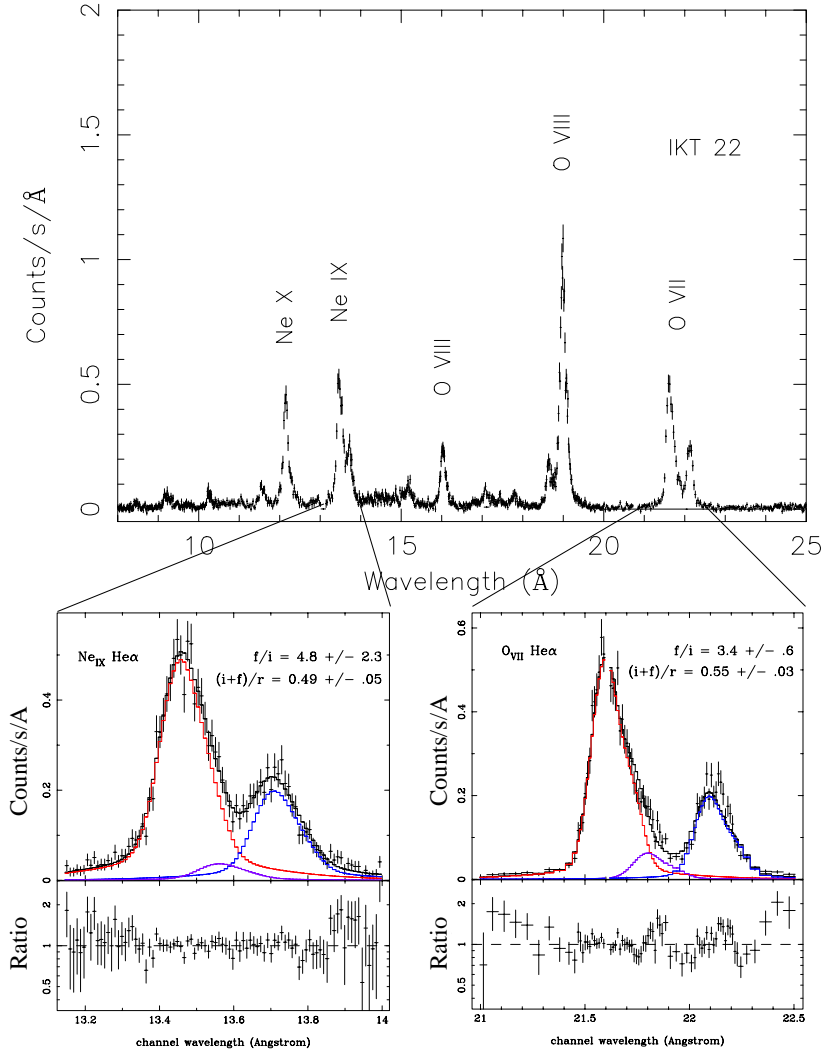


Figure 2.8: The *RGS* spectrum of SNR 1E0102-72. A blow up of the O VII and Ne IX He- α triplets, illustrating the line profiles used for fitting the He- α triplets in the derivation of the f/i and $(i+f)/r$ line ratio. Adapted from Rasmussen et al. (2001).

Table 2.1: Theoretical explosive nucleosynthesis abundance yields for type Ia (above) and type II (below) models. The abundance ratios are all relative to solar (Anders & Grevesse 1989) and normalised to Si. The abundances for the Type Ia models are from Nomoto et al. (1997), while the Type II yields for the 11, 12, 15 & 25 M_{\odot} zero-age-main-sequence progenitors are taken from Woosley & Weaver (1995).

Element	W70	W7	WDD1	WDD2	WDD3
C/Si	0.08	0.07	0.01	0.01	0.01
O/Si	0.07	0.07	0.02	0.02	0.02
Ne/Si	0.01	0.01	0.01	0.01	0.01
Mg/Si	0.12	0.06	0.03	0.02	0.02
S/Si	1.28	1.07	1.15	1.17	1.16
Ca/Si	1.09	0.75	0.90	0.94	0.93
Ar/Si	1.53	0.89	1.27	1.38	1.37
Fe/Si	1.86	1.56	0.50	0.85	1.43
Ni/Si	0.99	0.67	0.11	0.15	0.22
Element	11 M_{\odot}	12 M_{\odot}	15 M_{\odot}	20 M_{\odot}	25 M_{\odot}
C/Si	0.52	0.19	0.27	0.28	0.29
O/Si	0.44	0.16	0.45	1.14	1.89
Ne/Si	0.59	0.12	0.22	1.08	2.18
Mg/Si	0.57	0.12	0.70	2.07	2.04
S/Si	0.87	1.53	0.62	0.50	0.66
Ca/Si	0.65	2.04	0.43	0.36	0.47
Ar/Si	0.63	1.62	0.50	0.42	0.58
Fe/Si	1.37	0.23	0.70	0.30	0.16
Ni/Si	6.89	0.68	0.01	0.01	0.01

result of type Ia SN based on the absence of O, Ne Mg emission in the medium CCD-resolution *ASCA* spectrum (Hughes et al. 1995), shown in Fig. 2.9. The *RGS* spectrum also shown in Fig. 2.9, however, clearly reveals these lines because of its higher spectral resolution. Also, the *RGS* spectra of N 132D and SNR 1E0102-72 represent the first data in which C and N emission have been detected in X-ray spectra of SNRs.

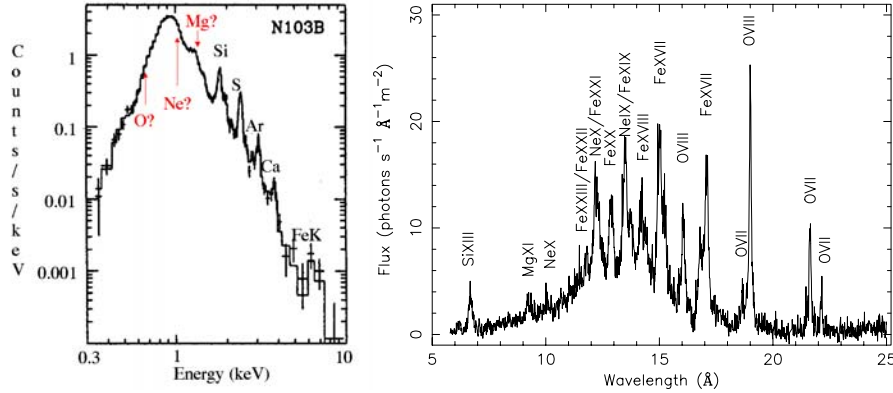


Figure 2.9: The *ASCA* (left) (Hughes et al. 1995) and *RGS* (right) spectrum of N103B (chapter 6). The O, Ne and Mg features are unresolved in the *ASCA* spectrum while the *RGS* spectrum clearly reveal emission from the elements. Note that the *ASCA* is given in energy scale, while the *RGS* spectrum is in wavelength ($E(\text{keV}) \sim 12.4/\lambda(\text{\AA})$).

2.2.3 Thermal Doppler Broadening

Shock waves in the shell of SNRs are thought to be collisionless because at the low densities encountered in remnants the shock front is thinner than the mean free path for collisions. The actual heating mechanism in collisionless shocks is not straightforward and needless to say, not well understood. The heating of particles at the shock-front is thought to be produced by collective processes, such as plasma waves (for a review see for instance, Draine & McKee 1993; Laming 2000). Since the heating is not collisional the plasma can be regarded as a two fluid system consisting of electrons and ions. There is no guarantee that there will be equilibration between the electron and ion temperature. A clear hint for non-equilibration is the low electron temperature in young SNRs, which in no object seems to exceed 5 keV, whereas a typical shock velocity of 4000 km s^{-1} should give rise to a mean plasma temperature of ~ 20 keV (e.g., McKee & Hollenbach 1980; Hughes et al. 2000). X-ray observations usually allow only the electron temperature to be determined. The ion temperature is difficult to measure, as it does not alter the continuum shape and hardly influences the ionization and excitation balance.

A straightforward ion temperature diagnostic, however, is the thermal Doppler

broadening of emission lines. The radial velocity distribution in a thermal plasma is Gaussian with a variance $\sigma^2 = kT_i/m_i$, with T_i and m_i the ion temperature and mass respectively. For the resolving power corresponding to this width, we find $R = (m_i c^2 / kT_i)^{1/2} \simeq 1077 A^{1/2} / T_{\text{keV}}^{1/2}$ (Paerels 1997), with A the atomic weight of the ions and T_{keV} the ion temperature in keV. Doppler measurement of ion temperatures < 200 keV, for all ions of interest ($A > 12$), are still unattainable with current instrumentation, as illustrated in Fig. 2.5. It is still possible to measure ion temperatures > 200 keV as recently shown by Vink et al. (2003). They measured a Doppler line broadening in a compact knot at the edge of SN 1006 with the *RGS*. The observed O VII-triplet line width of $\sigma \sim 0.123$ mÅ at a line energy of 21.6 Å indicates an oxygen-ion temperature of $kT_i \sim 530$ keV. Combined with the observed electron temperature of 1.5 keV, the observed broadening is direct evidence for temperature non-equilibration.

2.2.4 Optical Depth Effect

Optical depth effects may alter the X-ray spectrum, despite the low density ($< 10^7 \text{ m}^{-3}$) associated with SNRs. The large sizes of the X-ray emitting region (typically a few pc) yield column densities of 10^{24} m^{-2} . While the continuum is optically thin at these column densities, several strong lines could suffer from effects of resonance scattering. Resonance scattering is a well known effect in X-ray spectra of active solar regions where the column density is of similar order. Scattering in a resonance line does not destroy photons, but merely redistributes them in a different direction. The effects of resonance scattering are highly dependent on the spatial morphology of the source. In SNRs the X-ray emission is usually from limb brightened shells. If the limbs are studied, then the column density along the line-of-sight is much higher than perpendicular to the line-of-sight. The emitted line photons are thus preferentially scattered out of the line-of-sight resulting in lower line intensities. This could lead to underestimation of particle densities and abundances based on the line intensities.

The optical depth at the line centres are given by Kaastra & Mewe (1995) as

$$\tau = \frac{4.24 \times 10^6 f N_{24} \left(\frac{n_i}{n_z}\right) \left(\frac{n_z}{n_H}\right) \left(\frac{M}{T_{\text{keV}}}\right)^{1/2}}{E_{\text{eV}} \left(1 + \frac{0.0522 M v_{100}^2}{T_{\text{keV}}}\right)^{1/2}} \quad (2.1)$$

where f is the absorption oscillator strength of the line, E the energy in eV, N_{24} the hydrogen column density in units of 10^{24} m^{-2} , n_i the density of the ion, n_z the density of the element, M the atomic weight of the ion, T_{keV} the ion temperature in keV and v_{100} the micro-turbulence in units of 100 km s^{-1} .

In practice, the observer does not know a priori what the plasma conditions are. However ratios of line intensities within the same ion, e.g. Ly- α /Ly- β , can be used to directly measure the optical depth. Signatures of resonance scattering have been detected in the *RGS* data of Cas A (chapter 3) and DEM L 71 (chapter 7).

2.3 Accuracy of atomic physics

The ionisation balance is probably the major uncertainty entering the comparison of models. Fortunately, the ionisation and recombination rates of the H-like and He-like ions, which are the strongest lines in SNR spectra, are known more accurately than most of the other rates. The accuracy of atomic data used for high resolution spectral diagnostics are of obvious importance. For this reason a number of projects are currently underway to update existing atomic databases e.g. APED (Smith et al. 2001) and SPEX (Kaastra et al. 2003). The accuracy of the data is not the only important objective, but also the completeness of the spectral content. For example published collisional excitation rate data generally exist only for levels with low principle quantum numbers ($n \lesssim 6$). While individual lines of higher n are weak, lines become increasingly close together as one approaches the ionisation limit. The net contribution of these lines to the flux at the current spectral resolution can be significant. Fig. 2.10 shows the importance of the contribution of these lines. Here the O VIII Lyman series using the collision rates from the current MEKAL database (Mewe et al. 1995) is compared to a new version currently under development (Kaastra et al. 2003). An *RGS* spectrum of Cas A illustrating the astrophysical manifestations of these lines is also displayed in Fig. 2.10. Here the O VIII-Ly α line emission is reduced due to the high Galactic absorption towards Cas A. The higher order O VIII lines now become more important in an abundance determination, for example, since they carry more statistical weight than the O VIII-Ly α .

References

- Anders, E., & Grevesse, N., 1989, *Geochimica et Cosmochimica Acta*, 53, 197
Behar, E., Rasmussen, A.P., Griffiths, G., et al., 2001, *A&A*, 365, L242
Draine, B.T., & McKee, C.F., 1993, *ARA&A*, 31, 373
Gabriel, A.H., & Jordan, C., 1969, *MNRAS*, 145, 241

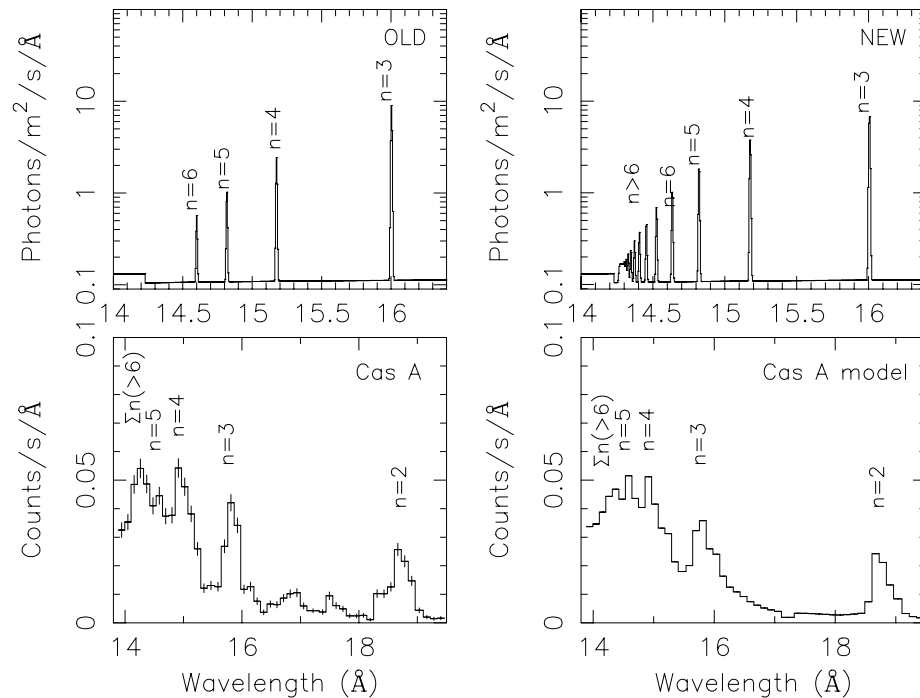


Figure 2.10: The O VIII Lyman series using the collision rates from the MEKAL database (Mewe et al. 1995) (top left) compared to new calculations (Kaastra et al. 2003) (top right). Calculations from the updated database show the contribution of emission from levels of higher principle quantum number ($n \geq 6$). An *RGS* spectrum of Cassiopeia A illustrating the astrophysical manifestations of these lines is displayed in the bottom left panel. The bottom right panel shows the new O VIII Lyman series calculations that has been convolved with a model that contains the Cassiopeia A spatial profile and an absorption component of $N_{\text{H}} \approx 1.3 \times 10^{26} \text{ m}^{-2}$.

den Herder, J.W., Brinkman, A.C., & Kahn, S.M., et al., 2001, *A&A*, 365, L7

Hughes, J.P., Hayashi, I., & Helfand, D.J., et al., 1995, *ApJ*, 444, L81

Hughes, J.P., Rakowski, C.E., & Decourchelle, A., 2000, *ApJ*, 543, L61

Kaastra, J.S., & Mewe, R., 1995, *A&A*, 302, L13

- Kaastra, J.S., Raassen, T., & Mewe, R., 2003, private communication
- Laming, J. M., 2000, *ApJS*, 127, 409
- Liedahl, D.A., Kahn, S.M., Osterheld, A.L., & Goldstein, W.H., 1990, *ApJ*, 350, L37
- Nomoto, K., Hashimoto, M., & Tsujimoto, T., et al., 1997, *Nucl. Phys.A*, 621, 467
- McKee, C.F., & Hollenbach, D.J., 1980, *ARA&A*, 18, 219
- Mewe, R., Kaastra, J.S., & Liedahl, D.A., 1995, *Legacy* 6, 16
- Paerels, F., 1997, in *X-ray Spectroscopy in Astrophysics*, p. 347, eds. J. van Paradijs & J.A.M Bleeker, Heidelberg, Springer-Verlag
- Rasmussen, A., Behar, E., Kahn, S. M., den Herder J. W., & van der Heyden, K., 2001, *A&A*, 365, L231
- Smith, R.K., Brickhouse, N.S., Liedahl, D.A., & Raymond, J.C., 2001, *ApJ*, 556, L91
- Strüder, L., Briel, U.G., Dennerl, K., et al., 2001, 365, L18
- Turner, M.J.L., Abbey, A., Arnaud, M., et al., 2001, 365, L27
- Vink, J., Laming, J.M, Gu, M.F., Rasmussen, A., Kaastra, J.S., 2003, *ApJ*, 587, L31
- Woosley, S.E. & Weaver, T.A. 1995, *ApJSS*, 101, 181

Chapter 3

Cassiopeia A: on the origin of the hard X-ray continuum and the implication of the observed O VIII Ly- α /Ly- β distribution

J.A.M. Bleeker, R. Willingale, K. van der Heyden, J.S. Kaastra
B. Aschenbach, J. Vink

Published in *Astronomy & Astrophysics* 365, L225 (2001)

Abstract

We present the first results on the hard X-ray continuum image (up to 15 keV) of the supernova remnant Cas A measured with the EPIC cameras onboard *XMM-Newton*. The data indicate that the hard X-ray tail, observed previously, that extends to energies above 100 keV does not originate in localised regions, like the bright X-ray knots and filaments or the primary blast wave, but is spread over the whole remnant with a rather flat hardness ratio of the 8–10 and 10–15 keV energy bands. This result does not support an interpretation of the hard X-radiation as synchrotron emission

produced in the primary shock, in which case a limb brightened shell of hard X-ray emission close to the primary shock front is expected. In fact a weak rim of emission near the primary shock front is discernable in the hardest X-ray image but it contains only a few percent of the hard X-ray emissivity. The equivalent width of the Fe-K line blend varies by more than an order of magnitude over the remnant, it is hard to explain this as Fe-emission from the reverse shock heated ejecta given the ejecta temperature and the age of the remnant. The uniquely high wavelength-dispersive *RGS*-spectrometer has allowed, for the first time, to extract monochromatic images in several highly ionised element species with high spectral resolution. We present here a preliminary result on the measurement of the O VIII Ly- α and Ly- β brightness distribution and brightness ratios. The large observed decrease of the Ly- α /Ly- β ratio going from the N to the SE can be explained by small-scale ($10''$) variations in the N_{H} column over the remnant and the potential presence of resonance scattering of the O VIII Ly- α photons in the limb brightened shell.

3.1 Introduction

The young galactic supernova remnant (SNR) Cassiopeia A (Cas A) is widely believed to be the result of the core collapse of a massive star, probably an early type Wolf-Rayet star (Fesen et al. 1987). Cas A is classified as an oxygen rich remnant since optical spectroscopic observations (Chevalier & Kirshner 1979) show the supernova ejecta (in the form of fast moving knots) to contain mostly oxygen and oxygen burning products such as sulphur, argon and calcium. At all wavelengths Cas A has the appearance of a broken shell with a radius varying between $1.6'$ to $2.5'$.

One of the outstanding problems in the study of Cas A is the origin of a recently discovered hard X-ray continuum in the spectrum of this remnant. From a theoretical point of view both synchrotron emission from shock accelerated electrons and non-thermal Bremsstrahlung from electrons accelerated from the tail of the thermal emission could be possible explanations for the hard continuum. In addition, high resolution spatially resolved spectroscopy of the remnant in the X-ray domain is a powerful tool to study in detail the distribution and physical properties of the (reverse) shock heated plasma. The bandwidth (up to 15 keV) of *XMM-Newton* and the presence of high wavelength-dispersive spectrometers (*RGS*) offers an unique opportunity to address these questions. In this respect *XMM-Newton* strongly complements Chandra, and this paper gives a first highlight of this capability.

3.2 Observations

A description of the instrument is given by Jansen et al. (2001). The data were obtained in July 2000 with a net exposure time of 30 ks. The telescope was pointed at

the centre of the remnant ($\alpha = 23^{\text{h}}23^{\text{m}}25^{\text{s}}$ $\delta=58^{\circ}48'20''$) and the telescope roll angle was such that the *RGS* dispersion axis was aligned at 45° (NE) on the sky.

The raw data were processed with the development version of the *XMM-Newton* Science Analysis System(SAS). The *RGS* spectra were extracted by applying spatial filters to the spectral image and the spectral order ($m = -1$) is selected applying the appropriate pulseheight intervals to the CCD spectral camera.

3.3 The hard X-ray data

A high-energy tail has been observed in the X-ray spectrum of the supernova remnant Cassiopeia A by the Compton Gamma Ray Observatory (The et al. 1996), BeppoSAX (Favata et al. 1997) and the Rossi X-ray Timing Explorer (Allen et al. 1997). Previous hard X-ray imaging observations, for example using BeppoSAX (Vink et al. 1999) indicated that the hard continuum radiation originated predominantly in the W region of the remnant, however this result was based on deconvolved images from a typically $1'$ resolution telescope with moderate effective area. The combination of large collecting area in the energy band 4.0 to 12.0 keV and angular resolution of a few arcseconds of *XMM-Newton* provides us with a unique opportunity to search for the distribution and origin of this hard “tail”.

3.3.1 The X-ray spectrum above 4.0 keV

Below 4.0 keV the observed spectrum is a complicated combination of spectral lines, continuum emission and the effects of interstellar absorption but above 4.0 keV it is dominated by a smooth continuum and the Fe-K emission line complex. A joint spectral fit of the *EPIC-MOS* and *EPIC-pn* spectra was performed in the energy band 4.0–12.0 keV for the complete remnant. The model included a single Bremsstrahlung component plus a power law continuum with photon index fixed at the previously observed value (Allen et al. 1997) of 1.8 below a break energy of 16 keV. Gaussian line features were used to fit the obvious Fe and Ni line blends. The resulting fit is shown in Fig. 3.1. The best fit Bremsstrahlung temperature is 2.56 ± 0.05 keV with emission measure $1.99 \pm 0.04 \times 10^{59} \text{ cm}^{-3}$ for a distance of 3.4 kpc and the power law flux at 1 keV is $0.0416 \pm 0.003 \text{ photons cm}^{-2} \text{ s}^{-1} \text{ keV}^{-1}$. The Fe line energy is 6.603 ± 0.001 keV in the *EPIC-MOS* and 6.623 ± 0.002 keV in the *EPIC-pn*. The errors quoted are statistical only and indicate the high quality of the data, the difference between the *EPIC-MOS* and *EPIC-pn* values may be attributed to systematic uncertainties which are at present of the order of 10 eV. We estimated the effect of potential pile-up in the *EPIC-pn* camera to be not larger than $\sim 3\%$ for the brightest regions. Fig. 3.1 indeed shows that the *EPIC-MOS* spectra, which do not suffer from pile-up, and the *EPIC-pn* spectrum are fully compliant. The equivalent width of the Fe line is 1.02 keV for the *EPIC-MOS* and 1.11 keV for the *EPIC-pn*. The Ni line energy is 7.740 ± 0.015 keV

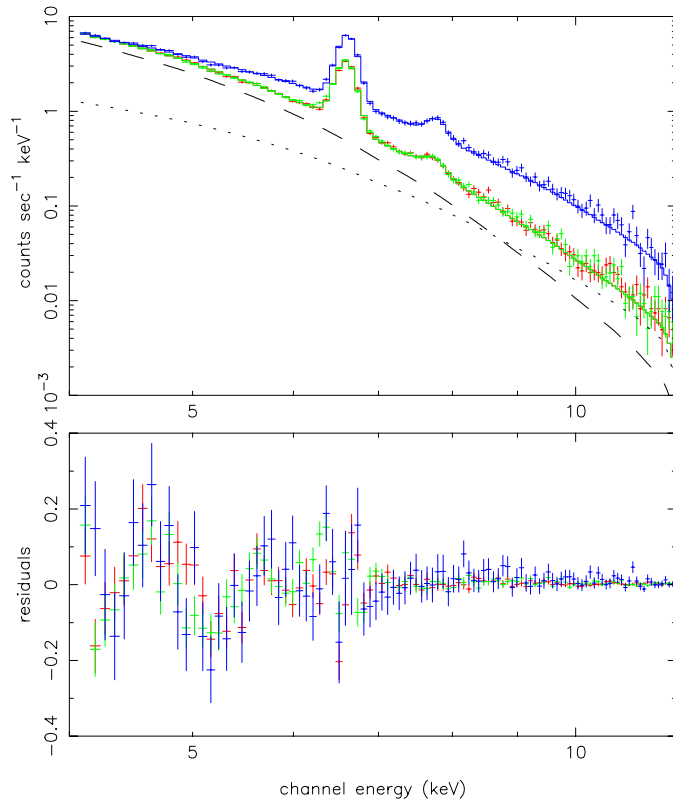


Figure 3.1: Joint spectral fit of the hard tail from the complete remnant, *EPIC-MOS* 1 red, *EPIC-MOS* 2 green and *EPIC-pn* blue. The dashed and dotted line indicate the Bremsstrahlung and power law components contributing to the *EPIC-MOS* continuum.

in the *EPIC-MOS* and 7.783 ± 0.015 keV in the *EPIC-pn* corresponding to Ni xxvi 7.687 keV and/or Ni xxvii 7.799 keV. The equivalent width of the Ni line was 0.130 keV for the *EPIC-MOS* and 0.179 keV for the *EPIC-pn*. Allen et al. (1997) fitted the composite spectrum of Cas A over a much broader energy range extending out to 100 keV using two Raymond-Smith collisional ionisation equilibrium (CIE) thermal components with $kT_1=0.6$ and $kT_2=2.9$ keV to fit the soft band below 6 keV and a broken power law ($E_b=15.9$ keV) with photon index 1.8 below E_b and 3.0 above E_b with a flux of 0.038 photons $\text{cm}^{-2} \text{s}^{-1} \text{keV}^{-1}$ at 1 keV. Favata et al. (1997), from the

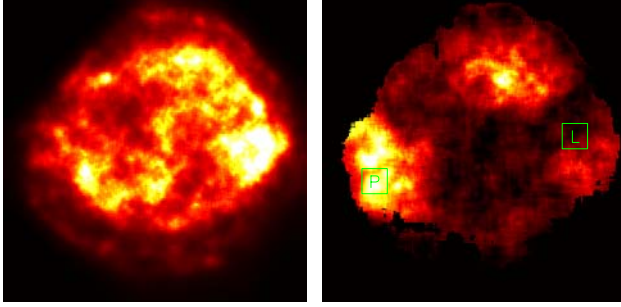


Figure 3.2: Continuum 4.06–6.07 keV (left) and Fe K equivalent width (right) black 0 keV to white 4 keV and above.

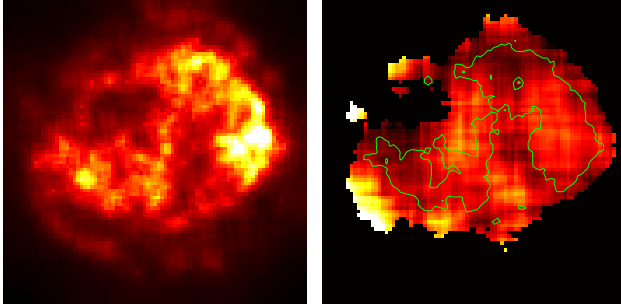


Figure 3.3: Continuum 8.10–15.0 keV (left) and hardness ratio $(10.0\text{--}15.0 \text{ EPIC-MOS} + \text{EPIC-pn}) / (8.10\text{--}10.0 \text{ EPIC-MOS} + \text{EPIC-pn})$ 0.15 black to 0.45 white.

BeppoSAX observations, obtained a continuum parameterized by two non-equilibrium ionisation (NEI) components with $kT_1=1.25$ keV, $kT_2=3.8$ keV and a power law with photon index 2.95 with a normalisation of $0.74 \text{ photons cm}^{-2} \text{ s}^{-1} \text{ keV}^{-1}$ at 1 keV. It is most important to note that, irrespective of the exact parameterization of these fits, they all share the fact that the X-ray flux above 8 keV becomes dominated by the power law component. More quantitatively, our spectral fit predicts a ratio between the power law and the Bremsstrahlung component in the *EPIC-MOS* cameras of 0.29 in the interval 4–6 keV, 1.04 in the 8–10 keV band and 2.00 in the 10–12 keV hardest band. We shall come back to this point in the next section on the X-ray images.

3.3.2 X-ray images above 4.0 keV

The *EPIC-MOS* and *EPIC-pn* images are practically identical. Fig. 3.2 shows *EPIC-MOS* images and Fig. 3.3 shows combined *EPIC-MOS* and *EPIC-pn* images. The lefthand panel of Fig. 3.2 is the continuum map for 4.07–6.07 keV an energy band in which no bright spectral lines are visible in either the *EPIC-MOS* or *EPIC-pn* spectra. The peak of the hard continuum occurs in the large knot to the W but there is also extended emission throughout the volume of the remnant. The outer rim (presumably just behind the blast wave) is visible but is very faint compared with the central volume.

The righthand image of Fig. 3.2 is the Fe K line equivalent width derived from the narrow energy band 6.20–6.92 keV. The continuum used to estimate the equivalent width was estimated by interpolation from the bands 4.06–6.07 keV and 8.10–15.0 keV. The Fe line is very bright relative to the continuum on the outer extremities of the SE knots, i.e. region marked P, but is rather weaker in the W where the continuum is bright, i.e. region marked L. The lefthand panel of Fig. 3.3 is the hard continuum above the Fe K line, 8.10–12.0 keV, which is very similar to the softer continuum image in Fig. 3.2. In order to try and locate where the hard X-ray tail originates we calculated the hardness ratio $(10.0-15.0)/(8.10-10.0)$ using both the *EPIC-MOS* and *EPIC-pn* cameras to give the best possible statistics. The result is shown in the righthand panel of Fig. 3.3. The contour superimposed in green is taken from the hard continuum map 8.10–15.0 keV and contains 37 % of the total counts in this energy band, the hardest region in the W contains less than 3 % of the total. The remaining 63 % of the hard flux is spread out over the rest of the remnant. There are significant changes in hardness over the remnant but all the bright features within the green contour have a remarkably similar spectrum above 8.0 keV.

From the spectral fits described in the previous section, it is clear that the photon flux observed in the continuum image in Fig. 3.3 is dominated by the hard tail (power law) component. *XMM-Newton* clearly detects the hard X-ray tail from the remnant but the hard X-ray image and the hardness ratio indicate that this flux does not predominate in a few localised regions, but pervades the whole remnant in a distribution similar to the softer thermal components.

3.3.3 The Fe K emission

Simpler spectral fits using a single Bremsstrahlung and one gaussian line were used to quantify the variation of the continuum and Fe K emission over the remnant. Region L in Fig. 3.2 corresponds to the brightest hard continuum and a rather low Fe equivalent width and region P to rather weak continuum with the highest Fe K equivalent width. The same model was also used to fit the composite spectrum. The results are summarised in Table 3.1. The apparent temperature in these fits is a measure of hardness and is higher than the value reported above because the power law continuum has been omitted for simplicity. It is clear that the temperature for the composite fit is similar

Table 3.1: Results of joint spectral fits using a single Bremsstrahlung and gaussian line 4.0–12.0 keV. Listed are the temperature kT , line centroid E_ℓ , equivalent width EW and line sigma width σ . The first values for E_ℓ , EW and σ are for the *EPIC-MOS* cameras and the second from the *EPIC-pn*.

Parameter	all	L	P
kT (keV)	3.53 ± 0.02	3.41 ± 0.14	3.15 ± 0.34
E_ℓ (keV)	6.60	6.60	6.67
	6.62	6.61	6.68
EW (keV)	0.95 ± 0.02	0.57 ± 0.08	6.19 ± 0.56
	1.01 ± 0.02	0.43 ± 0.18	5.28 ± 0.53
σ (keV)	0.083	0.079	0.047
	0.078	0.042	0.031

to that of the small regions (within the statistical accuracy), again indicating that the hard flux is distributed throughout the remnant. As shown in Fig. 3.2 and quantified in Table 3.1 the variation in equivalent width of the iron line is very large. We attempted to fit the composite spectrum from *EPIC-MOS* 1 + 2 + *EPIC-pn* 4.07–12.0 keV with a simple NEI model (see for example Borkowski 1994) plus a power law. The power law was again fixed at index 1.8 and the temperature kT fixed at 2.6 keV. This gave a good fit to the continuum with the Fe line blanked out.

A reasonable fit was obtained for an ionisation timescale parameter of 5.0×10^{11} s cm^{-3} or greater. For an age of 340 years, (10^{10} seconds) this implies a density of $> 50 \text{ cm}^{-3}$ which is rather large. This fit gave about the correct equivalent width for the Fe line (assuming solar abundances), but did not fit the line profile very well, presumably because the line is Doppler shifted and/or broadened. It also gave a reasonable fit to the Ni line feature at around 7.7 keV. Lower more reasonable values of the time scale 5.0×10^{10} s cm^{-3} corresponding to a density of 5 cm^{-3} predict a much larger equivalent width (a factor of 4 too large), a line energy which is too low and no Ni line at 7.7 keV.

Using the same model on region P in the SE where the equivalent width of Fe is very high gave a poor fit. No combination of temperature or time scale could produce a strong enough line at the correct energy. The P knot is clearly anomalous with abnormally high Fe abundance and/or extreme non-thermal equilibrium ionisation.

3.3.4 Discussion

The spectral form of the non-thermal high-energy “tail” is not inconsistent with a simple model of synchrotron emission from SNRs Reynolds 1998. However in such a model the electrons need to be accelerated to energies of tens of TeV at the primary

shock and the associated synchrotron emission would be expected to be concentrated in the compressed magnetic field just inside the shock front. The hard X-ray continuum maps from *XMM-Newton* indicates that the 8.0–15.0 keV flux, predominantly due to the previously reported high-energy tail, does not originate from a few localized regions such as X-ray bright knots and filaments, nor does it originate from a limb brightened (fractionary) shell close to the shock front generated by the primary blast wave. In fact a low brightness outer ring structure, presumably associated with the primary shock, can be discerned in the hard X-ray image but it contains only a few percent of the total hard X-ray flux. Therefore the hard X-ray image is morphologically inconsistent with the simple synchrotron model developed by Reynolds (1998). An alternative explanation for the observation of hard X-ray tails in the spectra of supernova remnants is the presence of non-thermal Bremsstrahlung generated by a population of suprathermal electrons (Asvarov et al. 1989; Laming 2000). One might expect in this case some degree of correlation with the strong line emitting regions, however abundance variations make this potential correlation ambiguous. A search of Cas A for regions with spectra devoid of line emission, as a possible tracer of synchrotron emission, was unsuccessful although Chandra observations indicated the presence of such a region just beyond the westernmost tip of the N rim of the remnant (Hughes et al. 2000). We specifically checked this region and still confirm the presence of, relatively weak, line emission, with for example equivalent widths of 200–300 eV for the He-like triplet of Si, S and Fe. We cannot exclude some contamination by line emission from neighbouring regions due to the wings of the XMM psf, on the other hand the Chandra data for this region also show line residuals above the continuum fit presented by Hughes et al. In summary we have not spotted any positive evidence, either morphologically or spectrally, for the presence of synchrotron emission in Cas A and, by implication, the associated TeV electrons. Consequently, whether the hard X-ray tail is thermal or non-thermal remains an open question.

3.4 High-resolution spectroscopic data

3.4.1 Analysis & results

Fig. 3.4 displays spectra from three extraction regions over the remnant situated in the N, NE and SE of the remnant. The data from *RGS 1* and *RGS 2* have been combined in order to increase the statistical weight of the observation. Several lines of highly ionized species of Si, Mg, Ne, Fe L and O are detected in the spectrum. Due to interstellar absorption no features can be measured long-ward of ~ 20 Å. The analysis and interpretation of these spectra will be the subject of a forthcoming paper.

As a first result for this paper we extracted images of the O VIII Ly- α and Ly- β lines to probe small scale variations in absorption effects over this part of the remnant and to investigate the potential presence of resonance scattering in the limb brightened shells viewed edge-on. The temperature range relevant for Cas A has no influence on the Ly-

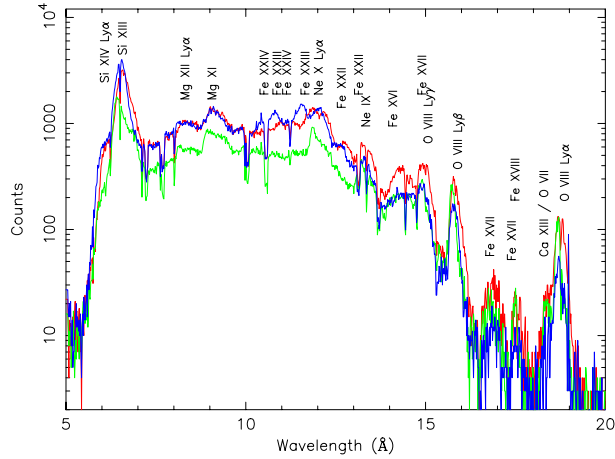


Figure 3.4: First order ($m = -1$) *RGS* spectra of Cas A for the three regions. Line identifications of the principle lines are provided.

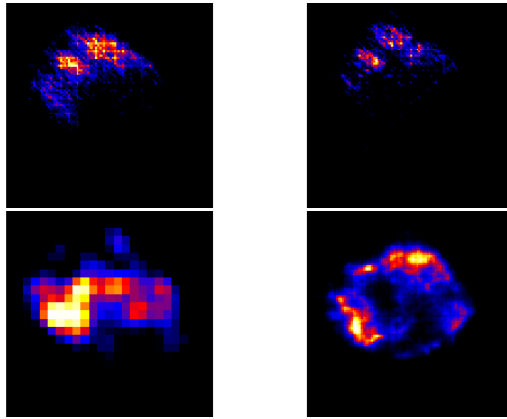


Figure 3.5: *RGS* images of O VIII Ly- β (top left) and Ly- α (top right), the dispersion direction runs from top-left to lower-right at 45 degrees with the vertical. Emission is seen in three blobs in the E and N rim. The ratio map of the Ly- β to Ly- α images is shown at the bottom left panel. The enhanced spot on the SE rim of the image indicates a Ly- α emission deficit in this region. For comparison we show a soft band *EPIC-MOS* image (0.5–1.2 keV) in the lower right panel.

$\alpha/\text{Ly-}\beta$ ratio. Since *RGS* is a slitless spectrometer it is possible to extract dispersed monochromatic images of Cas A. These images were converted from wavelength to spatial coordinates using the equation $\Delta\lambda = d \sin(\alpha)\Delta\phi$, where $\Delta\phi$ is the offset along the dispersion direction, $\Delta\lambda$ the wavelength shift, α the angle of incidence on the gratings and d the line distance of the gratings. However, any Doppler broadening is also convolved along the dispersion direction and, depending on its magnitude, Doppler broadening could distort the *RGS* images. The O VIII Ly- α and Ly- β maps are presented in Fig. 3.5. The oxygen emission is seen to originate from three blobs on the E and N rim of the remnant. The emission is faintest in the SE blob where there also seems to be a Ly- α deficit compared to Ly- β . To investigate this we produced cross-dispersion image profiles of the Ly- α and Ly- β lines by integrating over the dispersion direction. The cross-dispersion profiles together with the Ly- α to Ly- β ratio have been plotted in Fig. 3.6 (note that this is the inverse of the ratio plotted in the brightness distribution in Fig. 3.5 because of the low Ly- $\alpha/\text{Ly-}\beta$ ratio). The ratio plot seems to steepen gradually from a value of ~ 0.5 to ~ 0.15 – 0.20 , at a cross-dispersion above $+1'$. This decrease seems to indicate a Ly- α emission deficit in this region. The same effect is seen in the ratio image presented in Fig. 3.6.

3.4.2 Discussion

Three possible causes can be identified for explaining the O VIII Ly- α deficit in the SE part of Cas A, i.e. line blending, N_{H} variation and resonance scattering.

(1) A line blending effect due to the reduced spectral resolution arising from the finite source extent causes the Ly- β line to be "polluted" by neighbouring lines from the Fe-L complex. Given the limited angular extent of the bright emission region in the dispersion direction, i.e. $<1'$, and the fact that Cas A is an oxygen-rich remnant, this effect can be neglected, i.e. the oxygen emission lines strongly dominate the Fe-L lines and the spectral resolving power is still adequate ($R \sim 130$).

(2) The potential influence of variations in the column density N_{H} in this region can be assessed by using the column densities given by Keohane (1998). These data take into account both the H I and molecular absorption and have an average resolution of $30''$. In the E part of Cas A they centre at $1.10 \times 10^{22} \text{ cm}^{-2}$ with a full-width spread ranging from $1.00 - 1.20 \times 10^{22} \text{ cm}^{-2}$ (only the bright spot Cas A W shows a larger column of about $1.4 \times 10^{22} \text{ cm}^{-2}$). Applying this full range going from N (least absorbed) to the SE bright rim (most absorbed) yields a decrease of the O VIII Ly- $\alpha/\text{Ly-}\beta$ ratio of 1.4. The observed decrease of the Ly- $\alpha/\text{Ly-}\beta$ ratio, displayed in Fig. 3.6, appears to be substantially larger, i.e. a factor ≥ 3 from about 0.45 to 0.15. Smaller-scale variations could be caused by small scale structure in the N_{H} value on a $\sim 10''$ angular scale. To fully explain the decrease observed a column density variation of $6 \times 10^{21} \text{ cm}^{-2}$ (i.e. from $1.0 - 1.6 \times 10^{22} \text{ cm}^{-2}$) would have to be present, which seems rather unlikely.

(3) Alternatively a decrease in the Ly- $\alpha/\text{Ly-}\beta$ ratio could also be introduced by

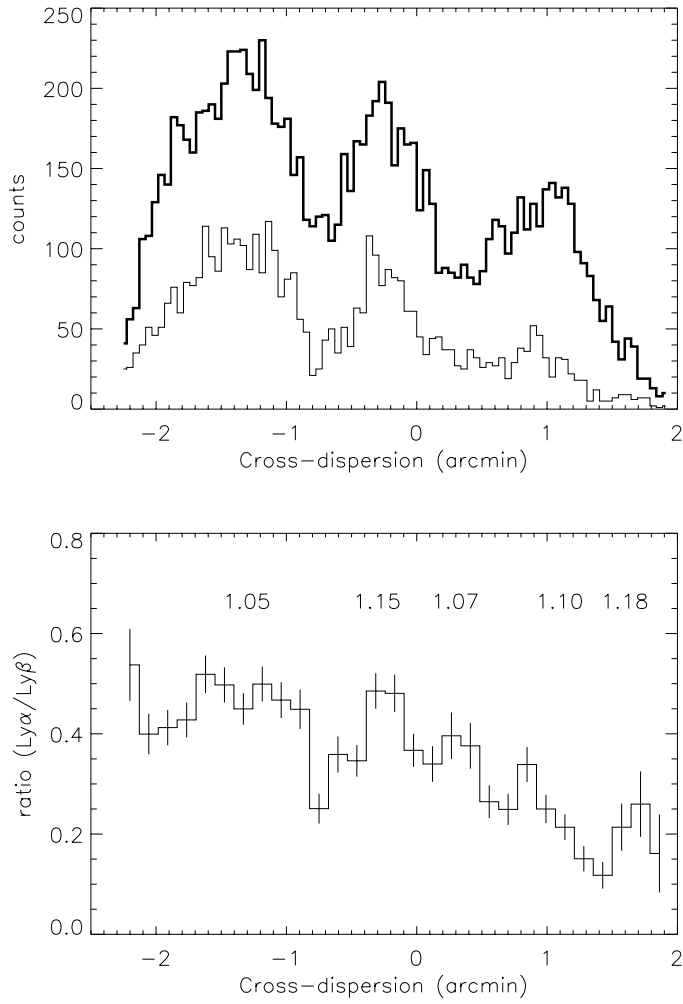


Figure 3.6: Upper panel: cross dispersion profiles of O VIII Ly- β (thick line) and O VIII Ly- α (thin line). Lower panel: ratio of Ly- α to Ly- β . Numbers indicate estimated N_{H} values from Keohane (1998), in units of 10^{22} cm^{-2} .

the presence of resonance scattering of the O VIII Ly- α photons in the X-ray bright rims if viewed edge-on (Kaastra & Mewe 1995). A factor of 2–3 reduction in Ly- α intensity can be explained by an optical depth in the Ly- α line of 2 or more (following the discussion in Kaastra & Mewe). For typical conditions in the rims of Cas A, an optical depth larger than 2 is expected to be present if the micro turbulent velocity is smaller than ~ 700 km/s.

Acknowledgements. The results presented are based on observations obtained with *XMM-Newton*, an ESA science mission with instruments and contributions directly funded by ESA Member States and the USA. We thank the referee J. Ballet for his helpful comments and suggestions.

References

- Allen G.E., Keohane J.W., Gotthelf E.V., et al., 1997, ApJ 487, L97
Asvarov A.I., Guseinov, O.H., Kasumov, F.K., Dogel', V.A., 1990, A&A 229, 196
Borkowski K.J., Sarazin C.L., & Blondin J.M., 1994, ApJ 429, 710
Chevalier, R.A., Kirshner, R.P., 1979, ApJ 233, 154
Favata F., Vink, J., dal Fiume, D., et al, 1997, A&A 324, L49
Fesen, R.A., Becker, R.H., Blair, W.P, 1987, ApJ 313, 378
Hughes, J.P., Rakowski, C.E., Burrows, D.N., Slane, P.O., 2000, ApJ 528, L109
Jansen, F.A., Lumb, D., Altieri, B. et al. 2001, A&A, 365 (this issue)
Kaastra, J.S., Mewe, R., 1995, A&A 302, L13
Keohane, J.W., 1998, Ph.D. Thesis, NASA/CR-1998-206893
Laming, J.M., 2000, accepted for ApJ (astro-ph/0008426)
Reynolds S.P., 1998, Ap.J. 493, 375
The L.-S., Leising, M.D., Kurfess, J.D., et al, 1996, A&AS 120, 357
Vink J., Maccarone, M.C., Kaastra, J.S., et al, 1999, A&A 344, 289

Chapter 4

X-ray spectral imaging and Doppler mapping of Cassiopeia A

R. Willingale, J.A.M. Bleeker, K.J. van der Heyden, J.S. Kaastra, J. Vink

Published in *Astronomy & Astrophysics* 381, 1039 (2002)

Abstract

We present a detailed X-ray spectral analysis of Cas A using a deep exposure from the *EPIC-MOS* cameras on-board *XMM-Newton*. Spectral fitting was performed on a 15×15 grid of $20'' \times 20''$ pixels using a two component non-equilibrium ionisation model (NEI) giving maps of ionisation age, temperature, interstellar column density, abundances for Ne, Mg, Si, S, Ca, Fe and Ni and Doppler velocities for the bright Si-K, S-K and Fe-K line complexes. The abundance maps of Si, S, Ar and Ca are strongly correlated. The correlation is particularly tight between Si and S. The measured abundance ratios are consistent with the nucleosynthesis yield from the collapse of a progenitor star of $12 M_{\odot}$ at the time of explosion. The distributions of the abundance ratios Ne/Si, Mg/Si, Fe/Si and Ni/Si are very variable and distinctly different from S/Si, Ar/Si and Ca/Si. This is also expected from the current models of explosive nucleosynthesis. The ionisation age and temperature of both the hot and cool NEI components varies considerably over the remnant. Accurate determination of these parameters has enabled us to extract reliable Doppler velocities for the hot and cold components. The combination of radial positions in the plane of the sky and velocities along the line of sight have been used to measure the dynamics of the X-ray emitting

plasma. The data are consistent with a linear radial velocity field for the plasma within the remnant with $v_s = 2600 \text{ km s}^{-1}$ at $r_s = 153$ arc seconds implying a primary shock velocity of $4000 \pm 500 \text{ km s}^{-1}$ at this shock radius. The Si-K and S-K line emission from the cool plasma component is confined to a relatively narrow shell with radius 100-150 arc seconds. This component is almost certainly ejecta material which has been heated by a combination of the reverse shock and heating of ejecta clumps as they plough through the medium which has been pre-heated by the primary shock. The Fe-K line emission is expanding somewhat faster and spans a radius range 110-170 arc seconds. The bulk of the Fe emission is confined to two large clumps and it is likely that these too are the result of ablation from ejecta bullets rather swept up circumstellar medium.

4.1 Introduction

In this paper we present a detailed X-ray spectral analysis of the young supernova remnant Cassiopeia A with an angular resolution of the order 20 arc seconds over a field of view covering the full remnant. The data were obtained from an 86 kilosecond exposure of the *XMM-Newton EPIC-MOS* cameras to the source. The outstanding spectral grasp of *XMM-Newton*, i.e. the combination of sensitivity, X-ray bandwidth and spectral resolving power, coupled to this very long exposure time provides ample photon statistics for a full spectral modelling of each image pixel commensurate with the beam width of the *XMM-Newton* telescopes ($\sim 15''$ Half Power Width), even for source regions of low surface brightness. This is illustrated in Fig. 4.1 which shows a broad band high resolution Chandra image of Cas A (Hughes et al. 2000) on which the pixel grid used in this analysis has been superimposed. Also drawn on this image is a contour indicating the region with good statistics and where the flux is not dominated by scattering. In addition, two samples of raw spectral data are shown, indicating the typical statistical quality in regions of high and low surface brightness.

The energy resolution, gain stability and gain uniformity of the *EPIC-MOS* cameras allows significant detection of emission line energy shifts of order 1 eV or greater for prominent lines like Si-K, S-K and Fe-K. Proper modelling of these line blends with the aid of broad band spectral fitting, taking into account the non-equilibrium ionisation balance (NEI), allows an assessment, with unprecedented accuracy, of Doppler shifts and abundance variations of the X-ray emitting material across the face of the remnant with an angular resolution adequate enough to discriminate the fine knot structure seen by Chandra. The implications for the dynamical model of the remnant and for the origin and shock heating of the X-ray emitting ejecta will be highlighted as the key result of this investigation.

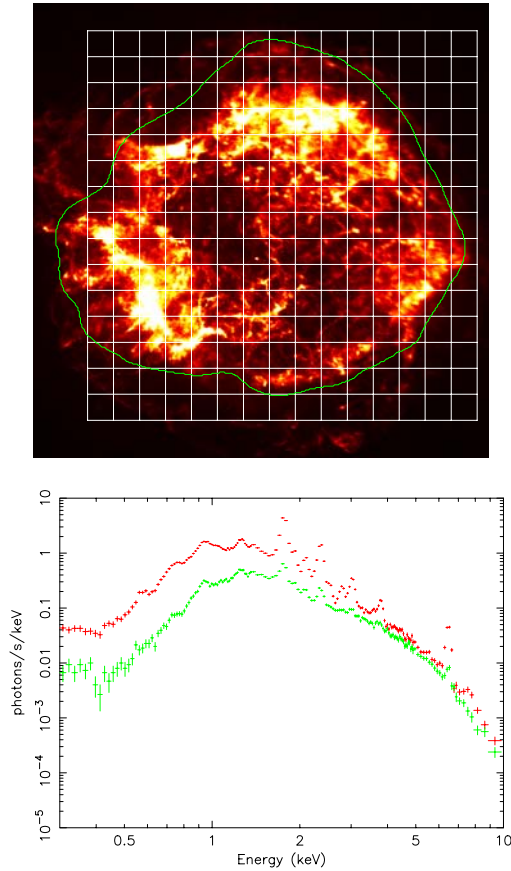


Figure 4.1: The pixel grid used in our analysis superimposed on the high angular resolution Chandra image of Cas A. The green contour indicates the region with good statistics and low scattering. Below are typical single pixel spectra from a high count and a low count region.

4.2 Spectral Fitting Analysis

We divided a $5' \times 5'$ field of view of Cas A on a spatial grid containing 15×15 pixels. This corresponds to a pixel size of $20'' \times 20''$, slightly larger than the half-power beam width of *XMM-Newton*. Spectra were extracted using this grid and analysed on a pixel by pixel basis.

The spectral analysis was performed using the SRON SPEX (Kaastra et al. 1996) package, which contains the MEKAL code (Mewe et al. 1995) for modeling thermal emission. We find that, even at the $20'' \times 20''$ level, one thermal component does not model the data sufficiently well, particularly in describing both the Fe-L and Fe-K emission. We therefore choose as a minimum for representative modelling two NEI components for the thermal emission. In addition we incorporated the absorption measure as a free parameter and also introduced two separate Doppler-shift parameters, one for each plasma component.

The basic rationale behind a two component NEI model is that we expect low and high temperature plasma associated with a reverse shock and a blast wave respectively. While we obtain good fits using a two NEI model, we estimate that a contribution from a power law hard tail to the 4-6 keV continuum could be as high as 25%. Since there is no evidence that the hard X-ray emission is synchrotron and its brightness distribution is very much in line with the thermal component (see Bleeker et al. 2001), we feel that our fitting procedure is justified. In other words the combined high and low temperature NEI components will provide a good approximation to the physical conditions that give rise to the line emission.

The low temperature plasma component in our model implicitly assumes that the ejecta material, which largely consist of oxygen and its burning products (Chevalier & Kirshner 1997), has been fully mixed regarding the contributing atomic species. In order to mimic a hydrogen deficient, oxygen rich medium we adopted a similar approach to that used by Vink et al. (1996), where they fixed the oxygen abundance of the cool component to a high value. We set the cool component abundances of O, Ne, Mg, Si, S, Ar and Ca to a factor 10000 higher than that of the hot component. It should be noted that 10000 is not a magic number, 1000 would suffice. The important point is that oxygen and the heavier elements are all dominant with respect to hydrogen so that oxygen rather than hydrogen is the prime source of free electrons in the plasma. The abundances of O, Ne, Mg, Si, S, Ar, Ca, Fe and Ni were allowed to vary over the remnant while the rest of the elemental abundances (He, C and N) were fixed at their solar values (Anders & Grevese 1989).

Our model allows us to estimate the distribution over the remnant of the emission measure $n_e n_H V$, the electron temperature T_e and the ionisation age $n_e t$ of the two NEI components as well as the distribution of the abundance of the elements (O, Ne, Mg, Si, S, Ar, Ca, Fe & Ni), the column density N_H of the absorbing foreground material, Doppler broadening of the lines and the redshift of the respective plasma components. Here n_e and n_H are the electron and hydrogen density respectively, V is the volume occupied by the plasma and t is the time since the medium has been shocked. The best fit model parameters were found and recorded for each pixel and it was thus possible to create maps of the various model parameters over the face of the remnant.

Table 4.1: Estimates of the mean errors associated with determining the Doppler velocities. ΔV is the mean statistical error in the Doppler velocity estimated from the two dominant factors and ΔV_{NEI} is the rms of the systematic correction provided by the NEI modelling.

line	E_{pband} keV	ΔE_{N} eV	ΔE_{C} eV	ΔV km s ⁻¹	ΔE_{NEI} eV	ΔV_{NEI} km s ⁻¹
Si-K	1.847	0.55	0.53	94	3.89	630
S-K	2.439	0.31	0.53	99	2.52	310
Fe-K	6.566	2.95	1.60	143	24.2	1115

4.3 Doppler mapping

It is possible to accurately determine the Doppler shifts of Si-K, S-K and Fe-K since these lines are strong and well resolved. Doppler shifts of these lines have been calculated in two different ways.

After fits were made to the full spectrum we froze all the fit parameters. We selected the Si-K (1.72-1.96 keV), S-K (2.29-2.58 keV) and Fe-K (6.20-6.92 keV) bands for determining their respective Doppler velocities while ignoring all other line emission. We then do a fit to each line separately by starting from the full fit model parameters as a template and subsequently allowing only the redshift and the abundance of the relevant element to vary. This method provides a fine tuning of the redshift which in turn gives the Doppler velocity of the element under scrutiny.

Alternatively, using the same fit parameters we calculated the predicted continuum flux, F_{pcont} , and energy centroid of the lines, E_{pline} and energy centroid of the continuum, E_{pcont} , for each line energy band in each pixel. Then using the raw events we calculated the measured total flux, F_{band} and energy centroid E_{band} in each band again for each pixel. The measured line flux was then estimated by subtracting the predicted continuum from the total flux in each band, $F_{\text{line}} = F_{\text{band}} - F_{\text{pcont}}$. The continuum centroid in a line energy band varies as a function of position over the remnant and the energy centroid for each band is the weighted sum of the line and continuum components. The measured line energy centroid was calculated by removing the contribution from the continuum.

$$E_{\text{line}} = (F_{\text{band}} \times E_{\text{band}} - F_{\text{pcont}} \times E_{\text{pcont}}) / F_{\text{line}}$$

An estimate of the Doppler shift of the line is then given by $\Delta E = E_{\text{line}} - E_{\text{pline}}$.

The Doppler shifts calculated by these two methods were in reasonable agreement indicating that the results were not sensitive to line broadening and lines close to the edges of the chosen energy bands.

The accuracy of the Doppler shift values depends on the ability of the NEI spectral model to predict the line blends combined with the uncertainties in the gain calibra-

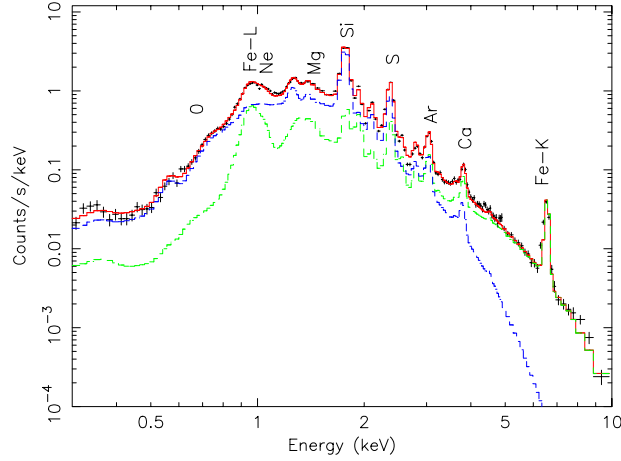


Figure 4.2: An example of a spectral fit within a single $20'' \times 20''$ pixel - cool component in blue, hot component in green and full model in red.

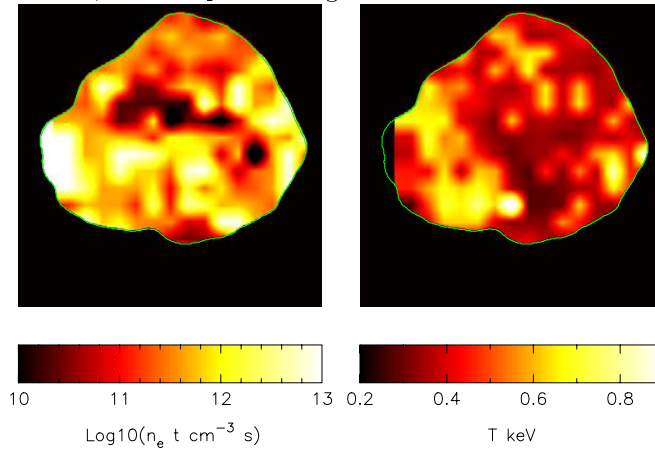


Figure 4.3: Spectral fit parameters for the cool component, ionisation age left-hand panel and temperature right-hand panel. The contour indicates the region with good statistics and low scattering.

tion of the detectors. Maps were constructed using the combined counts from the two cameras *EPIC-MOS 1* and *EPIC-MOS 2*. The results were the same but with some-

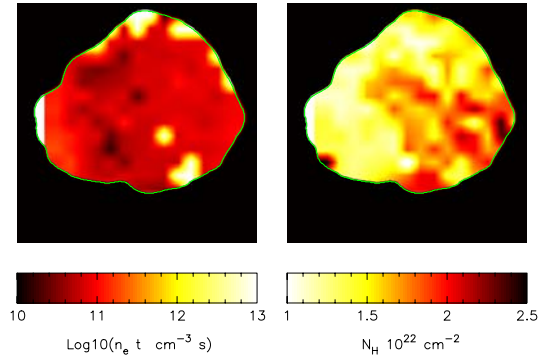


Figure 4.4: Ionisation age of the hot component and the interstellar column density. The contour indicates the region with good statistics and low scattering.

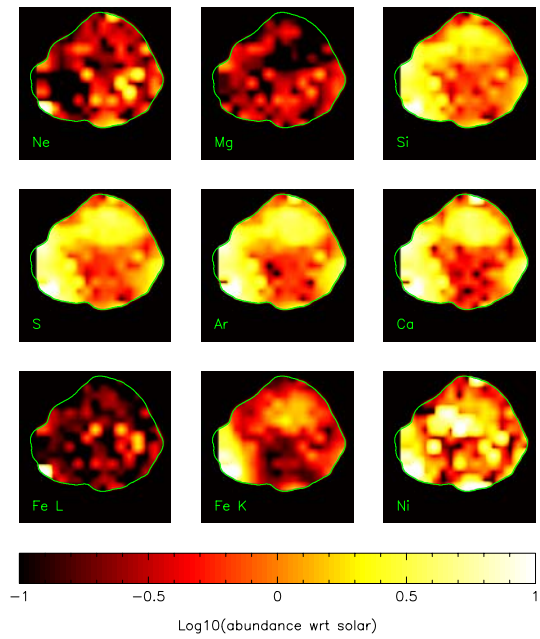


Figure 4.5: Abundance maps for the elements included in the spectral fitting. All are plotted on the logarithmic scale indicated by the bar at the bottom.

what poorer statistics if only *EPIC-MOS 1* or *EPIC-MOS 2* were used. The readout directions of the central CCDs of *EPIC-MOS 1* and *EPIC-MOS 2* are set perpendicular to one another on the sky so we are sure that the line shifts are not due to systematic charge transfer losses as the events are read out. Thus there is convincing evidence that the observed line shifts are not due to instrumental gain variations or some other more subtle detector effect. Fig. 4.2 shows a typical spectral fit. All features of the measured spectrum are remarkably well represented by the modelling.

The statistical errors on the velocity estimates depend on the intrinsic energy resolution of the detectors, the number of counts detected in the line energy band and the error associated with estimating the continuum contribution in the line energy band. There are two dominant factors. Firstly the statistical error in determining the energy centroid $\Delta E_N \approx \sigma_E / \sqrt{N}$ where σ_E is the rms width of the detector energy resolution at the line energy and N is the total detected count. Secondly the statistical errors in the continuum bands which translate into errors in the temperature and flux determination for the continuum flux and hence yield a centroid error ΔE_C .

Systematic errors on the Doppler velocities are introduced by improper modelling of the unresolved emission line blends within the Si-K, S-K and Fe-K line energy bands. The centroids of the line blends vary considerably over the remnant because of large differences in temperature and ionisation age. We have calculated the rms variation ΔE_{NEI} of the band centroid $E_{p_{band}}$ over the remnant. If the spectral modelling is correct then this systematic error should have been eliminated.

Estimates of the factors affecting the accuracy of the Doppler velocities over the remnant are given in Table 4.1. The velocity error ΔV was calculated from the combination of the two statistical components. The velocity errors do vary over the face of the remnant since they depend on the surface brightness but for all the bright knots the errors in Table 4.1 are a good estimate.

4.4 Key results

Bivariate linear interpolation was used to transfer the model parameters, predicted fluxes etc. onto the grid of 1 arc second pixels. Fig. 4.3 displays maps of the ionisation age and temperature of the cool NEI component. This component is dominant in the line spectrum including Fe-L emission. The temperature distribution of the hot component is similar to (but not the same as) the cool component but with a temperature range 2-6 keV. The hot component is responsible for all the Fe-K emission and also dominates the continuum above 4 keV. Fig. 4.4 shows the ionisation age of the hot NEI component and the interstellar column density. These plots demonstrate the amazing variability in the spectrum over the face of the remnant. The column density does exhibit some correlation with the surface brightness of the bright knots of the remnant presumably because of parameter coupling in the spectral fitting process. The N_H fitting is particularly sensitive to modelling of the O VIII emission 0.6-0.8

keV and Fe-L lines 1.0-1.5 keV. The mean column density is $1.5 \times 10^{22} \text{ cm}^{-2}$ while the range is $1.0 - 2.5 \times 10^{22} \text{ cm}^{-2}$. The variation of interstellar column density over the face of the remnant has previously been mapped by Keohane et al. (1996) using radio data. The distribution in their map is similar to Fig. 4.4 with high column density in the West due to a molecular cloud but the overall range of their column density derived from the equivalent widths of HI and OH is smaller, $1.05 - 1.26 \times 10^{22} \text{ cm}^{-2}$.

Fig. 4.5 is a montage of abundance maps. Again we see considerable variations over the remnant. The Fe-L distribution comes from the cool component while the Fe-K and Ni are derived exclusively from the hot component. The distributions of Si, S, Ar and Ca, which are all oxygen burning products, are similar and distinct from carbon burning products, Ne and Mg, and Fe-L. Fig. 4.6 shows the variation in the ratios S/Si, Ar/Si and Ca/Si with respect to the abundance of Si. On the one hand these ratios clearly vary over the remnant but on the other hand, for a Si abundance range spanning more than two orders of magnitude, these ratios remain remarkably constant. The thick vertical bars indicate the mean and rms scatter of the ratio values.

Line flux images were produced using an adaptive filter with a minimum beam count of 400 and maximum beam radius of 15 arc seconds. The raw event images from each line energy band were smoothed and then multiplied by the ratio of the predicted line flux to line plus continuum flux ratio in order to estimate the line flux. Fig. 4.7 shows the resulting line flux images colour coded with the Doppler velocity. The bottom left image is the colour coding used. The Doppler shifts seen in different areas of the remnant are very similar in the three lines. The knots in the South East are blue shifted and the knots in the North are red shifted. This is consistent with previous measurements, Markert et al. (1983), Holt et al. (1994), Vink et al. (1996). Moving from large radii towards the centre the shift generally gets larger as expected in projection. This is particularly pronounced in the North. At the outer edges the knots are stationary or slightly blue shifted. Moving South a region of red shift is reached indicating these inner knots are on the far side of the remnant moving away from us. The distributions of flux as a function of Doppler velocity are shown in Fig. 4.8. The distributions for Si-K and S-K are very similar. The Fe-K clearly has a slightly broader distribution for the red shifted (+ve) velocities. The lower panel is the flux plotted in the Si velocity-S velocity plane showing the tight correlation between the Doppler shift measured for these lines. This plot was quite sensitive to small systematic changes in temperature, ionisation age or abundances in the spectral fitting since these can potentially have a profound effect on the derived Doppler velocities as indicated by the large values of ΔV_{NEI} in Table 4.1.

The X-ray knots of Cas A form a ring because the emitting plasma is confined to an irregular shell. We searched for a best fit centre to this ring looking for the position that gave the most strongly peaked radial brightness distribution (minimum rms scatter of flux about the mean radius). The best centre for the combined Si-K, S-K and Fe-K line image was 13 arc second West and 11 arc seconds North of the image

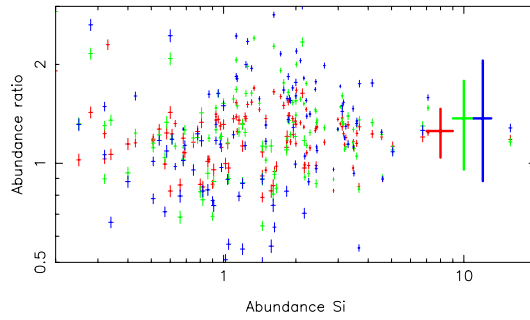


Figure 4.6: The variation in the abundance ratios of S/Si red, Ar/Si green and Ca/Si blue as a function of the Si abundance. The large error bars to the right indicate the mean and rms scatter for the three elements.

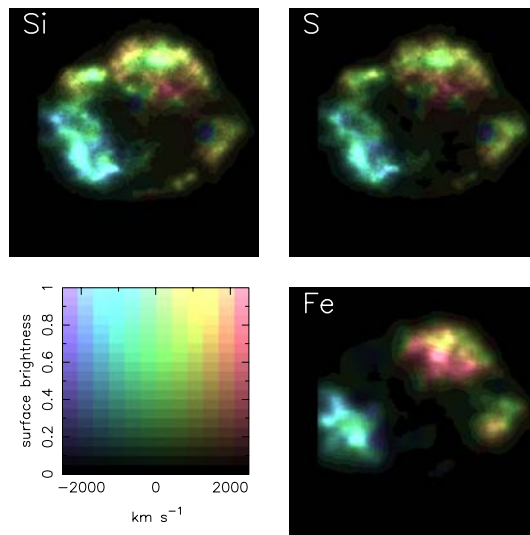


Figure 4.7: Doppler maps derived from Si-K, S-K and Fe-K emission lines. For each case the surface brightness of the line emission (after subtraction of the continuum) is shown colour coded with the Doppler velocity. The coding used is shown in the bottom left image.

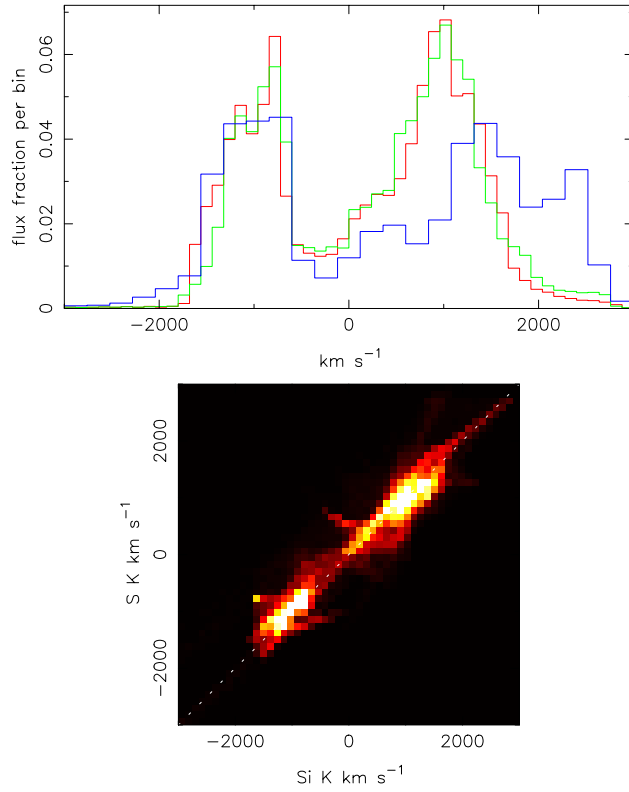


Figure 4.8: Flux distributions of Si-K (red), S-K (green) and Fe-K (blue) as a function of measured Doppler velocity. The lower panel shows the flux distribution in the Si velocity-S velocity plane.

Table 4.2: Mean measured abundance ratios and rms scatter compared with theoretical predictions for progenitor masses of 11, 12 and 13 M_{\odot} .

ratio	mean	rms	11 M_{\odot}	12 M_{\odot}	13 M_{\odot}
O/Si	1.69	1.37	0.44	0.16	0.33
Ne/Si	0.24	0.37	0.59	0.12	0.33
Mg/Si	0.16	0.15	0.57	0.12	0.41
S/Si	1.25	0.24	0.87	1.53	0.88
Ar/Si	1.38	0.48	0.65	2.04	0.64
Ca/Si	1.46	0.68	0.63	1.62	6.56
FeL/Si	0.19	0.65	1.37	0.23	0.96
FeK/Si	0.60	0.51	1.37	0.23	0.96
Ni/Si	1.67	5.52	6.89	0.68	1.80

centre (the central Chandra point source). Using this centre the peak flux occurred at a radius of 102 arc secs, the mean radius was 97 arc secs and the rms scatter about the mean radius was 24 arc seconds.

Given such a centre we can assign a radius to each pixel and using the Doppler velocity measured for each pixel we can map the flux into the radius-velocity plane. The result is shown in Fig. 4.9.

4.5 Ionisation structure and abundance ratios

The models for nucleosynthesis yield from massive stars predict that the mass or abundance ratio $R_{X/Si}$ of ejected mass of any element X with respect to silicon varies significantly as a function of the progenitor mass M . We show the observed mean values of $R_{X/Si}$ as well as its rms variation in Table 4.2, together with the predictions for models with a progenitor mass of 11, 12 and 13 M_{\odot} . The observed abundance ratios for X equal to Ne, Mg, S, Ar, Ca and Fe-L (the iron of the cool component) are all consistent with a progenitor mass of $12.0 \pm 0.6 M_{\odot}$, where we used the grid of spherically symmetric models by Woosley and Weaver (1995). In these models, most of the Si, S, Ar and Ca comes from the zones where explosive O-burning and incomplete explosive Si-burning occurs, and indeed as Fig. 4.6 shows these elements track each other remarkably well. Furthermore the average abundance ratio fits the expectation for a 12 M_{\odot} progenitor. The correlation between Si and S is remarkably sharp but not perfect, the scatter in Fig. 4.6 is real. These remaining residuals can be attributed to small inhomogeneities. Table 4.2 also indicates that the rms scatter of the abundances with respect to Si get larger as Z increases, S to Ar to Ca and indeed through to Fe and Ni. This is to be expected since elements close together in Z are produced in the same layers within the shock collapse structure while those of very

different Z are produced in different layers and at different temperatures.

The Fe which arises from complete and incomplete Si burning should give rise to iron line emission. For both the Fe-L and Fe-K lines we see that iron abundance varies over the remnant but does not show any straightforward correlation with the other elements (there is a very large scatter in $R_{\text{Fe/Si}}$). This is to be expected if most of the iron arises from complete Si burning. We return to the different morphologies of Si and Fe later in the discussion.

Ne and Mg are mostly produced in shells where Ne/C burning occurs, and the relative scatter in terms of $R_{\text{X/Si}}$ is indeed much larger than for S, Ar and Ca (Table 4.2). Furthermore the abundance maps of Ne and Mg in Fig. 4.5 are similar and very different from the Si, S, Ar and Ca group.

The oxygen abundance is much higher than predicted by theory, contrary to all other elements. We cannot readily offer an explanation for this, but there are at least two complicating factors. As the XMM RGS maps show (Fig. 3.5), oxygen has a completely different spatial distribution to the other elements (it is more concentrated to the North), and it is also much harder to measure due to the strong galactic absorption and relatively poor spectral resolution of the EPIC cameras at low energies.

The map of the ionisation age of the cool component shows a large spread. The average value at the Northern rim (few times $10^{11} \text{ cm}^{-3}\text{s}$) matches nicely the value derived from ASCA data (Vink et al. 1996). At the SE rim the ionisation age is much larger (cf. Vink et al. $4 \times 10^{11} \text{ cm}^{-3}\text{s}$). We confirm this higher value, but also see that there is a large spread in ionisation age. It should also be noted that for ionisation ages larger than about $10^{12} \text{ cm}^{-3}\text{s}$ the plasma is almost in ionisation equilibrium and therefore the spectra cannot be distinguished from equilibrium spectra; the extremely high values of $10^{13} \text{ cm}^{-3}\text{s}$ in the easternmost part of the remnant (Fig. 4.3) are therefore better interpreted as being just larger than $10^{12} \text{ cm}^{-3}\text{s}$. There is also a region of very low ionisation age (less than $3 \times 10^{10} \text{ cm}^{-3}\text{s}$) stretching from East to West just above the centre of the remnant. This region also has a very low emissivity (i.e. low electron density) and can be understood as a low density wake just behind and inside of the shocked ejecta.

The hot component has a more homogeneous distribution of ionisation age, centered around $10^{11} \text{ cm}^{-3}\text{s}$, again consistent with the typical value found by Vink et al. (1996) but in that case integrated over much larger areas. We have now clearly resolved this component spatially.

4.6 Dynamics

In the radius-velocity plane the flux from a thin shell of radius r_s expanding at velocity v_s is expected to form an ellipse which intersects the radius axis at r_s and the velocity axis at $\pm v_s$. We expect the velocity to increase with radius and for simplicity we can assume that the velocity field within the spherical volume is given by a linear form

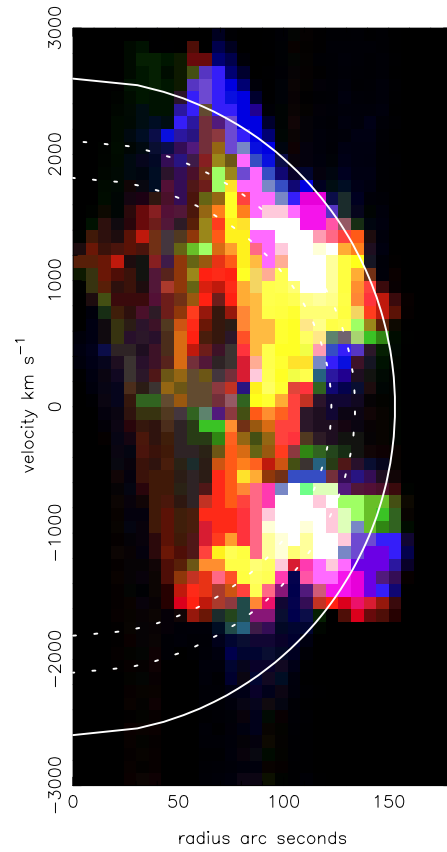


Figure 4.9: Flux distribution of Si-K (red), S-K (green) and Fe-K (blue) in the radius-velocity plane. The solid line is the best fit shock radius (see text). The outer dotted line indicates the peak of the Fe-K flux distribution and the inner dotted line indicates the mean radius of the Si-K and S-K emission.

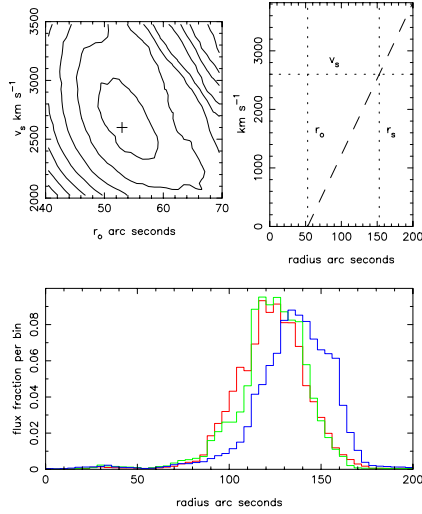


Figure 4.10: The velocity field which gives the minimum normalised shell thickness $\Delta r/r$. Each contour interval in the top left plot corresponds to a $\sim 2\%$ increase in shell thickness. The lower panel shows the deprojected flux distribution of Si-K (red), S-K (green) and Fe-K (blue) as a function of radius from the centre of the remnant.

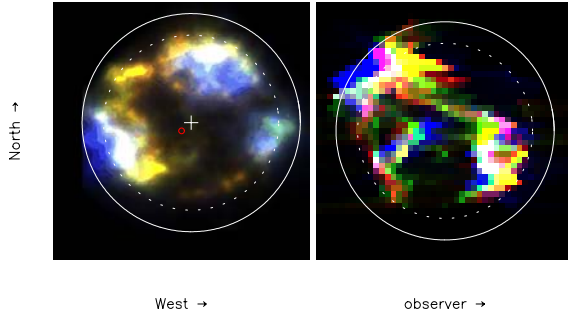


Figure 4.11: The left-hand panel is an image of Si-K (red), S-K (green) and Fe-K (blue). The small red circle indicates the position of the Chandra point source. The white cross is the best fit centre from the fitting of the radial distribution. The right-hand panel is a reprojection of the same line fluxes onto a plane containing the line of sight, North up, observer to right. In both panels the outer solid circle is the shock radius $r_s = 153$ arc seconds and the inner circle is the mean radius of the Si-K and S-K flux.

$$v(r) = \frac{v_s}{(r_s - r_o)}(r - r_o)$$

where v_s is the postshock velocity of material at the shock radius r_s and r_o is the radius within the remnant at which the velocity falls to zero. From the analysis of the Chandra data, (Gottlieb et al. 2001), we have an estimate of $r_s = 153$ arc seconds. Adopting such a spherically symmetric velocity field precludes the possibility that the expansion is wildly asymmetric. In the plane of the sky the outer shock seen both in radio and X-ray images is remarkably circular (see for example the Chandra X-ray image scaled to highlight the faint outer filaments, Gottlieb et al. 2001). We therefore think it is unlikely that the velocity field or shock radius is very different along the line of sight. Assuming values for v_s and r_o we can calculate the radius of each pixel within the spherical volume from the observed radius on the plane of the sky and the Doppler velocity (along the line of sight). As the parameters are changed so the fractional rms scatter, $\Delta r/r$, of the flux about the mean radius varies. The top left panel of Fig. 4.10 shows the variation in $\Delta r/r$ as a function of r_o and v_s .

The minimum scatter of 0.16 is found at $r_o = 53$ arc seconds and $v_s = 2600$ km s^{-1} . The velocity field which gives the minimum shell thickness is shown in the top right-hand panel. This result is very similar to the velocity field of an isothermal blast wave, Solinger et al. (1975), but we would like to stress this does not imply that Cas A has entered this phase of its evolution. The remnant is almost certainly in between the ejecta-dominated and the Sedov-Taylor stages as modelled in detail by Truelove and McKee (1999). The lower panel of Fig. 4.10 shows the deprojected flux distributions as a function of radius in the spherical volume. The Si-K and S-K distribution match quite closely. The Fe-K distribution is somewhat broader and peaks at a larger radius. The deprojected Si-K and S-K flux distributions are very similar to the emissivity profiles derived from the Chandra data (Gottlieb et al. 2001) although their analysis was for a section of the remnant while the profiles in Fig. 4.10 are the average over the full azimuthal range. The solid semi-circular line in Fig. 4.9 is the best fit with $r_s = 153$ arc seconds and $v_s = 2600$ km s^{-1} . The inner dotted line shows the mean radius of the combined Si-K and S-K flux and the outer dotted line shows the peak of the Fe-K distribution. The outer reaches of the Fe-K distribution straddle the shock radius derived from the Chandra image.

The *EPIC-MOS* energy resolution cannot separate the red and blue components when they overlap. If we see both the distant red shifted shell and nearer blue shifted shell in the same beam the line profile is slightly broadened but the centroid shift is diminished. The observed Doppler velocities and the best fit value for v_s may be slightly biased by this ambiguity, however most beams appear to be dominated by either red or blue shifted knots and therefore this bias is expected to be small. It is fortuitous that the X-ray emission is distributed in clumps rather than a thin uniform shell since this enables us to measure the Doppler shift with a modest angular

resolution without red and blue components in the same beam cancelling each other out.

The left-hand panel of Fig. 4.11 is a composite image of the remnant seen in the Si-K, S-K and Fe-K emission lines. The solid circle indicates the $r_s = 153$ arc seconds and the dashed circle is the mean radius of the Si-K and S-K flux $r_m = 121$ arc seconds. The X-ray image of the remnant provides coordinates x-y in the plane of the sky. Using the derived radial velocity field within the remnant we can use the measured Doppler velocities v_z to give us an estimate of the z coordinate position of the emitting material along the line of sight thus giving us an x-y-z coordinate for the emission line flux in each pixel. Using these coordinates we can reproject the flux into any plane we choose. The right-hand panel of Fig. 4.11 shows such a projection in a plane containing the line-of-sight, North upwards, observer to the right. In this reprojection the line emission from Si-K, S-K and Fe-K are reasonably well aligned for the main ring of knots. The reprojection is not perfect because the *EPIC-MOS* cameras are unable to resolve components which overlap along the line-of-sight and this produces some ghosting just North of the centre of the remnant. In the plane of the sky Fe-K emission (blue) is clearly visible to the East between the mean radius of the Si+S flux and the shock radius. Similarly in the reprojection Fe-K emission is seen outside the main ring in the North away from the observer. The Si+S knot in the South away from the observer in the reprojection is formed from low surface brightness emission in the South West quadrant of the sky image. The X-ray emitting material is very clumpy within the spherical volume and is indeed surprisingly well characterised by the doughnut shape suggested by Markert et al. (1983). However the distribution is distinctly different to that obtained in similar 3-D studies of the optical knots, Lawrence et al. (1995).

The expansion of Cas A has been measured in various ways; using the proper motion of optical knots (van den Bergh and Kamper 1983, Fesen et al. 1987, Fesen et al. 1988), from the proper motion of radio knots (Anderson and Rudnick 1995), using Doppler shifts of spectral lines from optical knots (Reed et al. 1995, Lawrence et al. 1995), Doppler shift of X-ray line complexes (Markert et al. 1983, Holt et al. 1994 and Vink et al. 1996) and the proper motion of X-ray knots (Vink et al. 1999). These methods identify a number of distinct features with different dynamics; Quasi Stationary Flocculi (optical QSF), Slow Radio Knots in the South West (SRK), the main ring of radio knots, the main ring of X-ray knots (continuum + lines 1-2 keV), Fast Moving Knots (optical FMK) and Fast Moving Flocculi (optical FMF).

In proper motion studies it is conventional to express the motion as an effective expansion time $t_{ex} = R/V$ (years) where R is the radius of the feature/knot from some chosen centre (arc seconds) and V is the proper motion (arc secs/year). The deceleration parameter, the ratio of the true age over the expansion age, can be estimated as $m = t_{age}/t_{ex}$. There is no need to deproject the radius or velocity to estimate m . However if we then wish to estimate a true expansion velocity the R must be deprojected but still the ratio R/V will remain constant. Doppler measurements allow some form

of deprojection and measured radii on the sky can be converted to actual radii within the volume of the remnant as described in the previous section. Given a radius in arc seconds r_{as} and velocity in km s^{-1} v_{kms} we can calculate an expansion time in years t_{ex} assuming a distance in kpc d_{kpc} , $t_{\text{ex}} = 4.63 \times 10^3 r_{\text{as}} d_{\text{kpc}} / v_{\text{kms}}$. Previous authors have used combinations of these measurements to refine estimates of the age and/or distance. Alternatively we can adopt some age and distance and compare the radii and expansion velocities of the various components. The original explosion probably occurred in 1680 (Ashworth 1980) so the age in 2000 is $t_{\text{age}} = 320$ years. Distance estimates have varied over the years but recent studies (Reed et al. 1995) have settled on $3.4_{-0.1}^{+0.3}$ kpc.

Table 4.3 gives estimates of the expansion parameters for the different components. Those marked with an asterisk are from proper motion studies which estimate the expansion time or the deceleration parameter directly. For these the r_{as} value has been estimated and the v_s calculated using the measured expansion time. From the Doppler measurements we get a measurement of r_s and v_s which are then used to estimate the expansion time or the deceleration parameter. Proper motion studies of X-ray emission track the movement of shock features in the plane of the sky while X-ray emission line Doppler measurements estimate the velocity of the postshock plasma v_s along the line of sight. The shock velocity u_s is related to the postshock plasma velocity, $v_s = \alpha u_s$. The factor α depends on the thermodynamics of the shocked gas but ranges between 0.58 for isothermal to 0.75 for adiabatic conditions, see for example Solinger et al. (1975). The present X-ray emission line (Xline) results in Table 4.3 have been calculated from the derived velocity field parameters, $r_s = 153$ and $v_s = 2600$ using a mean value of $\alpha = 0.65$. The error quoted reflects the uncertainty in this factor. The FMF are at large radii so it is likely that the deprojection correction is small and the value of 168 arc secs quoted is in fact the mean radius in the plane of the sky. For the SRK in the South West sector and the QSF the values quoted for r_s are just reasonable guesses. The expansion time and deceleration parameters derived from the observed Doppler shifts of the Si-K, S-K and Fe-K lines (Xline in Table 4.3) are in reasonable agreement with the radio proper motion observations (Anderson and Rudnick, 1995) and in good agreement with the soft X-ray proper motion measurements of Vink et al. (1999) (1 keV in Table 4.3).

4.7 Discussion

The tight correlation between the variation in abundance of Si, S, Ar, Ca over an absolute abundance range of two orders of magnitude is strong evidence for the nucleosynthesis of these ejecta elements by explosive O-burning and incomplete explosive Si-burning due to the shock heating of these layers in the core collapse supernova. Full mixing of the burning products is implied by the excellent fit to the plasma model. However the Fe emission, both in the Fe-K and the Fe-L lines, does not show this

Table 4.3: The expansion parameters for radio, optical and X-ray emissions. * indicates proper motion studies. The results from this paper are given in the line labelled Xline (see text for details).

	v_{kms}	r_{as}	t_{ex}	m
QSF*	370 ± 300	~ 105	4470 ± 2300	0.07 ± 0.06
SRK*	656 ± 16	~ 100	2100 ± 360	0.15 ± 0.02
Radio*	2848 ± 100	~ 110	604 ± 12	0.51 ± 0.02
Xline	4000 ± 500	153 ± 5	537 ± 70	0.60 ± 0.07
1 keV*	3456 ± 105	~ 110	501 ± 15	0.63 ± 0.02
FMK	5290 ± 90	105 ± 1	312 ± 9	0.98 ± 0.03
FMF*	8816 ± 28	168 ± 6	300 ± 9	0.99 ± 0.03

correlation in any sense. A significant fraction of the Fe-K emission is seen at larger radii than Si-K and S-K as convincingly demonstrated in our Doppler derived 3-D reprojection, Fig. 4.11. Moreover the Fe-K emission is patchy, reminiscent of large clumps of ejecta material, rather than shock heated swept up circumstellar material. In fact the bulk of the Fe-K emission arises in two limited regions possibly indicating that the core collapse threw off material in two opposing clumps which we clearly see in Fig. 4.11. If we interpret these Fe-rich ejecta as the nucleosynthesis product of complete explosive burning of the Si-layer, spatial inversion of the O- and Si-burning products has occurred and large scale bulk mixing of the explosion products is an inevitable consequence. A similar conclusion was obtained by Hughes et al. (2000) for ejecta material at the east side of the remnant based on the morphological features of the high spatial resolution Chandra data.

The largely bi-polar distribution of the Fe-K emission and, to some degree, the Si-K and S-K emission may indicate that the original explosion was aspherical, possibly with axial symmetry. The recent jet-induced models of Khokhlov et al. (1999) and Höflich et al. (2001) produce a butterfly-shaped density profile for the heavier elements a few hundred seconds after the explosion and this might evolve into a distribution similar to our present results. Therefore the progenitor mass estimate of $12 M_{\odot}$ derived from the spherically symmetric models of Woosley and Weaver (1995) may be inappropriate and the mass could be significantly larger.

The Fe-K emission requires a relatively high temperature in the range 2-6 keV. This temperature cannot be generated by the reverse shock wave, but only by the primary blast wave. Heating is certainly provided by the primary shock but preheating of the ambient medium by clumps that move ahead of the primary shock could contribute, see Hamilton (1985).

In the plane of the sky image Fig. 4.11 the Fe-K emission to the East is at a radius of 140 arc seconds, near the primary shock, with an implied shock velocity

of u_s in the range 3500-4500 km s^{-1} (see previous section). It is coincident with a cluster of three FMFs, 4,5,6 listed by Fesen et al. (1988). They all have a proper motion of 0.52 ± 0.05 arc secs yr^{-1} and a mean radius from the expansion centre in 1976 of 149 ± 3 arc seconds. Assuming a distance of 3.4 kpc and age in 1976 of 296 years this corresponds to a transverse velocity of 8170 ± 790 km s^{-1} and a deceleration parameter of $m = 1.0 \pm 0.1$. The same Fe-K emission is also coincident with the radio knots 89,90,92 and 93 listed by Anderson and Rudnick (1995). These have a mean proper motion of 0.26 ± 0.01 arc secs yr^{-1} and a mean radius from the expansion centre in 1987 of 136 ± 3 arc seconds. This corresponds to a transverse velocity of 4117 ± 160 km s^{-1} and a deceleration parameter of $m = 0.59 \pm 0.02$. These radio knots also correspond to the bow shock feature D identified using morphology and polarimetry by Braun, Gull & Perley (1987). They estimate the Mach number of this feature as 5.5, the highest in their list of 11 such features.

The Fe-K emission at large radii is highly reminiscent of SNR shrapnel discovered by Aschenbach et al. (1995) around the Vela SNR. These are almost certainly bullets of material which were ejected from the progenitor during the collapse and subsequent explosion. They would initially be expected to have a radial velocity less than the blast wave but as the remnant develops, and the shock wave is slowed by interaction with the surrounding medium, the bullets would overtake the blast wave and appear outside the visible shock front as is the case in Vela. It was suggested by Aschenbach et al. (1995) that the X-ray emission from the Vela bullets arises from shock-heating of the ambient medium by supersonic motion. If this is the case the X-rays will be seen from Mach cones which trail the bullets extending back towards the centre of the remnant.

The generation of radio emission associated with the deceleration of ejecta bullets has been discussed at length by several authors, Bell (1977), Braun, Gull & Perley (1987), Anderson and Rudnick (1995). The optical emission arises from shocks penetrating dense ejecta clumps. When these internal shocks have crossed the clump deceleration sets in accompanied by a strong turn-on of radio synchrotron emission. Electrons are accelerated in the bow-shock and the magnetic field is amplified in shearing layers between the dense ejecta and the external medium. The amplified magnetic field in the wake of ejecta bullets is predominately radial in agreement with radio polarization measurements, Anderson, Keohane and Rundick (1995). The supersonic flow associated with this scenario has been simulated by Coleman & Bicknell (1985). The same situation could also give rise to X-ray emission. The bulk of the electrons are heated to ~ 3 keV by the bow shock. As the shocked material drifts back into the wake the plasma slowly comes into ionization equilibrium and X-ray line emission is produced. Our analysis of the abundances clearly indicates that the matter responsible for the line emission is ejecta and this must have been ablated from the bullets rather than swept up by the shock. The velocities of both the radio and X-ray emission in the East are about half that of the optical. This is consistent with the peak of the radio and X-ray emission falling in the wake of the bullet trailing behind the peak of

the optical emission.

What is the heating mechanism responsible for the cool component? Our present analysis clearly indicates this component is dominated by ejecta material. It is conventional to assume that the primary source of ejecta heating which produces the bright ring of X-ray emission in Cas A is the reverse shock (McKee 1974, Gull 1975). However the primary shock seen in X-rays and radio at a radius of 150 arc seconds is not very bright and it is not clear that the reverse shock has been or is presently very strong. The Chandra image shows much fragmentation consistent with dense bullets and it is likely that significant heating arises, again, from the interaction of these bullets with the material pre-heated by the primary shock.

Acknowledgements. The results presented are based on observations obtained with *XMM-Newton*, an ESA science mission with instruments and contributions directly funded by ESA Member States and the USA. JV acknowledges support in the form of the NASA Chandra Postdoctoral Fellowship grant nr. PF0-10011, awarded by the Chandra X-ray Center.

References

- Anders, E., Grevese, N., 1989, *Geochimica et Cosmochimica Acta*, 53, 197
- Anderson, M.C., Rudnick, L. 1995, *Ap.J.* 441, 307
- Anderson, M.C., Keohane J.W., Rudnick, L. 1995, *Ap.J.* 441, 300
- Aschenbach B., Egger, R. & Trümper, J. 1995, *Nature* 373, 587
- Ashworth, W.B. 1980, *J. Hist. Astr.*, 11, 1
- Bell, A.R. 1977, *Mon.Not.R.astr.Soc* 179, 573
- Bleeker, J.A.M., Willingale, R., van der Heyden, K.J., et al. 2001, *A&A*, 365, L225,
- Braun, R., Gull, S.F., & Perley, R.A. 1987, *Nature*, 327, 395
- Chevalier, E., Kirshner, R.P. 1979, *Ap.J.* 233, 154
- Coleman, C.S., & Bicknell, G.V. 1985, *Mon.Not.R.astr.Soc* 214, 337
- Fesen, R.A., Becker, R.H., Blair, W.P. 1987, *Ap.J.* 313, 378
- Fesen, R.A., Becker, R.H. & Goodrich, R.W. 1988, *Ap.J.* 329, L89
- Gotthelf, E.V., Koralesky, B., Rudnick, L., Jones, T.W., Hwang, U. and Petre, R. 2001, *Ap.J.* 552, L39
- Gull S.F. 1975, *Mon.Not.R.astr.Soc* 171, 263
- Hamilton, A.J.S. 1985, *Ap.J.*, 291, 523
- Holt, S.S., Gotthelf, E.V., Tsunemi, H., Negoro, H. 1994, *PASJ* 46, L15

-
- Höflich, P., khokhlov, A. and Wang, L. 2001, astro-ph/0104025
- Hughes, J.P., Rakowski, C.E., Burrows, D.N. and Slane, P.O. 2000, Ap.J. 528, L109
- Kaastra, J.S., Mewe, R., Nieuwenhuijzen, H. 1996, in UV and X-ray Spectroscopy of Astrophysical and Laboratory Plasmas, p. 411, eds. K. Yamashita and T. Watanabe, Tokyo, Univ. Ac. Press
- Keohane, J.W., Rudnick, L., & Anderson, M.C. 1996, Ap.J. 466, 309
- Khokhlov, A.M., Höflich, P.A., Oran, E.S., Wheeler J.C., Wang, L. and Chtchelkanova, A.Yu. 1999, Ap.J. 524, L107
- Lawrence, S.S., MacAlpine, G.M., et al. 1995, A.J. 109, 2635
- Markert, T.H., Canizares, C.R., Clark, G.W., Winkler, P.F. 1983, Ap.J. 268, 13
- McKee C.F. 1974, Ap.J. 188, 335
- Mewe, R., Kaastra, J.S., Liedahl, D.A. 1995, Legacy 6, 16
- Reed, J.E., Hester, J.J., Fabian, A.C., Winkler, P.F. 1995, Ap.J. 440, 706
- Solinger, A., Rappaport, S. and Buff, J. 1975, Ap.J. 201, 386
- Truelove, J.K. & McKee, C.F. 1999, Ap.J.Supp.Ser. 120, 299
- van den Bergh, S., Kamper, K.W. 1983, Ap.J. 268, 129
- Vink, J., Kaastra, J.S., & Bleeker, J.A.M. 1996, A&A, 307, L41
- Vink J. et al. 1999, A&A 344, 289
- Woosley, S.E. & Weaver, T.A. 1995, Ap.J.Supp.Series, 101, 181

Chapter 5

Detection of X-ray line emission from the shell of SNR B 0540–69.3 with *XMM-Newton* RGS

K.J. van der Heyden, F. Paerels, J. Cottam, J. S. Kaastra, G. Branduardi-Raymont
Published in *Astronomy & Astrophysics* 365, L254 (2001)

Abstract

We present X-ray observations of PSR B 0540–69.3 with the *XMM-Newton* observatory. The spectra obtained with the Reflection Grating Spectrometer reveal, for the first time, emission from ionized species of O, Ne and Fe originating from the SNR shell. Analysis of the emission line spectrum allows us to derive estimates of the temperature, ionization timescale, abundances, location, and velocity of the emitting gas.

5.1 Introduction

SNR B 0540–69.3 is one of only a few Crab-like supernova remnants (SNRs) with a shell. SNR B 0540–69.3 harbors a pulsar, PSR B 0540–69.3, discovered in the soft X-ray band by Seward et al. (1984). Like the Crab, it shows plerion emission from a synchrotron nebula powered by the embedded young pulsar (Chanan et al. 1984). From the period (50 ms) and spin down rate ($4.79 \times 10^{-13} \text{ s}^{-1}$) a characteristic age of

1660 yr and rotational energy loss rate of 1.5×10^{38} ergs s^{-1} have been derived (Seward et al. 1984).

Early optical observations (Mathewson et al. 1980) classified SNR B 0540–69.3 as a young oxygen-rich SNR with an $8''$ diameter shell, bright in [O III]. Mathewson et al. (1980) also found a diffuse patch of [O III] $\sim 30''$ to the west of the ring which indicated that the remnant was larger than $8''$. A *ROSAT* High Resolution Imager observation by Seward & Harnden (1994) also revealed emission from well outside the central region, which they interpreted as from a patchy outer shell with a diameter of $55''$. This shell contributes $\sim 20\%$ to the measured flux in the *ROSAT* 0.1–2 keV band. More recently Gotthelf & Wang (2000) presented a high resolution *Chandra* HRC observation of PSR B 0540–69.3 which clearly shows emission from the outer shell.

In this letter, we report the results of observations of SNR B 0540–69.3 acquired with the Reflection Grating Spectrometer on board the *XMM-Newton* Observatory (den Herder et al. 2001). These observations allow us for the first time to detect and identify emission lines from the remnant shell. Our spectral analysis allows us to derive values for the temperature, ionization timescale, abundances, location, and velocity of the emitting gas.

5.2 Observations & Data Reduction

PSR B0540 was observed repeatedly as part of the calibration of the Reflection Grating Spectrometer (*RGS*) during the Calibration/Performance Verification (Cal/PV) phase. For the purpose of this letter, we have analyzed the 126 ks data obtained on 2000 May 26, which is the longest observation with the lowest background. The observation was performed with the telescope rolled such that the *RGS* dispersion axis was aligned at 21.29° , clockwise on the sky, from celestial north. The data were initially processed with the *XMM-Newton* Science Analysis Software (SAS). The spectra were extracted by applying spatial filters to the CCD image while a CCD pulse-height filter was applied to select the $m = -1$ spectral order. The remnant is located on the edge of a broad region of diffuse emission (Wang & Helfand 1991) which complicates background determination. However, the image is small enough on the detector that spatial regions offset from the source position can be used for background subtraction. The background spectra were extracted by applying the same pulse height filters as used for the source, to spatial regions at either edge of the camera.

A response matrix appropriate to the spatial extent of the source was generated as follows. A spatial mask corresponding to the *RGS* aperture was imposed on the *Chandra* HRC image, and the intensity distribution was integrated over the *RGS* cross-dispersion direction. The resulting profile was convolved with the *RGS* point source response matrix, generated with the SAS task RGSRMFGEN. The spectral analysis was performed using the SRON SPEX (Kaastra et al. 1996) package, which contains

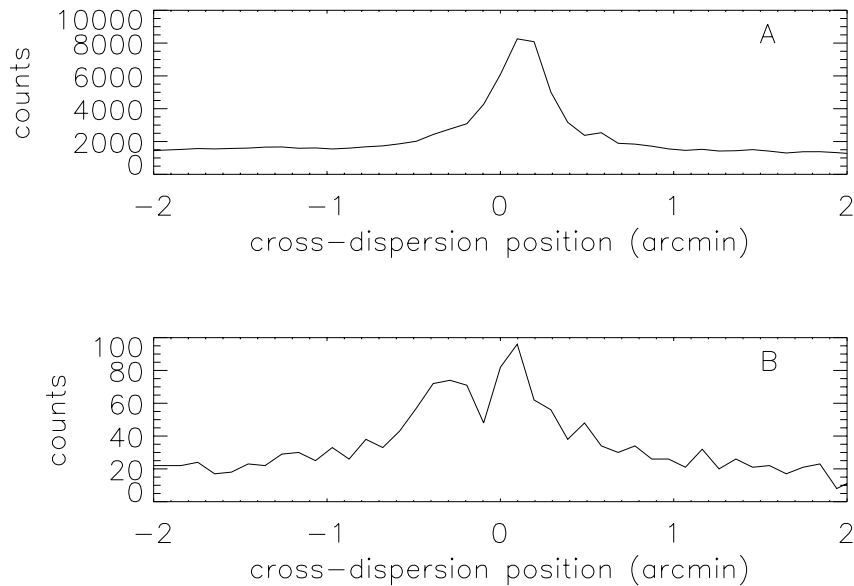


Figure 5.1: Cross-dispersion profiles of SNR B 0540–69.3 obtained by integrating along the dispersion axis for a: the entire spectrum and b: O VIII Ly α only.

the MEKAL code (Mewe et al. 1995) for modeling thermal emission.

5.3 Analysis and Results

5.3.1 Location of emitting region

We initially extracted spectra with spatial filters $0.25'$, $0.5'$, $1'$ and $1.5'$ wide, each centered about the peak emission. The most interesting feature in the spectra is the presence of an O VIII Ly α emission line that becomes more prominent as the width of the spatial extraction region is increased. This is an indication that at least some of the O emission is from the SNR shell, and not the central region. To further constrain the spatial distribution of the emitting gas we created a cross-dispersion image profile of the O VIII Ly α line by integrating over the line in the dispersion direction. The cross-dispersion profile, plotted in Fig. 5.1, shows two peaks. Referring to the *Chandra* HRC

image (Gotthelf & Wang 2000, reproduced here as Fig. 5.2), we conclude that we see O emission both from the central region of the remnant, centered on the pulsar, (the peak at offset zero in Fig. 5.1b), as well as from the partial shell to the west (the second peak ≈ 24 arcsec towards more negative offset in Fig. 5.1b).

The angular extent of this partial shell, $\Delta\phi \approx 30''$, corresponds to an effective wavelength width along the dispersion direction of ≈ 0.06 Å, comparable to the wavelength resolution of the spectrometer. This implies that we do not have the sensitivity to resolve variations in brightness along the shell.

5.3.2 Spectral analysis

We divided the remnant into three regions, Northeast (NE), Central (C) and Southwest (SW), for the purpose of spectral analysis. For the NE and SW regions we use an extraction width of $0.5'$ centered at $\pm 0.375'$ about the central compact region, while for the brighter C region we use a width of $0.25'$. The spectra for these regions are displayed in Figs. 5.3 and 5.4. Each spectrum shows a strong power law continuum with superimposed line emission, most notably O VIII Ly α . Emission line features are weakest in the spectrum extracted from the NE region, where we only detect O VIII Ly α and possibly weak O VII emission. The line emission is strongest in the SW spectrum where we easily identify emission lines of O VIII (Ly α , Ly β), O VII ($n = 2 - 1$ triplet, He β), Fe XVII (15.01, 16.78, 17.05, 17.10 Å), Ne X (Ly α), and Ne IX ($n = 2 - 1$ triplet). Due to galactic absorption, no features can be seen longward of ~ 23 Å. Note that even though the shell-like structure and the plerion are only partially resolved by the telescopes of *XMM-Newton*, the high spectral resolution of the *RGS* allows for high sensitivity to the discrete emission from the remnant, even though the spectrum is dominated by the powerlaw continuum from the plerion.

In the SW spectrum, O VIII Ly α has a significant offset of $\Delta\lambda = -0.17$ Å with respect to the laboratory wavelength. This offset must be largely due to a Doppler shift, and not to a positional offset between the nominal pointing direction (the pulsar position) and the emission centroid of the shell, because the equivalent wavelength extent of the shell is much smaller than the observed shift. In the *Chandra* image, we find that the centroid of the SW emission, projected onto the *RGS* dispersion direction, is offset from the centroid of the plerionic emission, by about $\approx -9''$ along the dispersion direction. This corresponds to a wavelength offset of -0.019 Å. The net Doppler shift of the SW emission is thus -0.15 Å, which corresponds to a radial velocity of $v \approx -2370$ km s $^{-1}$. A similar radial velocity is also observed in the other strong emission lines in the spectrum. Note that the radial velocity of the LMC, $v_{\text{LMC}} = +278$ km s $^{-1}$, is only a relatively small correction to this measurement. The emission lines seen in the C and NE spectra are too faint to permit a meaningful radial velocity determination.

We synthesized a spectral model comprising three components: a power law to represent the synchrotron emission from the plerion, a non-equilibrium ionization (NEI)

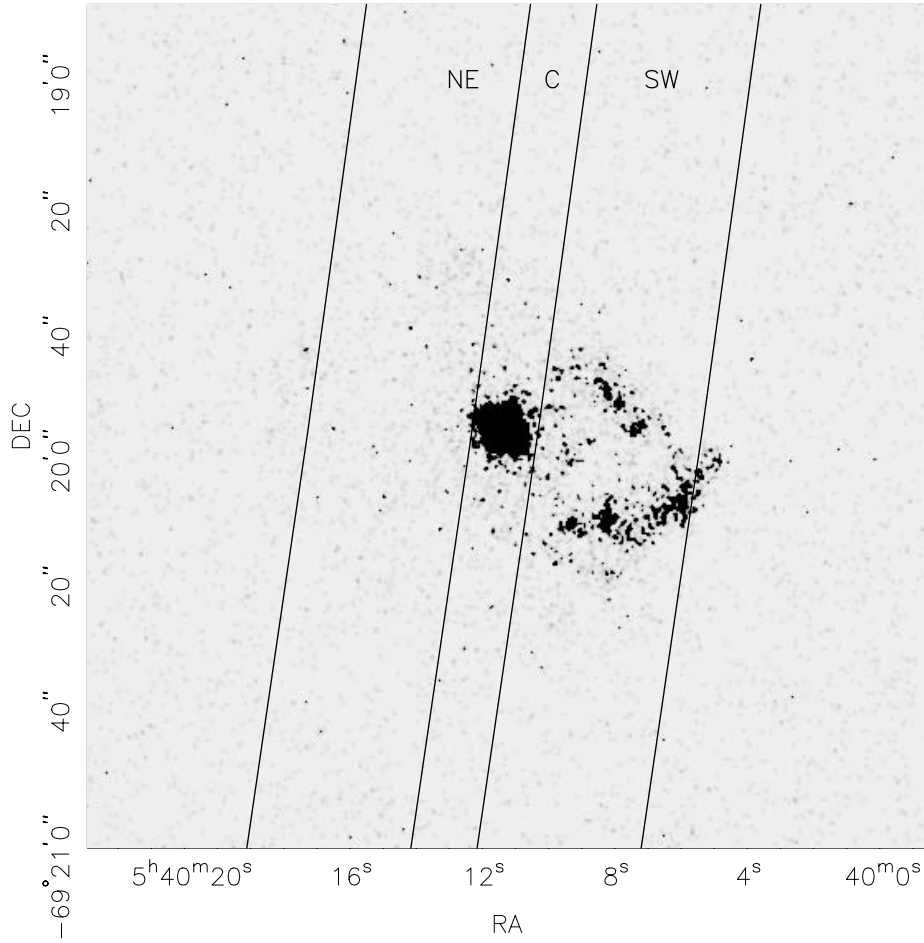


Figure 5.2: X-ray image of SNR B 0540–69.3 obtained by the *Chandra* HRC. The image contains the 50 ms pulsar PSR B 0540–69.3, the plerion and the outer shell. The SW, C and NE regions used for spectral analysis are indicated. The dispersion direction of the *RGS* is along the long dimension of the extraction regions.

model for the thermal line emission, and foreground absorption. The free parameters of the model are the photon index of the power law and its normalization, the electron

temperature T_e , emission measure, abundances, ionization age $n_e t$ of the shocked gas, and the column density N_H of foreground absorbing gas. Here, n_e is the electron density of the shell, and t is the time since the hot gas was shocked. We adopt a distance of 51 kpc throughout.

We concentrated our quantitative analysis on the SW region since the spectrum from this region contains the strongest line emission features. Fixing the O abundance to a third solar (note that we have no independent way of constraining the absolute abundances, since the continuum emission is dominated by the plerionic emission), the abundances of Ne and Fe were allowed to vary with respect to O. An initial fit was made to the SW spectrum, using O VIII Ly α and O VII-triplet only. The parameters obtained were subsequently used as starting parameters for fits to the entire spectrum. For the Ne/O and Fe/O abundance ratios, we obtain Ne/O \sim 3.0 and Fe/O \sim 2.1 relative to their solar values. The best fit model parameters are listed in Table 5.1. Fits were also made to the NE and C spectra. Since the line emission in these regions is extremely weak we fixed the NEI component parameters (i.e. electron temperature and ionization parameter) to the best fit parameters obtained from the SW region, while allowing the emission measure and photon indices of the power law component to vary. The best fit parameters are given in Table 1, and the spectra, together with the best fit models are shown in Figures 3, 4 and 5.

As can be seen from the Figures and the χ^2 values in Table 1, the fits are not perfect. This is probably due to a combination of remaining small calibration uncertainties in the *RGS* effective area (most of the χ^2 is in the relatively poor fit to the continuum, which is due to the plerion, at the shorter wavelengths, where the *RGS* effective area is least well calibrated), and the simplicity of our spectral model, which does not allow for temperature and ionization inhomogeneities. In particular, there is a feature at \approx 14 Å, which is not fit by our isothermal model. Candidate emission lines are $2p - 3d$ in Fe XVIII at 14.208 Å, or possibly $2s - 3p$ in Fe XXI at 14.008 Å, although the latter should be accompanied by strong emission at 12.29 Å in equilibrium. In any case, detectable amounts of higher charge states of Fe L would definitely indicate the presence of hotter plasma.

5.4 Discussion

First of all, a qualitative point. We detect faint, but significant O VIII emission from the direction of the plerion. At our spatial resolution, we cannot exclude the possibility that a significant component of this line emission is in fact from foreground remnant gas seen in projection and contamination by the SW region. If confirmed at higher spatial resolution, this detection would be interesting, because Mathewson et al. (1980) detected intense optical [O III] emission from this same inner region, with a large velocity dispersion of $v \approx$ 3000 km s $^{-1}$. There may consequently be a wide range of ionization present in the plerion. Unfortunately, we do not have the sensitivity to try

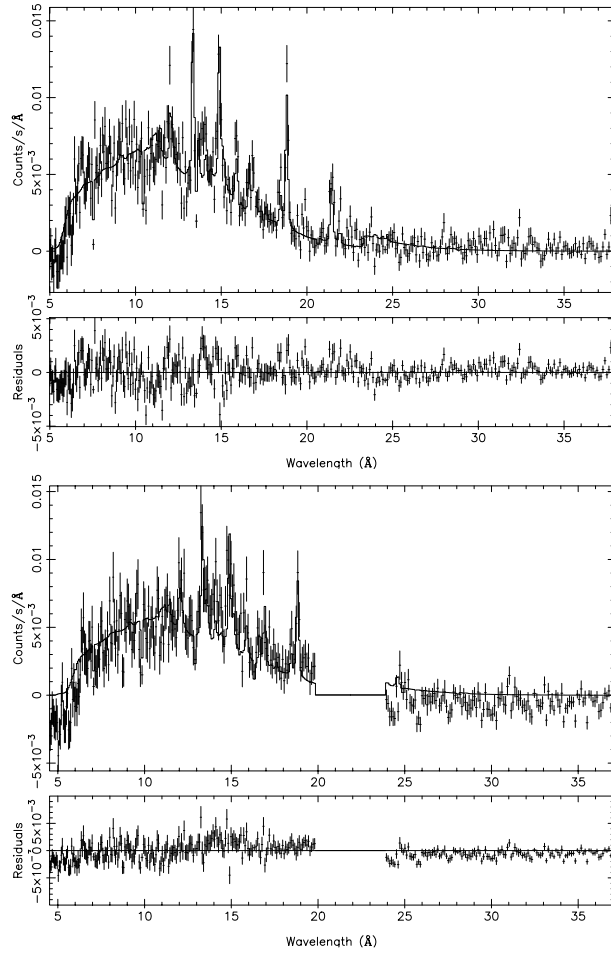


Figure 5.3: *RGS 1* & *RGS 2* (upper and lower plots respectively) spectrum of the SW region. The solid line is a model fit to the data. The gap between 20 to 24 Å in the *RGS 2* spectra is due to the failed CCD 4 on that instrument. The spectra exhibit a strong power law continuum due to synchrotron radiation from the plerion and thermal line emission from highly ionized atoms of O, Ne and Fe

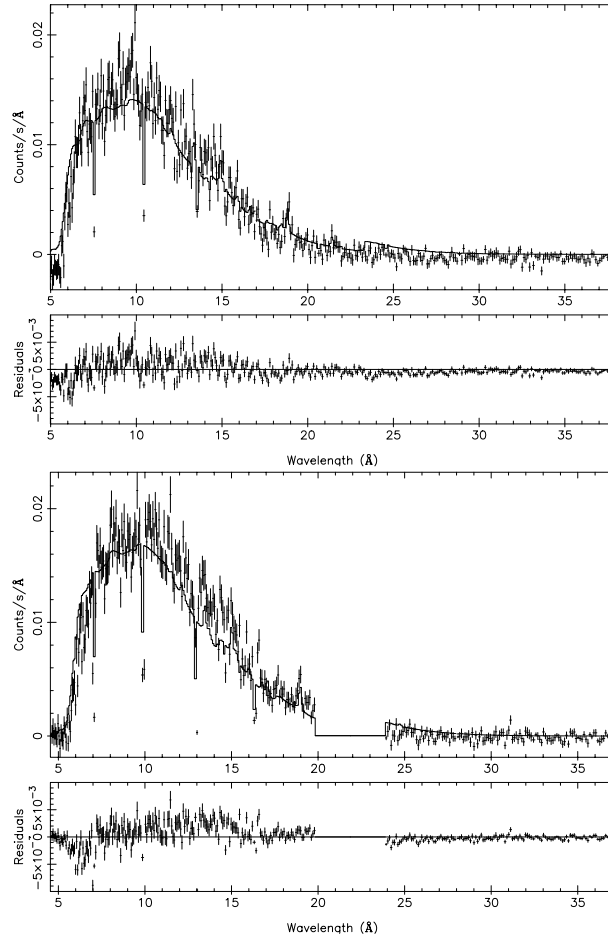


Figure 5.4: Same as for Figure 3, but for the C region.

and localize the highly ionized oxygen, and to constrain its kinematics for comparison with the [O III] image.

Next, we check for consistency of our measured parameter values. The interpretation of the radial velocity measured in O VIII is somewhat complicated. We see what appears to be a limb-brightened shell in the *Chandra* HRC image, but if the emission is really arranged in such a shell, one would not expect to see any radial velocity

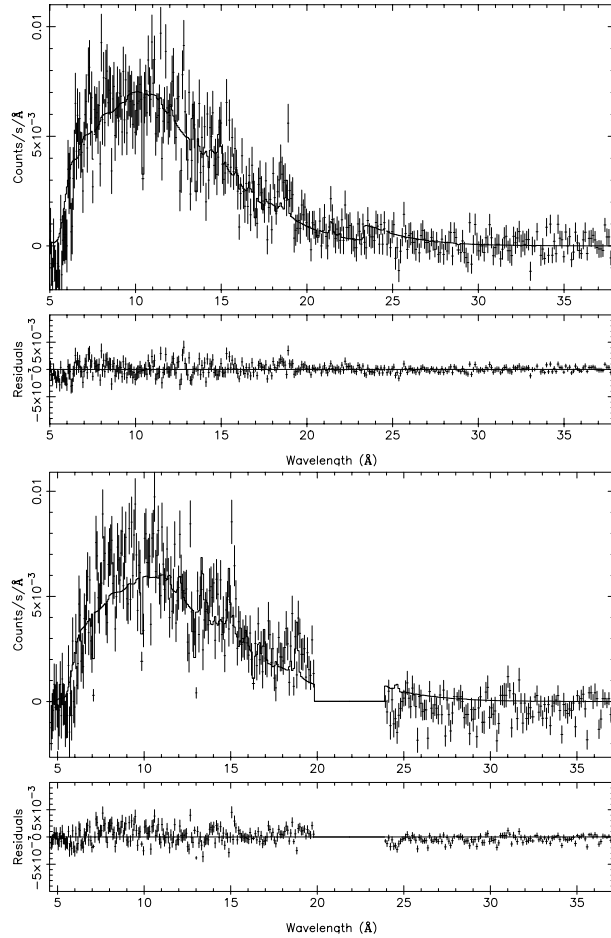


Figure 5.5: Same as for Figure 3, but for the NE region.

shift of the material at all, its velocity vector being entirely perpendicular to the line of sight. We know instead that the line emitting material has a velocity component along the line of sight of $\approx -2370 \text{ km s}^{-1}$, which, combined with an unknown perpendicular velocity component, sets a lower limit on the true space velocity of the O VIII emitting gas. To relate this space velocity to the velocity of the expanding blast wave requires making a further assumption about the structure and evolution of the

Table 5.1: Fitting results for the SW, C and NE regions of SNR B 0540–69.

parameter	SW	C	NE
NEI:			
$n_e n_H V$ (10^{58}cm^{-3})	92 ± 6.5	50 ± 20	45 ± 18
kT_e (keV)	0.58 ± 0.18		
$n_e t$ ($10^9 \text{cm}^{-3} \text{s}$)	25.22 ± 5		
POW:			
photon index	1.82 ± 0.1	1.2 ± 0.04	1.75 ± 0.1
ABS:			
N_H (10^{21}cm^2)	3.88 ± 1		
$\chi^2/\text{d.o.f.}$	2.04	2.8	2.9

expanding remnant. However, the measured radial velocity still gives a lower limit on the true expansion velocity, independent of these assumptions.

With a measured radius of $\approx 30''$, the shell has a linear radius of $R_s = 7.4$ pc. Combined with the lower limit on the expansion velocity, we estimate an upper limit to the age of the shell of $t < 2800$ yr, consistent with the pulsar spindown age of 1660 yr. Conversely, if we assume that the age of the shell is identical to the pulsar spindown age, we would conclude that the true expansion velocity of the blast wave is $\approx 4600 \text{ km s}^{-1}$, and the radial velocity we observe in the X-ray lines is either due to material well inside the interior of the remnant (where the flow velocities are smaller), or the line emitting gas must have a substantial perpendicular velocity component if it is located in the immediate post-shock region.

The discrete emission line spectrum implies an ionization age of approximately $n_e t \sim 2.5 \times 10^{10} \text{ cm}^{-3} \text{ s}$, a low value, which probably implies that the plasma has not yet reached ionization equilibrium. Combined with the pulsar spindown age, one infers a density of the medium of $n_e \sim 0.4 \text{ cm}^{-3}$. But the gas may have been shocked (much) more recently than the characteristic age of the blast wave, depending on its position within the remnant interior, and so we should regard this density estimate as a lower limit. Also, from the emission measure of the line emitting gas, we derive a density of approximately $n_e \sim 10 \text{ cm}^{-3}$ (assuming a half shell of relative thickness $\Delta R \sim R_s/10$ for the volume estimate). Given the relative insensitivity of the density estimate to the volume and emission measure, this higher density estimate may be closer to the characteristic values at the shell than the estimate derived from the ionization age, and this would favor the conclusion that the gas has been shocked more recently. In fact, the measured electron temperature, $kT_e \sim 0.6 \text{ keV}$, is incompatible with the

lower limit on the blast wave velocity $v_s > 2400 \text{ km s}^{-1}$ (unless the electron- and ion temperatures have not equilibrated), and most likely, we are seeing material that has recently passed through a (much slower) reverse shock. If gas with a much higher electron temperature is associated with the outer blast wave, it will be difficult to detect it in the *XMM-Newton* data. Because the remnant is only partially resolved, both the *RGS* and *EPIC* data are dominated by strong emission from the plerion, which reduces the sensitivity to detection of hot thermal gas.

5.5 Conclusions

We have detected resolved X-ray line emission from the supernova remnant shell around PSR B 0540–69.3, confirming the nature of the shell-like structure seen in previous experiments as a thermal SNR. Unfortunately, given the relatively low signal-to-noise of the observation, the fact that the object is only partially spatially resolved, and the uncertainties in the interpretation of the estimates of the various observable parameters, we can not uniquely decide what the evolutionary status of the remnant is, or what the relation of the line emitting gas is to the overall structure of the remnant.

Acknowledgements. We thank Eric Gotthelf for supplying us with his *Chandra* HRC image. The Laboratory for Space Research Utrecht is supported financially by NWO, the Netherlands Organization for Scientific Research. The Columbia group is supported by the U.S. National Aeronautics and Space Administration. The Mullard Space Science Laboratory acknowledges financial support from the UK Particle Physics and Astronomy Research Council.

References

- Chanan, G.A., Helfand, D.J., & Reynolds, S., 1984, *ApJ*, 287, L23
den Herder, J. W., Brinkman, A.C., Kahn, S.M. et al. 2001, *A&A*, 365 (this issue)
Gotthelf, E.V., & Wang, Q.D., 2000, *ApJ*, 532, L117
Kaastra, J.S., Mewe, R., Nieuwenhuijzen, H.1996, in *UV and X-ray Spectroscopy of Astrophysical and Laboratory Plasmas*, p. 411, eds. K. Yamashita and T. Watanabe, Tokyo, Univ. Ac. Press
Mathewson, D.S., Dopita, M.A., Tuohy, I.R., & Ford, V.L., 1980, *ApJ*, 242, L73
Mewe, R., Kaastra, J.S., Liedahl, D.A., 1995, *Legacy* 6, 16
Seward F.D., Harnden Jr F.R., & Helfand D.J., 1984, *ApJ*, 287, L19
Seward F.D. & Harnden Jr F.R., 1994, *ApJ*, 421, 581
Wang Q.D., & Helfand D.J., 1991, *ApJ*, 379, 327

Chapter 6

High-Resolution X-ray imaging and spectroscopy of N 103B

K.J. van der Heyden, E. Behar, J. Vink, A.P. Rasmussen, J.S. Kaastra
J.A.M. Bleeker, S.M. Kahn, R. Mewe

Published in *Astronomy & Astrophysics* 392, 955(2002)

Abstract

The X-ray emission from the young supernova remnant (SNR) N 103B is measured and analysed using the high-resolution cameras and spectrometers on board *XMM-Newton* and *Chandra*. The spectrum from the entire remnant is reproduced very well with three plasma components of $kT_e = 0.55$, 0.65 , and 3.5 keV, corresponding roughly to line emission by the O-K, Fe-L, and Fe-K species, respectively. Narrow band images reveal different morphologies for each component. The $kT_e = 0.65$ keV component, which dominates the emission measure ($4.5 \times 10^{65} \text{ m}^{-3}$), is in ionisation equilibrium. This provides a lower limit of 1200 yrs to the age of the remnant, which is in agreement with the previously assumed age of the remnant (1500 yrs). Based on the measured energy of the Fe-K feature at 6.5 keV, the hot (3.5 keV) component is found to be recently shocked (~ 200 yrs) and still ionising. The high elemental abundances of O and Ne and the low abundance of Fe could imply that N 103B originated from a type II supernova (SN) rather than a type Ia SN as previously thought.

6.1 Introduction

The young supernova remnant (SNR) N 103B (also known as SNR 0509-69) is the fourth brightest X-ray remnant in the Large Magellanic Cloud (LMC). It was first identified as a supernova remnant by Mathewson & Clarke (1983) based on the non-thermal nature of its radio spectrum and the relative emission-line strengths of S II and H α . Due to its small size (3 pc radius), Hughes et al. (1995) estimated the age of N 103B to be about 1500 yrs. Recent *Chandra* data (Lewis et al. 2001) show that the remnant is much brighter on the western limb than towards the East, this is most likely because of density contrasts between East and West. The radio and X-ray brightness variations are correlated on large scales, but do not overlap on finer spatial scales (Hughes 2001). In the analysis of the moderate resolution CCD ASCA spectrum of N 103B, Hughes et al. (1995) found strong emission lines from Si, S, Ar, Ca, and Fe, while no emission from O, Ne, or Mg was required in order to fit the ASCA spectrum. Hughes et al. (1995) thus concluded that N 103B is the result of a Type Ia supernova. In contrast, its proximity to the star cluster NGC 1850 and the H II region DEM 84 suggest that N 103B has an early-type progenitor (Chu & Kennicutt 1988).

In this work, we present the X-ray spectra of N 103B measured by the *XMM-Newton* suite of scientific instruments, i.e. the Reflection Grating Spectrometers (*RGS*) and the European Photon Imaging Cameras (*EPIC*). Particularly, we exploit the high dispersion of the *RGS* and its unique capability to resolve line emission from extended sources to investigate the nature of the hot plasma in N 103B in unprecedented detail and to shed new light on its progenitor. The large effective area of the *EPIC* cameras at high energies also allows us to study the important Fe-K emission. All these are complemented by the sharp images produced with the high angular resolution of the Advanced CCD Imaging Spectrometer (ACIS) on board *Chandra*, which reveal the temperature dependent morphology of N 103B.

6.2 Observation and Data Reduction

N 103B was observed by *XMM-Newton* on 7 August 2000. The effective exposure times and filters used on the different instruments are summarised in Table 6.1. The *RGS* data were processed using custom software that is identical in function to the RGS branch of the Science Analysis System (SAS), which was described briefly by Rasmussen et al. (2001). It includes pixel by pixel CCD event offset subtraction using median diagnostic frames, position dependent CTI correction, and correction of dispersion angles imparted by aspect drift.

We chose this analysis path since our response matrix generator features support for extended targets, and details in the angular distribution of N 103B were included in the response matrices. A single, broad-band archival ROSAT HRI image was used, along with mean spacecraft aspect and our spectral extraction angular width, to predict the monochromatic response in the readout channel space. This modeling

Table 6.1: *XMM-Newton* observation data of N 103B

Instrument	Filter	Exposure Time (ks)
MOS 1	Thick	8.0
MOS 1	Medium	8.0
MOS 2	Medium	23.5
PN	Medium	9.5
RGS 1		32.3
RGS 2		32.4

approach breaks down as soon as the target's morphology depends strongly on wavelength. However, it still permits accurate measurement of total line intensities and significant velocity distributions that distort line profiles in the *RGS*. In the case of N 103B, wavelength dependent variations in morphology (see Fig 6.4) appear on scales comparable to the *XMM-Newton* mirror point spread function (PSF), and our modelling approach remains reasonable for the purposes described. However, we do still expect to observe small (~ 20 mÅ) wavelength shifts for some lines due to variations in the remnant's morphology.

The raw *EPIC* data were initially processed with the *XMM-Newton* SAS. This involved the subtraction of hot, dead, or flickering pixels, as well as removal of events due to electronic noise. The spectrum was extracted from a circular region with a radius of $1.5'$. Background subtraction for *EPIC* was done using an exposure of the Lockman hole, with similar data selections and the same extraction region as for the SNR, scaling according to the exposure time. Periods of high particle background were rejected based upon the 10 – 12 keV count rate for the entire field of view.

In order to support our spectral analysis of the entire remnant with spatially resolved information on the morphology, we also used archival *Chandra* data of N 103B, which was observed with the back-illuminated ACIS-S3 chip on 4 December 1999 (see also Lewis et al. 2001). The cleaned event list was taken from the public *Chandra* archive. Narrow band images were extracted with energy selections made according to the nominal energy column, which provides a good energy estimate of each recorded photon.

6.3 Data Analysis

6.3.1 *XMM-Newton* Spectra

The *RGS* spectrum of N 103B is shown in Fig. 6.1. The spectrum is dominated by emission lines from highly ionised species of O, Ne, Mg, Si, & Fe. No emission longward

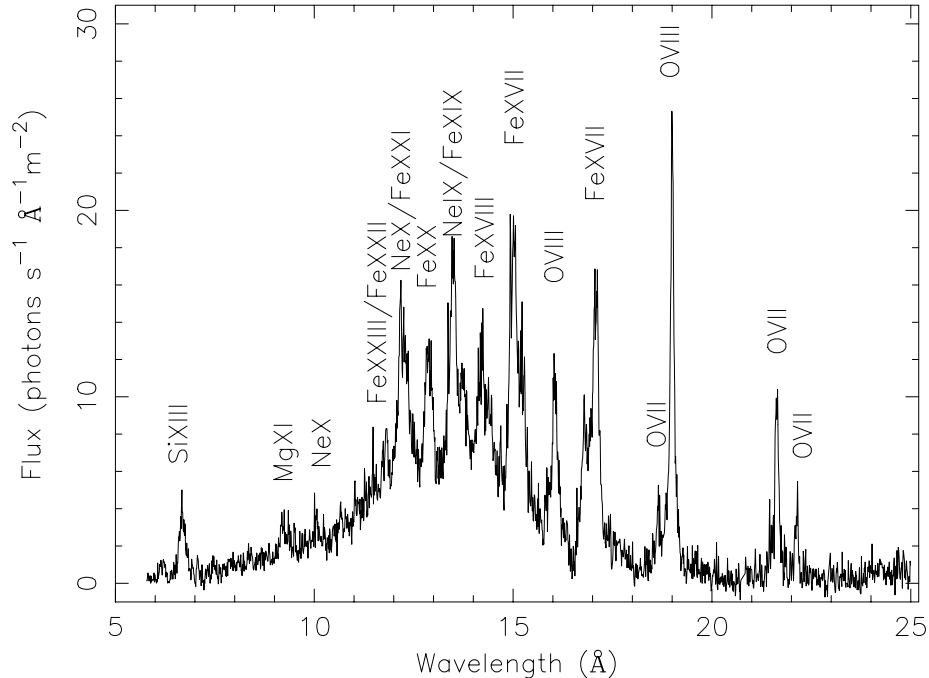


Figure 6.1: The fluxed *RGS* spectrum of N 103B. The most prominent lines are labeled.

of 23 Å is detected. This can probably be attributed to line-of-sight absorption towards the LMC rather than to the absence of N and C species, which could have been readily detected by the *RGS*. An important point to note is that we clearly detect O, Ne, and Mg lines. The OVII and OVIII lines are particularly strong. These features were not detected in the CCD spectrum of N 103B obtained with ASCA (Hughes et al 1995), and only weakly in a more recent CCD measurement with *Chandra* ACIS (Lewis et al. 2001). In order to observe shorter wavelengths than provided by the *RGS* we also employ the *EPIC-MOS* CCD spectrum, which is presented in Fig. 6.2. Emission lines from He-like S, Ar, Ca, as well as an Fe-K blend at 6.5 keV are clearly observed.

The spectral analysis was performed using the SRON SPEX package (Kaastra et al. 1996), which contains the MEKAL atomic database (Mewe et al. 1995) for thermal emission. Both Collisional Ionisation Equilibrium (CIE) and non-equilibrium ionisation (NEI) models are available in SPEX. Our model for the X-ray emission of N 103B consists of several plasma components. For each component, we fit for

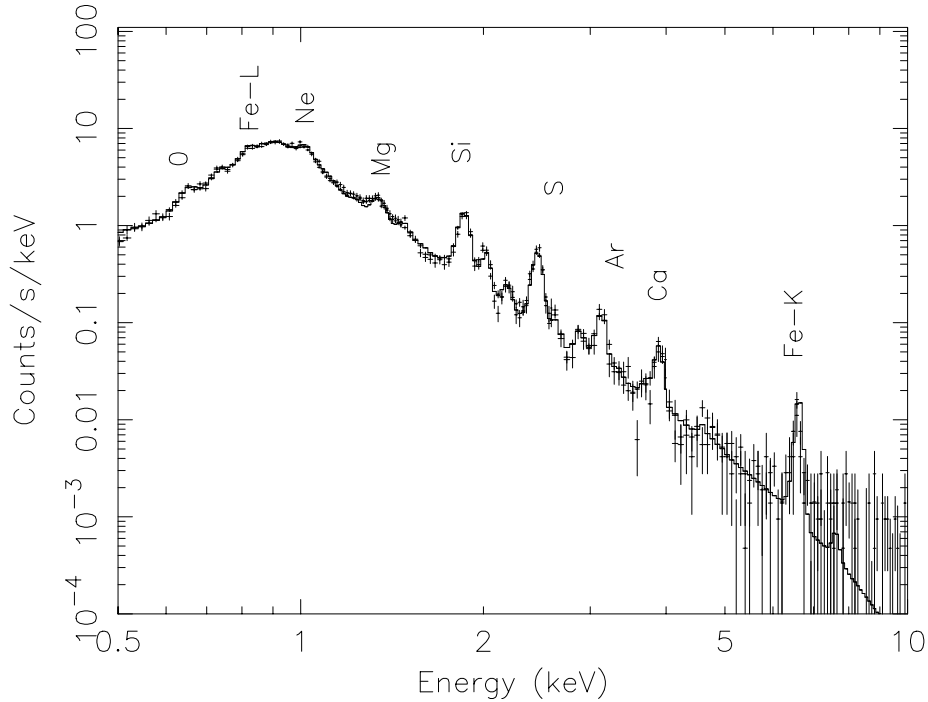


Figure 6.2: The N103B spectrum obtained with the *EPIC-MOS*. The solid line is the best-fit 3 component NEI model. The most prominent line blends are labeled.

the volume emission measure ($n_e n_H V$), the electron temperature (T_e), the elemental abundances, the redshift of the source, and the column density N_H of absorbing gas along the line of sight. In NEI models, the ionisation age ($n_e t$) (Kaastra & Jansen 1993) is also a free parameter. Here, n_e is the electron density, n_H is the hydrogen density, V is the volume of emitting gas and t is the time since the material has been shocked and heated to its current temperature. A distance of 51 kpc to the LMC is assumed (Feast et al. 2002).

In the following, we describe the procedure used to fit the total spectrum emitted by the whole remnant. The entire procedure was carried out for both CIE and NEI scenarios for comparison. We fitted the *RGS* spectrum first, since it has the most details and therefore is most constraining. Two plasma components are sufficient for obtaining a good fit to the *RGS* spectrum. Assuming that most of the X-ray emission is due to gas with more or less similar composition, we coupled the elemental abundances

in the two components. This also minimises the number of free variables in our fit, which makes it more robust.

It is clear from the *EPIC* spectrum that N 103B also has a hot component that is hard for the *RGS* to distinguish. In order to model this component, we fit the CCD spectrum of *EPIC* with three plasma components. We coupled the elemental abundances of O, Ne, Mg, Si, S, Ar & Ca of the third component to those of the two cooler components. The Fe abundance, however, is left free since we cannot fit the Fe-L and Fe-K with the same abundance value. The electron temperature, ionisation age and abundances of the two cooler components are fixed at the values obtained by the *RGS* fit. We note, however, that the hot component is not very sensitive to the other two components even when all three components are fitted simultaneously. In principle, the *EPIC* spectra could be fitted well with only two plasma components, i.e., without the relatively cold one. This explains why previous CCD observations did not detect the low-temperature component, which is dominated by O emission. It is only because of the spectral resolution of the *RGS* and its sensitivity to soft X-rays ($> 20 \text{ \AA}$) that we are able to resolve the O VII emission and hence need a cool or under-ionised component in the model. Finally, for consistency and in order to obtain the ultimate fit, we return to the *RGS* spectrum and refit it with three components. The hot component, which is constrained by the *EPIC*, but hardly produces line emission in the *RGS* spectrum is fixed at its *EPIC* values. The final parameters obtained for the three components are presented in Table 2 for both the CIE and NEI cases. We obtain a best-fit column density of $N_{\text{H}} = (2.5 \pm 0.7) \times 10^{25} \text{ m}^{-2}$. We also obtain a redshift of $340 \pm 70 \text{ km s}^{-1}$, which is consistent with the radial velocity of the LMC ($v_{\text{LMC}} = 278 \text{ km s}^{-1}$). The significance of NEI as well as the elemental abundances resulting from the fits are discussed in Sect. 4.

The best-fit spectral NEI model for N 103B is compared with the *EPIC-MOS* and *RGS* spectra in Figs. 6.2 and 6.3, respectively. The CIE model fits the data nearly as well. The overall fit to the data is very good. For the most part, the fit residuals are consistent within instrumental calibration uncertainties. However, some small discrepancies remain in the fit. The most prominent discrepancy is the missing flux in the model for the 2p-3s lines of Fe XVII at $\sim 17 \text{ \AA}$. This is a well known problem and has been observed in many coronal sources and in the laboratory. Therefore, it probably has nothing to do with NEI effects, although in principle NEI could enhance the 17 \AA lines with respect to the 15 \AA lines by means of inner-shell ionisation of Fe XVI. Doron & Behar (2002) suggest a model that could rectify the standard collisional-excitation line powers in MEKAL and in APEC (Smith et al. 2001). They show that including resonant excitation as well as recombination and ionisation processes (in CIE) from neighbouring ions in the models considerably enhances the 2p-3s lines and consequently produces the observed line ratios. Most of the other discrepancies in Fig. 6.3 have local asymmetrical profiles, which are a result of a combination of the following: (i) difference between the broadband spatial profile used in the response and the actual spatial profiles of individual emission lines, (ii) slight errors in model or

Table 6.2: Spectral fitting results. Components 1 & 2 reflect the *RGS* results. Component 3 is required to account for the Fe-K emission in the *EPIC* Data.

Parameter	Covered by	CIE	NEI
Component 1: $n_e n_H V$ (10^{64}m^{-3}) kT_e (keV) $n_e t$ ($10^{16} \text{m}^{-3} \text{s}$) redshift (kms^{-1})	<i>RGS</i>	6.2 ± 0.8 0.21 ± 0.05 340 ± 70	2.6 ± 0.1 $0.55^{+0.05}_{-0.32}$ $2.3^{+100}_{-0.3}$ 340 ± 70
Component 2: $n_e n_H V$ (10^{64}m^{-3}) kT_e (keV) $n_e t$ ($10^{16} \text{m}^{-3} \text{s}$) redshift (kms^{-1})	<i>RGS</i> + <i>EPIC</i>	65.1 ± 1.1 0.65 ± 0.05 340 ± 70	65.2 ± 1.2 0.65 ± 0.05 > 250 340 ± 70
Component 3: $n_e n_H V$ (10^{64}m^{-3}) kT_e (keV) $n_e t$ ($10^{16} \text{m}^{-3} \text{s}$) redshift (kms^{-1})	<i>EPIC</i>	4.1 ± 0.4 3.5 ± 0.5 4100 ± 300	4.1 ± 0.5 3.5 ± 0.5 5.3 ± 0.8 340 ± 70
$\chi^2/\text{d.o.f}$		1810/902	1790/899

data wavelengths, (iii) slight errors in the line spread function which does not account for the real asymmetrical profile of the RGS line shapes. The first of these sources of errors (i.e. the spatial profile used) should, however, dominate. There is also a slight overestimation of the continuum (in the range 18–23 Å) in the models, which is most likely due to uncertainties in the background subtraction. These inconsistencies between data and models are small and do not affect the conclusions drawn in this paper.

6.3.2 Chandra Images

In Fig. 6.4 we present three narrow-band images obtained with the ACIS camera. The images are produced in the energy ranges of 0.5–0.7, 0.7–1.0, and 3.0–6.8 keV. The first image (0.5–0.7 keV) is essentially an image of O-K emission (O VII and O VIII). The second image (0.7–1.0 keV) represents predominantly Fe-L emission and the third image (3–6.8 keV) reflects the morphology of Ar-K, Ca-K, and Fe-K lines, as well as some continuum. We have also separated this high-energy band into its various sub-component images (Ar, Ca, and Fe). However, within the statistics available for these images, all their morphologies appear to be fairly similar. The three images in Fig. 6.4 correspond roughly to the three plasma components described in Table 6.1,

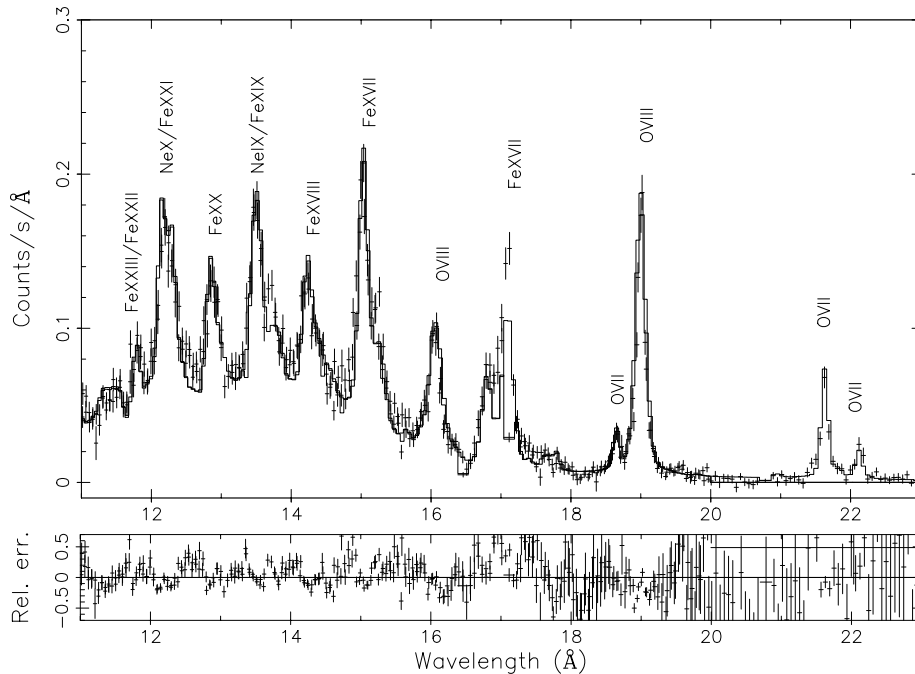


Figure 6.3: The *RGS* spectrum in the range 11–23 Å. The solid line represents a best-fit 2 component NEI model ($kT_e = 0.65$ & 0.55 keV) plus an underlying $kT_e = 3.5$ keV component as obtained from the *EPIC-MOS* fits. The missing flux in the model for the 2p–3s lines of Fe XVII at ~ 17 Å is a known problem which is due to missing transitions in the plasma code (see text).

in respective order. For short, we will henceforth refer to these three energy bands (and their respective plasma components) simply as the O-K, Fe-L, and Fe-K bands (components).

All three images in Fig. 6.4 show the same asymmetry, where the western hemisphere is much brighter than the eastern hemisphere. Aside from that, they are quite different in morphology. The O-K emission is concentrated in the northwest, while the Fe-L emission is more evenly distributed along the western rim of the remnant. The Fe-K image reveals a bright emission spot located at the southwestern rim. We also created a continuum subtracted, deconvolved, *XMM-Newton* Fe-K (i.e. 6.3–6.8 keV) image (see van der Heyden et al. 2002 for details). The *XMM-Newton* Fe-K image (Fig. 6.5) also shows a bright emission spot located at the southwestern rim, but ex-

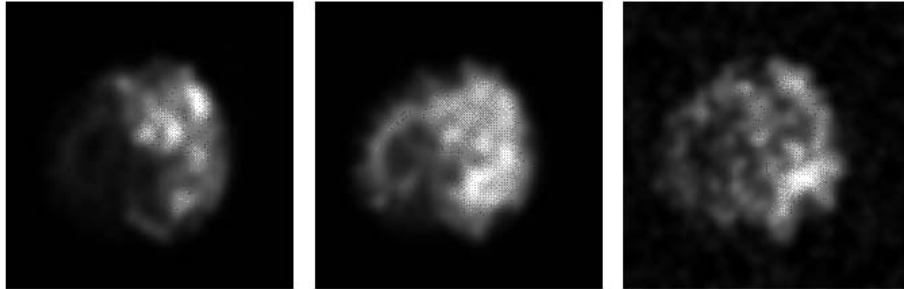


Figure 6.4: Chandra images for the approximate energy range 0.5–0.7 keV (left), 0.7–1.0 keV (centre) and 3–6.8 keV (right). These three energy bands are dominated by emission from O VII & O VIII (0.5–0.7 keV), Fe-L (0.7–1.0 keV) and Ar, Ca, Fe-K and continuum (3–6.8 keV).

tends further inward than seen in the *Chandra* 3–6.8 keV image. However, while the statistics of the *XMM-Newton* image is superior the ability to extract more information on the morphology of the remnant is hampered by the lower spatial resolution of the XMM cameras.

A more subtle difference between the emission in the three different bands is their radial distribution. In order to obtain a further insight into the radial distribution, we plotted the normalised radial profiles in counts per second in the three bands. These profiles in counts per pixel are presented in Fig. 6.6. Each profile is normalised separately to the average count rate measured in its energy range within a radius of $17.5''$. Despite the differences in azimuthal distribution, it can be seen that the (normalised) brightness of all three components is surprisingly similar; peaking at approximately $4''$, $7''$, and $10''$. The Fe-L component (solid curve) lies slightly ($0.5''$), but consistently inside the other two components. Normalising the radial profiles to their peak values does not alter this conclusion.

6.4 Discussion

6.4.1 Ionisation equilibrium

As demonstrated by the fitting results in Table 6.2, the *RGS* spectrum can be described similarly well by either a set of NEI or CIE plasma components, giving $\chi^2/\text{d.o.f.}$ of 1790/902 and 1810/899, respectively, for the two methods. Moreover, both models yield very similar spectra. In terms of emission measure, the X-ray spectrum of N 103B

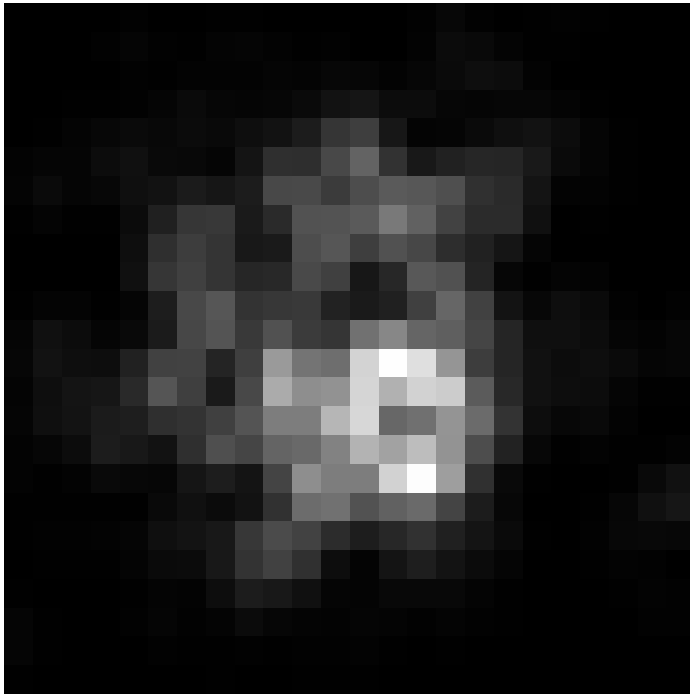


Figure 6.5: The deconvolved *XMM-Newton* Fe-K image. The Fe-K image reveals a bright emission spot towards the southwestern rim of the remnant.

is dominated by the Fe-L component (2). This emission component is represented by an electron temperature of $kT_e = 0.65$ keV in both models. The NEI model yields a very high ionisation age ($n_e t \geq 2.5 \times 10^{18} \text{ m}^{-3}\text{s}$) for this component, which is sufficiently high for the plasma to be in or very close to equilibrium (see Mewe 2002).

For the weaker and cooler O-K component (1), which produces the O VII and most of the O VIII emission, the two methods actually give very different temperature and emission measure values. In CIE conditions, these O ions form at a relatively low temperature (0.2 keV in the best-fit CIE model). In the case of NEI, on the other hand, this component is much hotter (0.55 keV), but still ionising ($n_e t \sim 2.3 \times 10^{16} \text{ m}^{-3} \text{ s}$). Both models reproduce the observed line intensities equally well. Note that the very large errors associated with the temperature (-0.32 keV) and ionisation time (+1e18 m^3s)

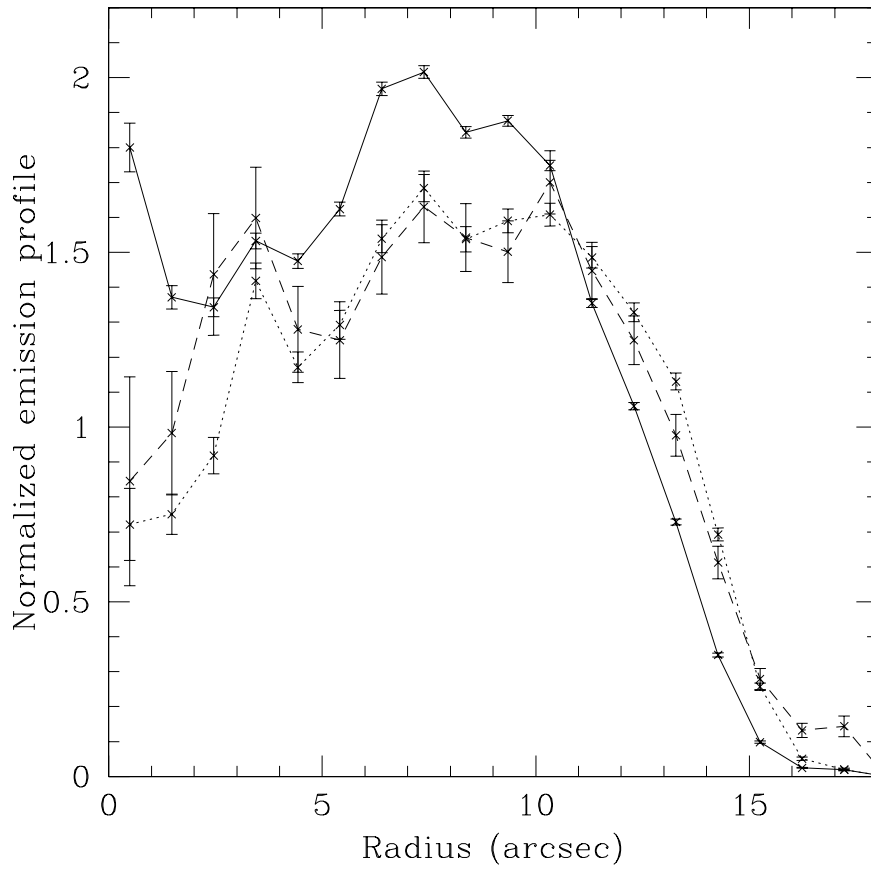


Figure 6.6: Normalised radial emission profiles for three separate photon-energy bands: 0.5–0.7 (dashed curve), 0.7–1.0 (solid curve), and 3–6.8 keV (dotted curve).

in the NEI model are due to the fact that the fitting routine finds another minimum at ~ 0.2 keV in the case of equilibrium ionisation, as expected. A comparison of the best-fit models for the O VII lines in both approaches is shown in Fig. 6.7. The differences between the NEI and CIE fits can be seen to be small, which implies that the

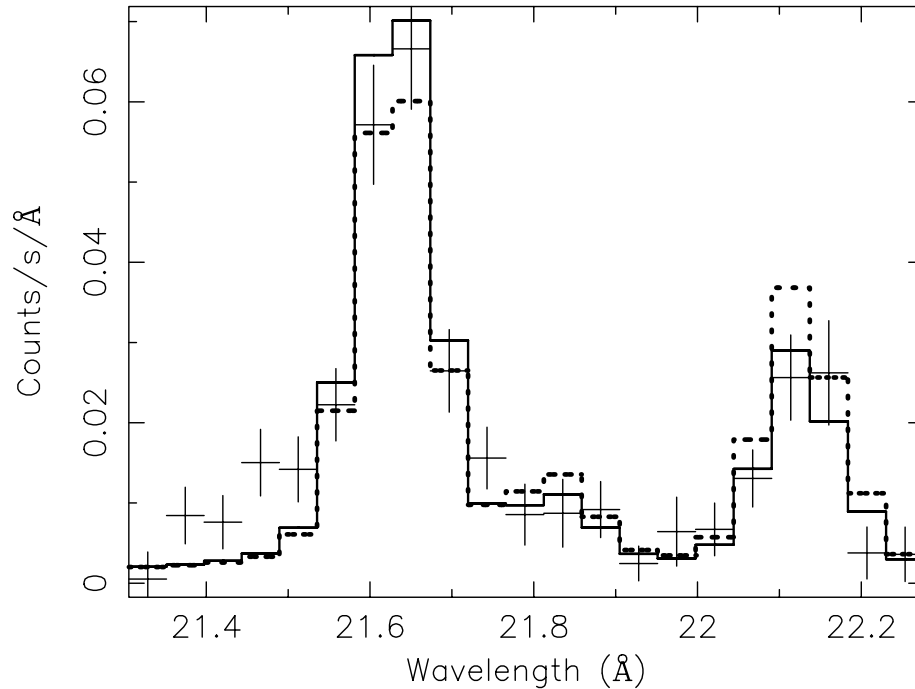


Figure 6.7: Comparison of NEI and CIE fits to the O VII Helium-like triplet. The crosses are the *RGS* data points in the 21.3–22.3 Å range. The solid line is the $kT_e = 0.55$ keV NEI model while the dashed line is the $kT_e = 0.2$ keV CIE model.

data do not decidedly favour one scenario over the other. This CIE/NEI ambiguity in the O VII lines was recognised before in the analysis of the *RGS* spectrum of the LMC remnant N132D (Behar et al. 2001). It should be noted that the ambiguity of NEI/CIE in the O-K component (1) does not affect the fits for the other components at all, i.e., we get the same parameters for components 2 and 3, regardless of whether component 1 is in NEI or CIE.

The most outstanding evidence for NEI conditions emerges from the hot Fe-K component (3), which is responsible for the Fe-K feature measured at 6.5 keV, as displayed in Fig. 6.8. An attempt to model this feature as a CIE He-like Fe line (see Fig. 6.9) requires that an extra doppler shift of ~ 4100 km s $^{-1}$, with respect to the LMC systemic velocity, be applied to this component. Such a large redshift is not observed for the Ar-K nor the Ca-K lines. This large doppler shift applied to the

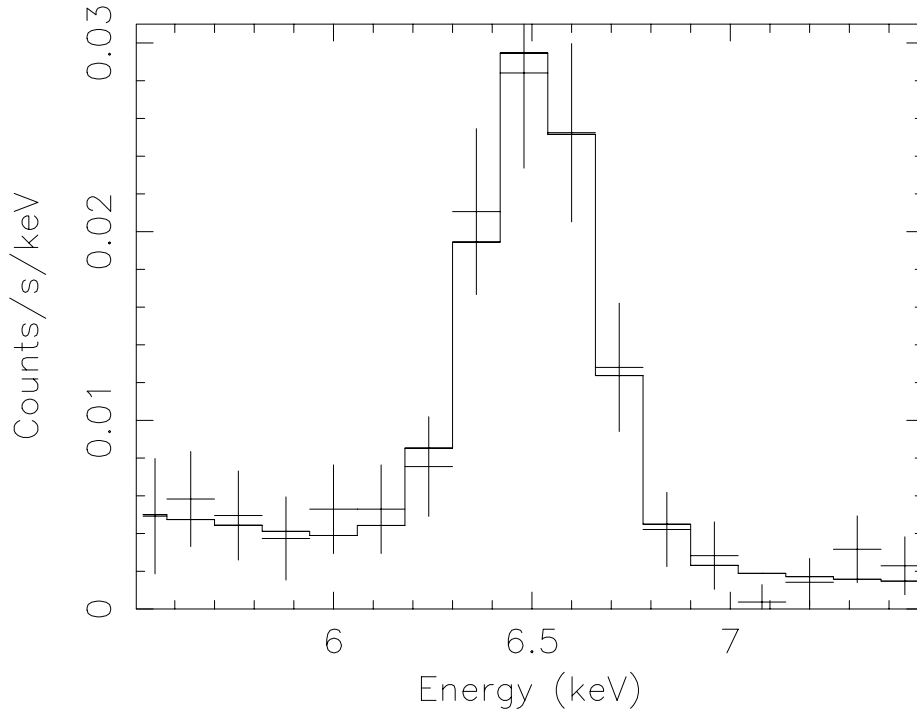


Figure 6.8: The *EPIC-pn* spectrum in the range 5.5-7.5 keV, showing the Fe-K emission. The solid line is a $kT_e = 3.5$ keV model fit. The location of the line centroid (~ 6.5 keV) indicates that the gas is not in ionisation equilibrium.

hot (3.5 keV) component now forces the cooler (0.65 keV) component to contribute most of the flux needed to fit the Ar-K and Ca-K lines. However, one would expect the Ar-K and Ca-K emission to arise from the same component as Fe-K. The Ar-K, Ca-K and Fe-K emission also seem to overlap spatially. This makes the large redshift interpretation unlikely. An alternative and more plausible explanation for the spectral position of the Fe-K complex would be a relatively low ionisation age of $n_e t \sim 5.3 \times 10^{16} \text{ m}^{-3} \text{ s}$ for the hot component, as obtained by our NEI fit (see Table 6.2) without any additional redshift. This NEI component predicts a distribution of Fe charge states that peaks between Fe XIX and Fe XXIV. This component also contributes most of the flux in the Ar and Ca lines and provides good fits to these lines.

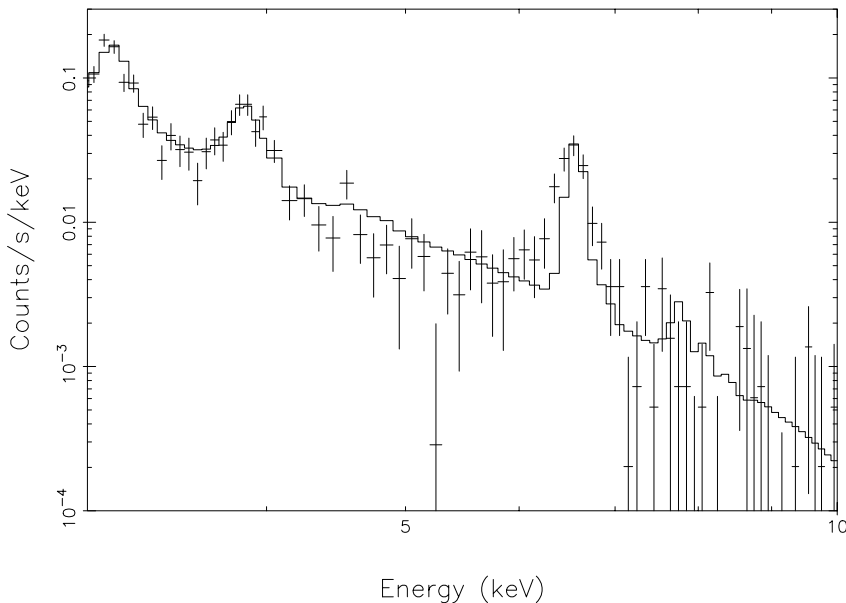


Figure 6.9: The *EPIC-pn* spectrum in the region from Ar-K to Fe-K. The solid line shows the best fit CIE model.

6.4.2 Density, age, and dynamics

The electron density can be calculated from the emission measure ($n_e n_H V$) if we know the volume of the emitting region. For simplicity, we generally assume the emitting volume to be a thick spherical shell. Based on the emission maps provided in Fig. 6.4 and on the radial profiles shown in Fig. 6.6, the shell is taken to have a radius of $R = 15''$ and to be $\Delta R = R/10 = 1.5''$ thick (Lozinskaya 1992). At a distance of 51 kpc, it gives a volume of $V = 1.7 \times 10^{51} \times f \text{ m}^3$, where f is a volume filling factor. This is a very crude estimate of the volume, but it is sufficient for our order-of-magnitude estimates that follow.

For the dominant Fe-L component (2), which seems to cover most of the western hemisphere (see Fig. 6.4), we assume a half filled shell or $f = 0.5$, which gives an electron density of $n_e \sim 25 \times 10^6 \text{ m}^{-3}$. Using this density and the ionisation age ($n_e t$) from Table 2, we get for the time since the Fe-L gas was shocked: $t \sim 3000 \text{ yrs}$. However, the spectral model changes slowly with ionisation age in the $(1-2.5) \times 10^{18} \text{ m}^{-3} \text{ s}$

$n_e t$ range. This would place a lower limit on the age estimate at ~ 1200 yrs, which is compatible with the previously assumed age of the remnant (1500 yrs).

Since the Fe-K component is concentrated in the southwestern region of the remnant (see Fig. 6.4), we estimate the filling factor to be $f = 0.25$. This gives an electron density of $\sim 8 \times 10^6 \text{ m}^{-3}$, which in turn yields an age of ~ 200 yrs. This is a relatively short time and is particularly in contrast with the derived age of the Fe-L component. For component 1, the bulk of the O-K emission is located towards the NW rim of the remnant. We again assume a filling factor of $f = 0.25$. This yields electron densities of 7.1×10^6 and $10.6 \times 10^6 \text{ m}^{-3}$ for the NEI and CIE models, respectively. If the NEI model is preferred, its ionisation time would then also imply a time of about 100 yrs since shock heating. Note the comparable ages of the O-K and Fe-K components. On the other hand, the different locations (Fig. 6.4) and vastly different temperatures of these two components strongly suggest that they may not be dynamically connected.

Indeed, each of the three spectral components can be identified spatially. As discussed earlier and as seen in Fig. 6.4, the various spectral components show substantial variation in morphology. Given our spectral analysis and due to the fact that roughly comparable densities are obtained for all of these components, it is most likely that these variations are due to gradients in temperature and ionisation ages. The different locations and temperatures of the three components suggest that they are probably unrelated dynamically. Despite these morphological differences the azimuthal average emission profiles show a remarkable similarity. Even more surprising is that, compared to the Fe-L component, the coolest (O VII/O VIII) and the hottest component peak at a larger radius, extend further out, and seem to be the most recently shocked components. This would suggest that these components are associated with material recently shocked by the blast wave, whereas the Fe L component may be plasma heated by the reverse shock. However, the overabundance of Ar, Ca and Fe-K suggests that, at least the hot component consists of ejecta material. Note that this confusing situation is corroborated by Lewis et al. (2002), who, based on imaging spectroscopy with Chandra, show that these elements have radially outward increasing abundance gradients. Both the abundance gradient and the radial emission profiles of the three components do not fit the standard description of young supernova remnants, in which there is an outer, hot, shocked ISM component, and a cooler shock ejecta component.

6.4.3 Elemental abundances and type of progenitor

As mentioned previously, N 103B was designated to be the result of a Type Ia SN on the basis of the lack of O, Ne, and Mg emission in the ASCA spectrum (Hughes et al. 1995). The *RGS* however, shows prominent O, Ne, and Mg emission, which strongly suggests that N 103B could in fact be the result of a core collapse SN. To investigate this further, we compare the abundance yields as obtained from fits to the *RGS* spectra to those predicted by theory for Type Ia and Type II nucleosynthesis models. We also compare these abundances to the average LMC values to verify that the observed X-

rays do not originate from shocked LMC ISM. All LMC abundance values are taken from Hughes et al. (1998) except for those of Ar and Ca, which are from Russell & Dopita (1992) as these values are not supplied by Hughes et al. (1998). We use the relative abundances because they are more consistent among the various models than the absolute abundances (see Hwang et al. 2000). The calculated abundances for the Type Ia models, the classical W7 and delayed detonation (WDD2) model, are taken from Nomoto et al. (1997), while the Type II models for 12 and 20 M_{\odot} zero-age main-sequence progenitors are taken from Woosley & Weaver (1995). The ratio comparisons are given in Table 6.3. The Fe-L abundance is derived from the $kT_e = 0.65$ keV component, while the Fe-K is from the $kT_e = 3.5$ keV component. All abundances are normalised to Si and relative to solar ratios (Anders & Grevese 1989).

Table 6.3: Element abundance ratios as derived from NEI fits to the data compared to the LMC abundances and theoretical yield for Type Ia and Type II (for 12 & 20 M_{\odot} progenitors) models. The ratios are all relative to solar (Anders & Grevesse 1989) and normalised to Si. The abundances for the Type Ia W7 and WDD2 models are from Nomoto et al. (1997), while the Type II yields are taken from Woosley & Weaver (1995). The LMC values are from Hughes et al. (1998), except for Ar and Ca which are from Russell & Dopita (1992).

Abun. ratio	Observed	Type Ia		Type II		LMC
		W7	WDD2	12 M_{\odot}	20 M_{\odot}	
O/Si	0.45±0.08	0.070	0.019	0.17	1.14	0.61
Ne/Si	0.37±0.07	0.005	0.001	0.13	1.08	0.93
Mg/Si	0.25±0.06	0.061	0.019	0.13	2.07	1.03
S/Si	1.91±0.21	1.074	1.167	1.63	0.5	1.16
Ar/Si	2.56±0.64	0.751	0.935	2.19	0.35	0.54
Ca/Si	2.91±0.87	0.891	1.382	1.75	0.42	0.34
FeL/Si	0.52±0.14	1.88	0.866	0.23	0.30	1.16
FeK/Si	1.24±0.44	1.88	0.866	0.23	0.30	1.16

Table 6.4: Estimated mass yields for O, Si and Fe. All values are in solar masses.

Element	Estimated mass	Type IA		Type II	
		W7	WDD2	12 M_{\odot}	20 M_{\odot}
O	0.27	0.14	0.07	0.22	1.48
Si	0.032	0.15	0.27	0.099	0.095
Fe	0.033	0.70	0.67	0.059	0.075

The derived abundance ratios measured for N 103B do not compare well with those

of the LMC. While some elements are underabundant by a factor of a few (Ne, Mg, Fe), others are grossly overabundant (S, Ar, Ca). The absolute abundances (not shown) are also larger than those of the LMC, indicating that the observed emission is by and large due to shocked ejecta. Furthermore, the measured abundance ratios compare much better with the type II models than with the type Ia models. Particularly, our abundance ratios for O/Si, Ne/Si, and Mg/Si are almost an order of magnitude larger than those predicted for a type Ia explosion, while the Fe/Si ratio is about a factor of 3 lower than predicted by the W7 model and slightly lower than predicted by the WDD2 model.

Next, we check if the total Fe and O masses are consistent with a Type Ia SN. According to our volume estimates for the Fe-L and Fe-K components (2 and 3) in the previous section, their emission comes from volumes of $V = 0.85$ and $1.2 \times 10^{51} \text{ m}^3$, respectively. Using these volumes along with the derived EM and Fe abundance, we calculate an Fe mass of $0.02 M_{\odot}$ (for $f = 0.5$) from Fe-L and $0.013 M_{\odot}$ from Fe-K, giving a total Fe mass of $0.033 M_{\odot}$. Similarly, we use the volume estimates made in Sect. 6.4.2, the emission measure and abundances of components 1 & 2 and 2 & 3 to calculate the total O and Si masses respectively. We obtain a total O mass of $0.27 M_{\odot}$ and Si mass of $0.032 M_{\odot}$. In Table 6.4 we compare the estimated O, Si and Fe masses to model predicted yields for type Ia and type II SNe. The estimated masses are not in exact agreement with any of the models, but compare better to the type II than type Ia models. In particular, the Fe mass estimate is only a factor 2-3 smaller than predicted by the core collapse models, while being more than an order of magnitude smaller than can be expected for a type Ia SN. The mass increases only with the square root of the filling factor (or by \sqrt{V}), so it is unlikely that our simple volume estimates could cause the order of magnitude discrepancy between our Fe mass estimate and that expected from the Type Ia models.

6.5 Summary & Conclusions

The high resolution *XMM-Newton* emission-line spectra of N 103B can be fitted well with three plasma components. The dominant component (Fe-L) is already in equilibrium and can be represented by a $kT_e = 0.65$ keV CIE model. The fact that 0.65 keV gas has equilibrated, together with its volume estimate, provides an approximate lower limit to the age of N 103B, which is found to be 1200 yrs. A separate component is needed to explain the O-K emission and here we find difficulty to distinguish between a relatively cool medium ($kT_e = 0.2$ keV) in equilibrium or hotter ($kT_e = 0.55$ keV) ionising gas. Both scenarios produce essentially the same spectrum for O VII. The Fe-K emission can be represented by a hot $kT_e = 3.5$ keV NEI component with a relatively low ionisation age of $n_e t \sim 5.3 \times 10^{16} \text{ m}^{-3} \text{ s}$, implying recent shock heating (~ 200 yrs). The description of the X-ray emission from N 103B in terms of this three-component model is strongly supported by the different morphologies revealed with the *Chandra*

images in three corresponding energy bands. The O-K component is concentrated in the northwest, the Fe-L component extends along the western rim of the remnant, and the hottest component (Fe-K) peaks at a bright knot in the southwest. The observed emission profiles, abundances, and ionization structure are not easily explained in terms of the standard description of young supernova remnants, in which there is an outer, hot, shocked ISM component, and a cooler ejecta component. Although the temperatures and the morphologies of the three components suggest that they are dynamically unrelated, the azimuthal average emission profiles of the hottest and coolest component show a remarkable similarity. These components peak at a larger radius and extend further out than the Fe-L component, and seem to be the most recently shocked components. This suggests that these components are associated with material recently shocked by the blast wave, whereas the Fe-L component may be plasma heated by the reverse shock. However, the overabundance of Ar, Ca and Fe-K suggests that, at least the, underionised, hot component consists of ejecta material (see Lewis et al. 2001). This somewhat confusing situation deserves future attention.

The *RGS* spectrum unambiguously reveals emission from species of O, Ne and Mg. The presence of these lines and the abundance measurements they provide suggest that N 103B might actually be the result of a type II SN and not a type Ia as previously thought. Also, the total O mass is higher than predicted by a type Ia SNe, while the total Fe mass is much lower than would be expected if N 103B was the result of a type Ia SN.

Acknowledgements. The results presented are based on observations obtained with XMM-Newton, an ESA science mission with instruments and contributions directly funded by ESA Member States and the USA. JV acknowledges support in the form of the NASA Chandra Postdoctoral Fellowship grant nr. PF0-10011, awarded by the Chandra X-ray Center. SRON is supported financially by NWO.

References

- Anders, E., & Grevese, N., 1989, *Geochimica et Cosmochimica Acta*, 53, 197
- Behar, E., Rasmussen, A.P., Griffiths, R.G., et al, 2001, *A&A*, 365, L241
- Bleeker, J.A.M., Willingale, R., van der Heyden, K.J., et al., 2001, *A&A*, 365, L225
- Chu, Y.-H., & Kennicutt, R.C., 1988, *AJ*, 96, 1874
- Doron, R., & Behar, E., 2002, *ApJ*, submitted
- Feast, M., Whitelock, P., & Menzies, J., 2002, *MNRAS*, 329, L7
- van der Heyden, K.J., Behar, E., Vink, J., et al., 2002, *New Visions of the X-ray Universe in the XMM-Newton and Chandra era*, in press
- Hughes, J.P., 2001, in *Young Supernova Remnants Eleventh Astrophysics Conference*, eds., S. S. Holt and U. Hwang, AIP Conference Proceedings, 565, 419

- Hughes, J.P., Hayashi, I., & Koyama, K., 1998, ApJ, 505, 732
- Hughes, J.P., Hayashi, I., Helfand, D.J., et al, 1995, ApJ, 444, L81
- Hwang, U., Petre, R., & Hughes, J.P., 2000, ApJ, 523, 970
- Kaastra, J.S., & Jansen, F.A., 1993, A&AS, 97, 873
- Kaastra, J.S., Mewe, R., & Nieuwenhuijzen, H.1996, in UV and X-ray Spectroscopy of Astrophysical and Laboratory Plasmas, p. 411, eds. K. Yamashita and T. Watanabe, Tokyo, Univ. Ac. Press
- Lewis, K.T., Burrows, D.N., Nousek, J.A., et al, 2001, in *Young Supernova Remnants Eleventh Astrophysics Conference*, eds., S. S.Holt and U. Hwang, AIP Conference Proceedings, 565, 181
- Lewis, K.T., Burrows, D.N., Hughes, J.P., et al., 2002, in *X-rays at Sharp Focus: Chandra Science Symposium*, in press
- Lozinskaya, T.A., 1992, *Supernovae and Stellar Wind in the Interstellar medium*, transl. from Russian by M. Damashek, AIP, New York
- Mathewson, D.S., Ford, V.L., Dopita, M.A., et al., 1983, ApJS, 51, 345
- Mewe, R., 2002, *New Visions of the X-ray Universe in the XMM-Newton and Chandra era*, in press
- Mewe, R., Kaastra, J.S., & Liedahl, D.A., 1995, Legacy 6, 16
- Nomoto, K., Hashimoto, M., Tsujimoto, T., et al, 1997, Nucl. Phys.A, 616, 79
- Rasmussen, A.P., Behar, E., Kahn, S.M., et al. 2001, A&A, 365, L231
- Russell, S.C., & Dopita, M.A., 1992, ApJ, 384, 508
- Smith, R. K., Brickhouse, N. S., Liedahl, D. A., & Raymond, J. C., 2001, ApJ, 556, L91
- Woosley, S.E., & Weaver, T.A., 1995, ApJS, 101, 181

Chapter 7

High resolution spectroscopy and emission line imaging of DEM L 71 with *XMM-Newton*

K.J. van der Heyden, J.A.M. Bleeker, J.S. Kaastra, J. Vink

Published in *Astronomy & Astrophysics* 406, 141 (2003)

Abstract

The X-ray emission from the supernova remnant DEM L 71 is measured and analysed using the high-resolution cameras and spectrometers on board *XMM-Newton*. The spectrum from the outer shell is reproduced very well by two plasma components of $kT_e = 0.3$ and 0.8 keV. The abundance value from this shell is consistent with the average LMC values. More extreme temperature variations are possibly indicated by spatial variations in the O VII forbidden/resonance line ratio, which could imply that in some regions the plasma is cooling dramatically and recombining. However, an alternative and equally interesting possibility is that the variation in forbidden/resonance ratios is due to resonant scattering, which would reduce resonance line emission along lines of sight with a high O VII column density. The inner region is hotter ($kT_e = 1.1$ keV) and shows enhanced Fe and Si abundances. We estimate the Fe and Si ejecta mass to be 0.7–1.1 M_\odot and 0.1–0.15 M_\odot , respectively. The morphology, mass estimates and abundances strongly suggest that DEM L 71 is the result of a type Ia explosion, as indicated by previous measurements.

7.1 Introduction

DEM L 71 (SNR 0505-67.9) belongs to a class of Supernova Remnants (SNR) that are dominated by hydrogen emission in their optical spectra with virtually no emission from collisionally excited forbidden lines. Analysis of the optical spectrum of DEM L 71 indicates a shock velocity of 300–800 km s⁻¹ which corresponds to a shock temperature of $T_s = 0.11 - 0.75$ keV (Smith et al. 1994). This information, combined with a radial size of ~ 10 pc, gives an estimated age of $\sim 10^4$ years. *ASCA* spectroscopy revealed that, despite its age, DEM L 71 still showed emission from ejecta material in the form of enhanced Fe abundance (Hughes et al. 1998). The enhanced Fe abundance indicates that DEM L 71 is the result of a type Ia SNe. The recent *Chandra* Fe-L images (Hughes et al. 2003; see also Fig. 7.1) also reveal that the remnant exhibits both shell-like X-ray emission and a centrally filled morphology in this energy range.

In this work, we present the X-ray spectra of DEM L 71 measured by the *XMM-Newton* suite of scientific instruments, i.e. the Reflection Grating Spectrometers (*RGS*) (den Herder et al. 2001) and the European Photon Imaging Cameras (*EPIC*) (Turner et al. 2001; Strüder et al. 2001). In particular, we exploit the high dispersion of the *RGS* and its unique capability to resolve line emission from extended sources to investigate the conditions of the X-ray emitting plasma in DEM L 71 in unprecedented detail.

7.2 Observation and Reduction

Our analysis is based on *XMM-Newton* observations of DEM L 71 obtained on 2 April 2001. The observation was performed with the telescope rolled such that the *RGS* dispersion axis was aligned at 72°, clockwise on the sky from celestial North. A large fraction of the observation is affected by high particle background caused by solar activity. For the *EPIC* instruments periods of high particle background were rejected based upon the 10–12 keV count rate for the entire field of view. After filtering out these high background periods we are left with a net exposure time of 10 ks for the *EPIC* instruments. The *EPIC* instruments were all operated in full window mode with the medium filter in place. Good time intervals (GTI) for the *RGS* were created based on the count rate in CCD number 9 (it is the one closest to the optical axis of the telescope, therefore the most affected by background flares). After applying the GTI filter we are left with an effective exposure time of 40 ks for the *RGS*. The spectra were extracted by applying spatial filters to the CCD image while a CCD pulse-height filter was applied to select the $m = -1$ spectral order. All the *XMM-Newton* data were processed using the Science Analysis System (SAS version 5.3).

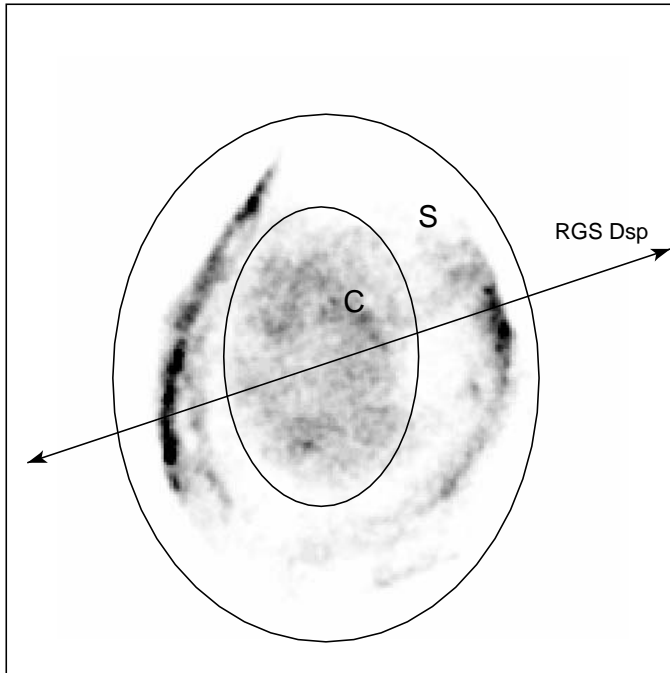


Figure 7.1: *Chandra* image for the approximate energy range 0.7–1.0 keV. The regions used for the extraction of the outer shell (S) and central region (C) are indicated. The alignment of the *RGS* dispersion axis is also indicated.

7.3 Analysis and Results

7.3.1 Spectra

The spectral analysis was performed using the SRON SPEX package (Kaastra et al. 1996), which contains the MEKAL atomic database (Mewe et al. 1995) for thermal emission. Our model for the X-ray emission of DEM L 71 consists of several plasma components. For each component, we fit for the volume emission measure ($n_e n_H V$), the electron temperature (T_e), the ionisation age ($n_e t$) (Kaastra & Jansen 1993), the

elemental abundances, the redshift of the source, and the column density N_{H} of absorbing gas along the line of sight. Here, n_e is the electron density, n_{H} is the hydrogen density, V is the volume of emitting gas and t is the time since the material has been shocked and heated to its current temperature. A distance of 52 kpc to the LMC is assumed (Feast et al. 2002).

The first order *RGS* spectrum of DEM L 71 is shown in Fig. 7.2. The spectrum is dominated by emission lines, the most prominent of which are from transitions of highly ionised ions of C, O, Fe and Ne. The O VIII- $L\alpha$ and O VII-triplet lines are particularly strong. Weaker, but unambiguous, emission from ions of N, Mg and Si are also present. While the second order *RGS* spectrum has higher spectral resolution, it does not provide any additional information. The second order spectrum is also of lower statistical quality and was therefore not used.

We fitted the *RGS* 1&2 spectra, extracted from the entire source, simultaneously. A response matrix appropriate to the spatial extent of the source was generated as follows. A spatial mask corresponding to the *RGS* aperture was imposed on the *Chandra* ACIS image, and the intensity distribution was integrated over the *RGS* cross-dispersion direction. The resulting profile was convolved with the *RGS* point source response matrix, generated with the SAS task RGSRMFGEN. We find that one plasma component does not describe the data sufficiently well and that at least two NEI plasma components are needed for obtaining a good fit to the *RGS* spectrum. A hotter component ($kT_e \sim 0.8$ keV) describes the spectrum below ~ 20 Å, while a cooler component ($kT_e \sim 0.2$ keV) is needed to model the emission from the O VII-triplet through C VI. When fitting the abundances we used O as the reference atom and, for technical reasons, kept its abundance fixed to solar. We use O because it has the strongest emission and would thus give the least uncertainty in the abundance determination. We allowed the abundance of H, C, N, Ne, Mg, Si and Fe to vary with respect to O. The He abundance was pegged to the H value. The best fit results, given in Table 7.1, gives a $\chi^2/d.o.f \sim 1869/945$. We obtain a best fit $N_{\text{H}} = (9.5 \pm 3.1) \times 10^{24}$ m $^{-2}$ and a systematic redshift of 380 ± 120 kms $^{-1}$, which is consistent with the LMC radial velocity (278 kms $^{-1}$). The derived elemental abundances are consistent with the average LMC abundance values. We discuss this more extensively in Sec. 7.4.2.

The model provides very good fits to the data, though a few discrepancies exist. For the most part, the fit discrepancies in Fig. 7.2 are a result of the difference between the broad band spatial profile used in the response and the actual spatial profiles of individual emission lines. The images in Fig. 7.4 show that the remnant's morphology depends strongly on wavelength.

In addition to the spectral features which are present in the *RGS* spectra, the *EPIC* spectra also show more prominent emission from Si and also S. We do not detect any significant Fe-K emission nor emission from Ca and Ar. We extracted and fitted the *EPIC-pn* spectrum from the entire source. We use the *EPIC-pn* spectra because they provide the best statistics. As a starting point we used the same model and parameters obtained from the *RGS* fits. We first allow only the normalisations of the

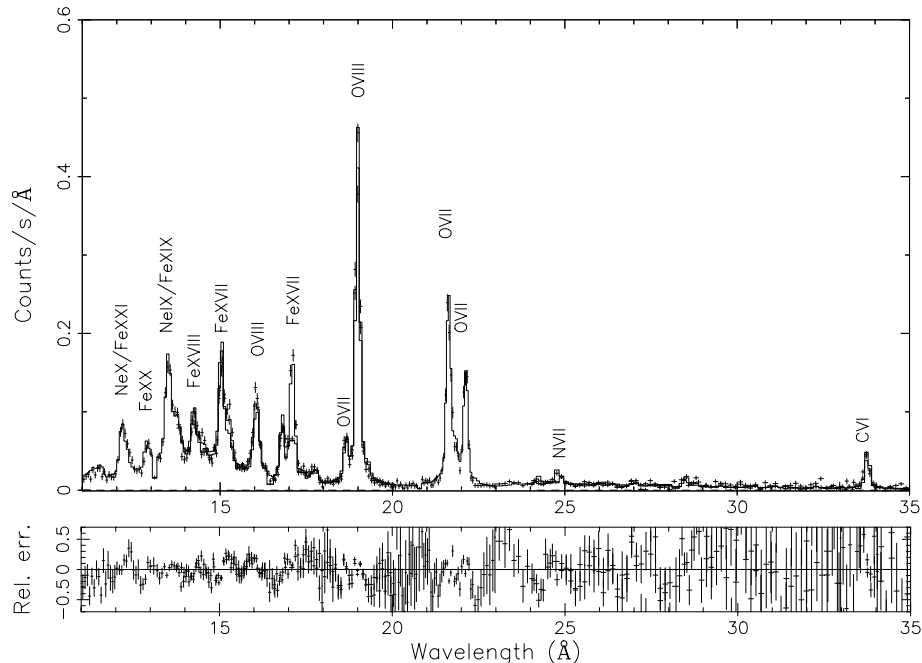


Figure 7.2: The first order *RGS* spectra of DEM L 71 in the range 11–35 Å. *RGS-1* and *RGS-2* spectra are overplotted. The solid line represents a best-fit 2 component NEI model ($kT_e = 0.2$ & 0.8 keV). The most prominent line blends are labeled.

plasma components to vary and subsequently we allowed the absorption, temperature, ionisation age and abundances to vary. The fit results are supplied in Table 7.1. The derived parameters, except the normalisations, from the fit to the *EPIC-pn* data remain similar to those obtained from the *RGS*. The larger normalisations for the *EPIC-pn* are due to the higher N_H and differences in the *RGS* and *EPIC-pn* calibrations (of the order 10%).

We also extracted and fitted the *EPIC-pn* spectra from both the outer and central region (see Figs. 7.1 & 7.3). The spectrum from the inner region is dominated by a broad emission peak around 0.9 keV from Fe-L. The spectrum from the outer rim is softer and shows more pronounced O-K (O VII and O VIII) and Mg-K α lines. We fitted the spectrum extracted from the rim first. We find that this spectrum can not be well described using only one plasma component. A model composed of two NEI plasma

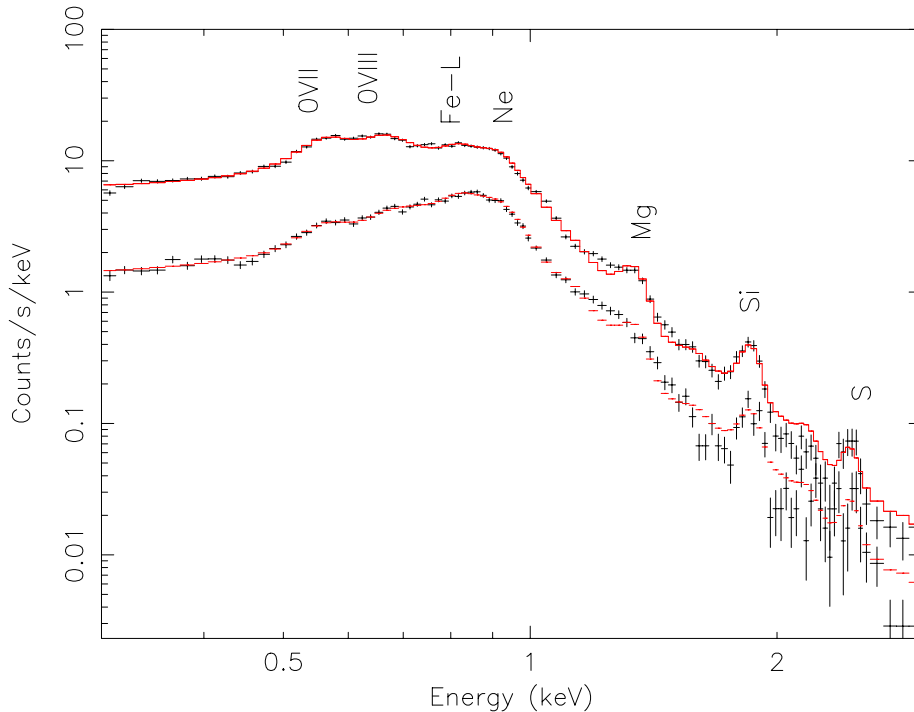


Figure 7.3: The DEM L 71 spectrum obtained with the *EPIC-pn*. The upper curve represents the spectrum from the shell, while the lower curve is from the central region. The solid line represents a best-fit NEI models. The most prominent line blends are labeled.

components provides a better fit to the data. The fitting procedure was the same as for the full *EPIC-pn* spectrum. We then fitted the spectrum from the inner region. As a model we used one NEI component to account for emission from the central shell-like structure. In addition to this, we added the same plasma components and parameters as derived from the fits to the outer region. Only the normalisations from these components were allowed to vary. We do this to account for any projected fore/background shell emission.

The results of the fits are supplied in Table 7.2. The shell components ($kT_e \sim 0.3\&0.8$ keV) have lower temperatures than the central component ($kT_e \sim 1.1$). Another significant difference between the two regions is the Fe/O & Si/O abundance ratio. The outer region has a Fe/O ~ 1.6 and Si/O ~ 1.5 , while the inner regions has

Table 7.1: Best fit parameters for fits to the *RGS* and *EPIC-pn* spectra, extracted from the entire remnant. The abundance values are all normalised and relative to solar (Anders & Grevesse 1989). Note that C and N emission can not be determined from the *EPIC-pn* data, while the S-K emission is too weak to be detected by the *RGS*.

Parametres	<i>RGS</i>		<i>EPIC-pn</i>	
	Comp. 1	Comp. 2	Comp. 1	Comp. 2
$n_e n_H V$ (10^{64} m^{-3})	16.78 ± 0.71	3.51 ± 0.70	30.10 ± 10.01	5.34 ± 3.03
kT_e (keV)	0.19 ± 0.02	$0.83^{+0.05}_{-0.20}$	0.21 ± 0.04	$0.82^{+0.40}_{-0.21}$
$n_e t$ ($10^{16} \text{ m}^{-3} \text{ s}$)	81.10 ± 20.10	7.31 ± 3.11	$81.01^{+80.10}_{-30.03}$	$7.20^{+10.10}_{-4.20}$
N_H (10^{24} m^{-2})	9.50 ± 3.10		12.10 ± 6.30	
Abundances (wrt solar):				
H/O	4.96 ± 1.11		5.0 ± 2.12	
C/O	2.3 ± 0.82		-	
N/O	0.35 ± 0.21		-	
Ne/O	1.50 ± 0.41		1.49 ± 1.02	
Mg/O	2.03 ± 1.01		2.11 ± 1.32	
Si/O	1.78 ± 1.12		1.96 ± 1.41	
S/O	-		2.01 ± 1.6	
Fe/O	2.65 ± 0.42		2.64 ± 1.41	

Table 7.2: *EPIC-pn* spectral fitting results for the shell and central region. The abundance values are all normalised and relative to solar (Anders & Grevesse 1989).

Parametres	Shell		Central region
	Comp. 1	Comp. 2	
$n_e n_H V$ (10^{64} m^{-3})	$6.11^{+2.04}_{-0.31}$	$4.52^{+1.10}_{-0.22}$	0.65 ± 0.22
kT_e (keV)	$0.36^{+0.12}_{-1.34}$	0.79 ± 0.05	$1.12^{+0.11}_{-0.33}$
$n_e t$ ($10^{16} \text{ m}^{-3} \text{ s}$)	$4.7^{+30.1}_{-0.5}$	11.1 ± 0.22	4.1 ± 0.8
Abundances (wrt solar):			
Si/O	1.53 ± 0.22		2.32 ± 0.91
Fe/O	1.61 ± 0.34		5.94 ± 2.10

a much higher Fe/O ~ 5.9 and Si/O ~ 2.3 . The interpretation is discussed in Sec. 4.3.

Some systematic fit residuals are present in the *EPIC-pn* fits. The most prominent residual is the underestimation of the spectra at ≈ 1.2 keV. This is a known problem

and is probably due to missing high excitation lines of Fe XVII-XIX in the plasma code (see Brickhouse et al.2000).

7.3.2 Monochromatic images and single ion spectroscopy

We extracted monochromatic images for various lines to probe variations in temperature and ionisation ages over the remnant and to further investigate the morphological differences between O and Fe emission. In order to compare *RGS* line images to one another one has to take into account an important systematic effect, which is the chromatic magnification that makes long wavelength images more 'squashed' than the shorter wavelength images. We correct for this effect, to first order, by using the grating equations. The extent of the source of the source produces a maximum broadening of $\pm 0.08 \text{ \AA}$ (O VII-r line), equivalent to a Doppler shift in either direction of 1100 km s^{-1} . For comparison, the intrinsic wavelength resolution of the *RGS* is $\sim 0.06 \text{ \AA}$ (FWHM) at 21.6 \AA . However, any Doppler broadening is also convolved along the dispersion direction and, depending on its magnitude, could distort the *RGS* images. We present images for the O VIII Ly- α , O VII-resonance (*r*) and O VII-forbidden (*f*) line in Fig. 7.4. We choose these lines because they are the strongest features in the spectrum and because the O VII line ratios are valuable plasma diagnostics. We also extracted an Fe XVII image for the purpose of investigating the Fe emission morphology. The images are all on a $2 \times 2'$ size. The images have been smoothed with a gaussian filter (FWHM of $4''$ for O VIII Ly- α and $8''$ for the rest).

First we turn our attention to the Fe/O emission morphology. The *Chandra* images (Hughes et al. 2003) suggest that most of the O emission originates from the outer shell, while the central region is (as compared to the rim) Fe rich. The *Chandra* observations, however, cannot resolve line blends so these images are possibly contaminated with underlying continuum emission as well as emission from different ion species (e.g. Ne). For this reason we turn our attention to the monochromatic images supplied by the *RGS*. The *RGS* O images and the Fe XVII image (see Fig. 7.4) confirm the *Chandra* results. The Fe XVII image shows a central filled morphology with some emission from the outer region. The O images show more emission from the outer rim with less emission in the central region. We also examined the cross-dispersion profiles, displayed in Fig. 7.5, to ensure the statistical significance of these results. We use the cross-dispersion since we have no velocity distortion in this plane, as opposed to the dispersion direction. Here, again, we see that the Fe emission profile is more centrally peaked as compared to the O emission.

Next we turn our attention to the differences between the morphology of the O VIII Ly- α , O VII-*r* and O VII-*f* emission. The images show significant differences between the three lines. The O VIII Ly- α emission predominantly comes from the rim. The O VII-*r* emission shows a brighter emission spot in the northwestern region while the O VII-*f* line shows a bright emission spot on the East rim. To ensure the statistical

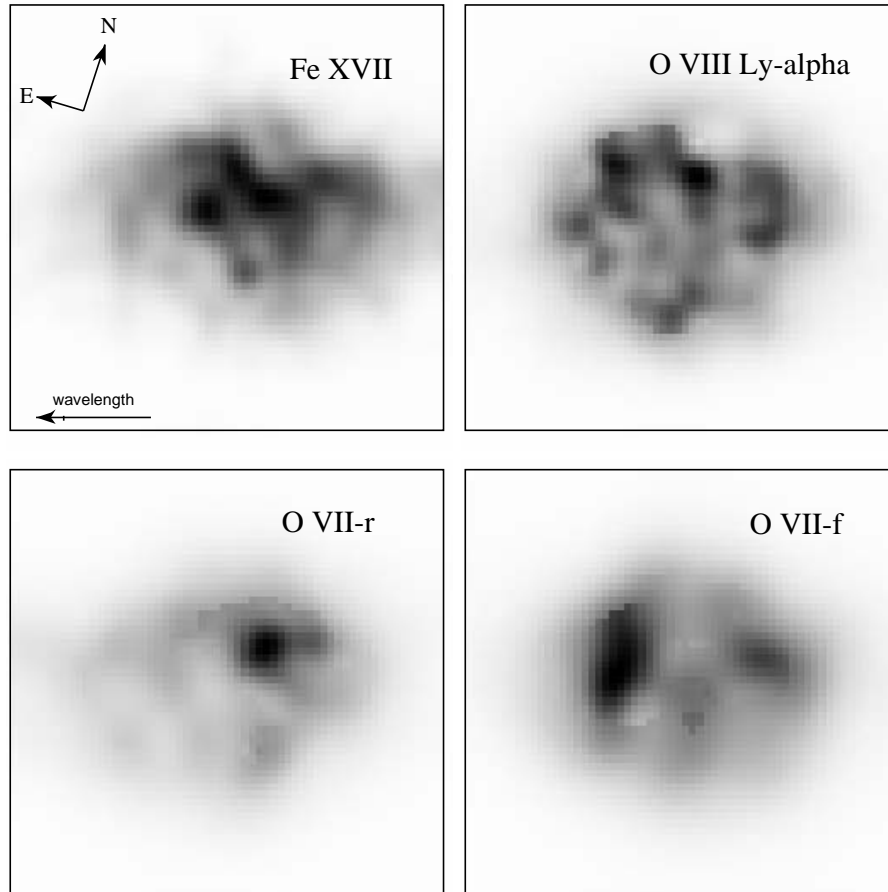


Figure 7.4: *RGS* monochromatic images for Fe XVII (at 17.05 Å) (upper left) O VIII Ly α (upper right), O VII-resonance (lower left) and O VII-forbidden (lower right) lines. The images are plotted with the dispersion and cross-dispersion on the X & Y axis respectively. North is 18° clockwise, as indicated. The *RGS* dispersion direction is such that wavelength increases from right to left in the images.

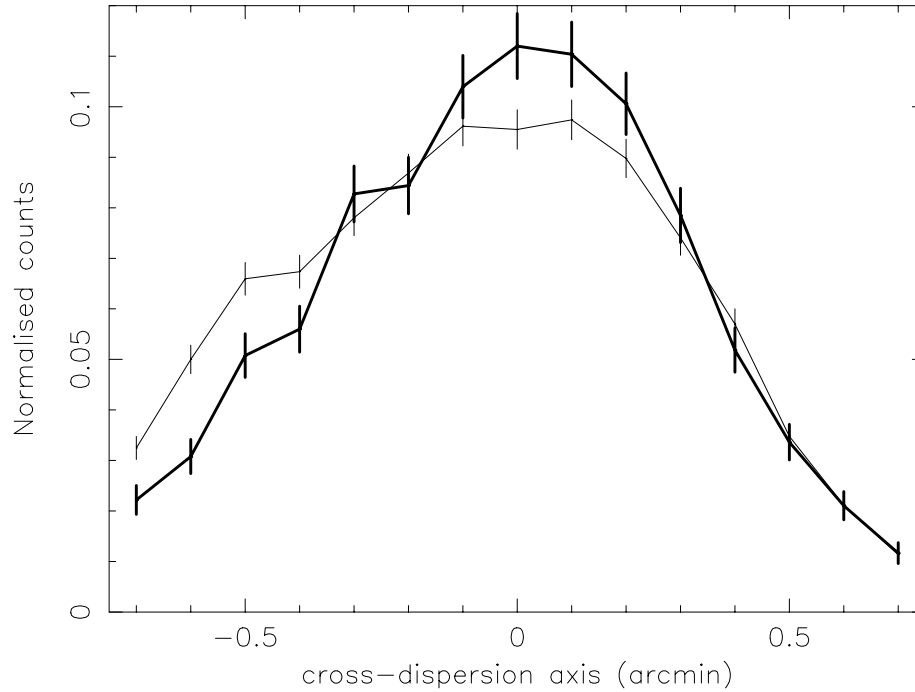


Figure 7.5: *RGS* cross-dispersion profiles for O VIII Ly α (thin solid curve) and Fe XVII (thick solid curve).

significance of these results we consider the dispersion profiles, displayed in Fig. 7.6. We now use the dispersion profiles because the differences in the lines show up more clearly in this plane. These lines should originate from the same location and have the same velocity structure since they are from the same ion. Any velocity distortion between these images should thus be insignificant as compared to the resolution of our instrument. These profiles confirm the variations in the O VII-*f* and O VII-*r* images.

One concern could be the possible contamination of O VII-*r* by its neighbouring O VII-*i* line. Due to the extent of the source, the O VII-*i* line emission from the West rim could show up at the long wavelength shoulder of the O VII-*r* emission line (i.e. the East rim in the O VII-*r* image). So any possible contamination would cause an increase in the O VII-*r* line in the East, we instead see the opposite. The intercombination line is, in any case, weak. We checked the spectra from various cross-dispersion regions, but did not see any evidence for an enhanced *i* line.

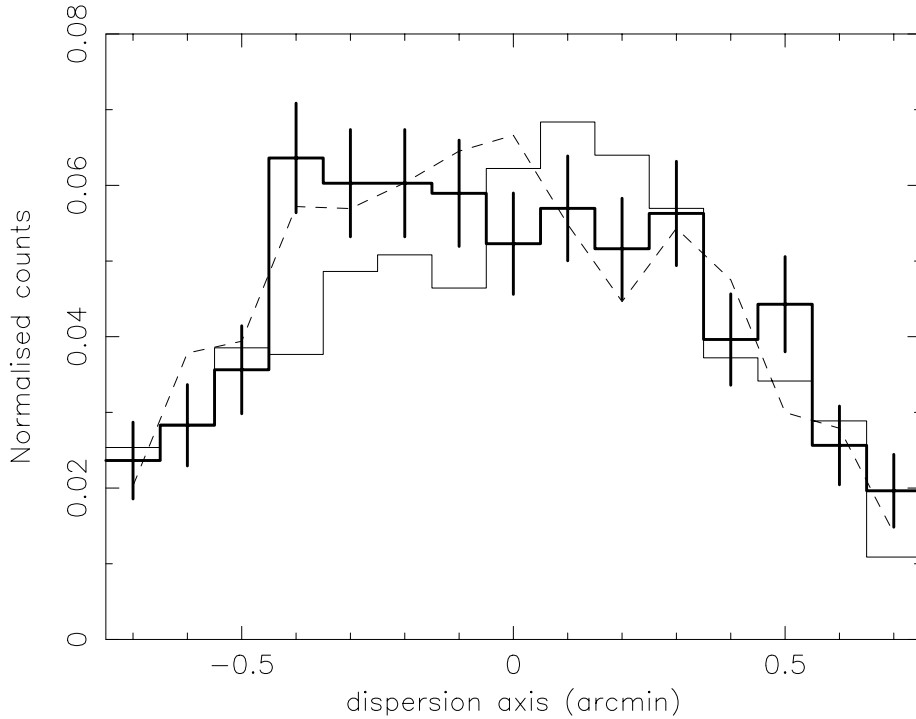


Figure 7.6: *RGS* dispersion profiles for emission lines of O VIII Ly α (dashed curve), O VII-resonance (thin solid curve) and O VII-forbidden (thick solid curve). Error bars are provided for O VII-forbidden line. Errors are typically 50% and 70% smaller for the for the O VIII Ly α and O VII-resonance lines, respectively.

7.4 Discussion

7.4.1 Single Ion Spectroscopy

The O VII f/r line ratios, displayed in Fig. 7.7, indicate considerable temperature and ionisation age variations in the outer shell. To further investigate the implications of the variations in the monochromatic images we studied the O VII f/r ratio. The ratio plot has a mean value of 0.65 and ranges from ~ 1.3 in the East to as low as ~ 0.4 in the northwest. In order to understand the implication of these ratios we computed the O VII f/r for a NEI plasma using numerous combinations of temperatures and

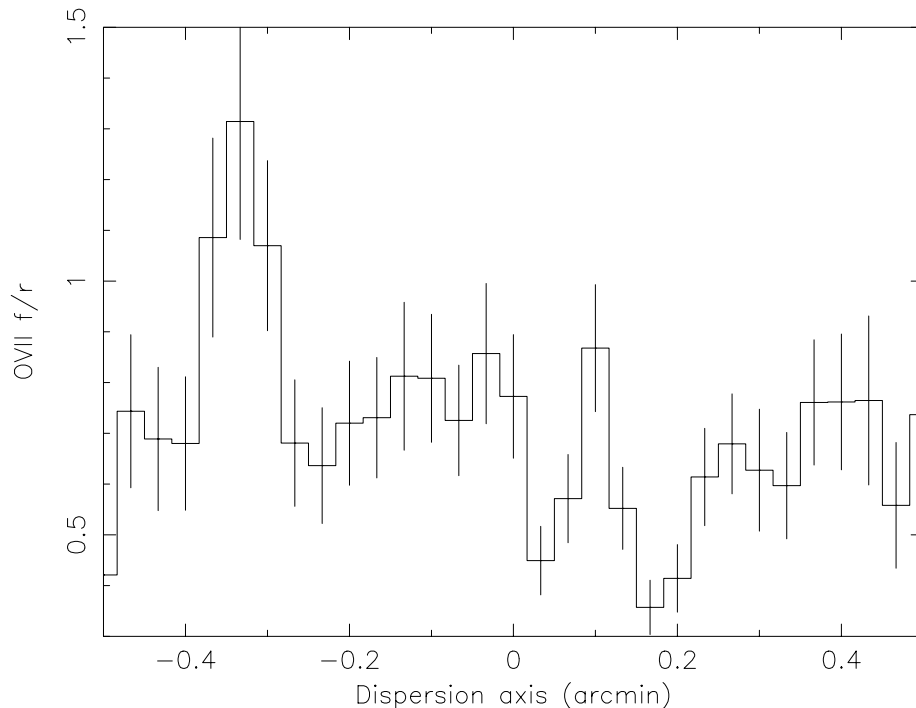


Figure 7.7: *RGS* O VII forbidden/resonance line ratio profile in the dispersion direction.

ionisation ages. The average ratio of ~ 0.65 corresponds to a plasma in the temperature range $kT_e \sim 0.1 - 0.4$ keV with $n_e t > 3 \times 10^{17} \text{ m}^{-3}\text{s}$. The ratio of ~ 0.4 in the northwest indicates an ionisation age and temperature combination ranging from ($n_e t \sim 1 \times 10^{16} \text{ m}^{-3}\text{s}, kT_e \sim 0.3$ keV) to ($n_e t \sim 1 \times 10^{17} \text{ m}^{-3}\text{s}, kT_e \sim 0.6$ keV).

The high f/r value in the East could indicate a low ionisation age ($n_e t \sim 1 \times 10^{15} \text{ m}^{-3}\text{s}$) plasma. However, such a low ionisation age plasma should produce strong O VII-intercombination (i) line emission and we do not see any evidence for this in our data. The observed line ratio can also be obtained if the gas in this region is slowly cooling down to a temperature of ~ 0.1 keV. Such a situation would produce a recombination spectrum with the observed f/r ratio and without a particularly strong O VII- i line. The next question, if we do indeed have a recombining plasma, is the feasibility of cooling in DEM L 71. Recombination effects would become notable if there were some energy draining mechanism operating at the shock front, e.g. particle

acceleration (Dorfi & Böhringer 1993) or radiative shocks. If we assume an initial explosion energy of $E_0 = 1 \times 10^{44}$ J and an electron density $n_e \sim 3.2 \times 10^6 \text{ m}^{-3}$, as obtained in Sect. 7.4.3, then we estimate (according to Falle 1981) that the radiative cooling phase could commence at an age of $\sim 1.4 \times 10^4$ yrs and this time could be reduced if the blastwave encounters higher density ISM material in this region. If we consider that the estimated age of DEM L 71 is 1×10^4 yrs then this, together with the fact that radiative shocks have also been observed by Ghavamian et al. 2000, makes it possible that we have detected the effects of recombination. We attempted to model the *EPIC-pn* spectrum from the East rim with a recombination model. This model gave a good description of the data, but required a Fe abundance of greater than 20 times solar while the other elements had sub-solar abundances. We regard this model as being unphysical. It is probably incorrect to model emission from the entire rim with a recombination model since recombination could only be occurring at a localised region(s) along the rim, as suggested by the bright *f* line emission spot in Fig. 7.4 and the results of the Fabry-Perot observations of Ghavamian et al. (2000).

Alternatively, an increase in the *f/r* line ratio could be introduced by the presence of resonance scattering of the O VII-*r* photons. In the case of resonance scattering the effective velocity broadening needed to calculate the optical depth is determined from the maximum differential velocity over the region with optical depth $\tau = 1$. We estimate a differential velocity of 30 kms^{-1} , given an overall expansion velocity of 800 kms^{-1} . This differential velocity includes both the gradient in the radial velocity component of the shocked gas as well as the effective azimuthal velocity difference due to the finite (azimuthal) extent of the last scattering surface $\tau = 1$. If we assume a uniform spherical shell of thickness $R_s/12$ and a velocity broadening of 30 kms^{-1} , then we could expect an optical depth of $\tau \sim 2.2$ and $\tau \sim 1.0$ in the O VII-*r* and O VIII Ly α lines, respectively. Following the arguments put forward by Kaastra & Mewe (1995), an optical depth of $\tau \sim 2.2$ could produce a factor of 2 reduction in the O VII-*r* line, which would then produce the observed *f/r* ratio. If the O VII emission originated in a homogeneously filled spherical shell then one would expect that, in the presence of resonance scattering, the O VII-*r* line image would be more centrally peaked as the photons would escape along the path of shortest optical length. This morphology is not observed. However, the effects of resonance scattering are highly dependent on the morphology and geometry of the system and resonance scattering could be limited to localised regions. The observed *f/r* ratio in the East could come about if the shock front encountered a dense inter-stellar medium (ISM) clump there. The O VII-*r* photons would then be scattered out of the line of sight, thus producing the observed *f/r* ratio. We neglected the broadening of the line profile due to microturbulence in the estimation of the optical depth. Microturbulence velocities of a few hundred kms^{-1} could reduce the optical depth quite considerably. However, such high microturbulent velocities in DEM L 71 are unlikely.

Further evidence for resonance scattering is provided by the O Line profiles in Fig. 7.6. Since the estimated optical depth in the O VIII Ly α line is unity, the expected

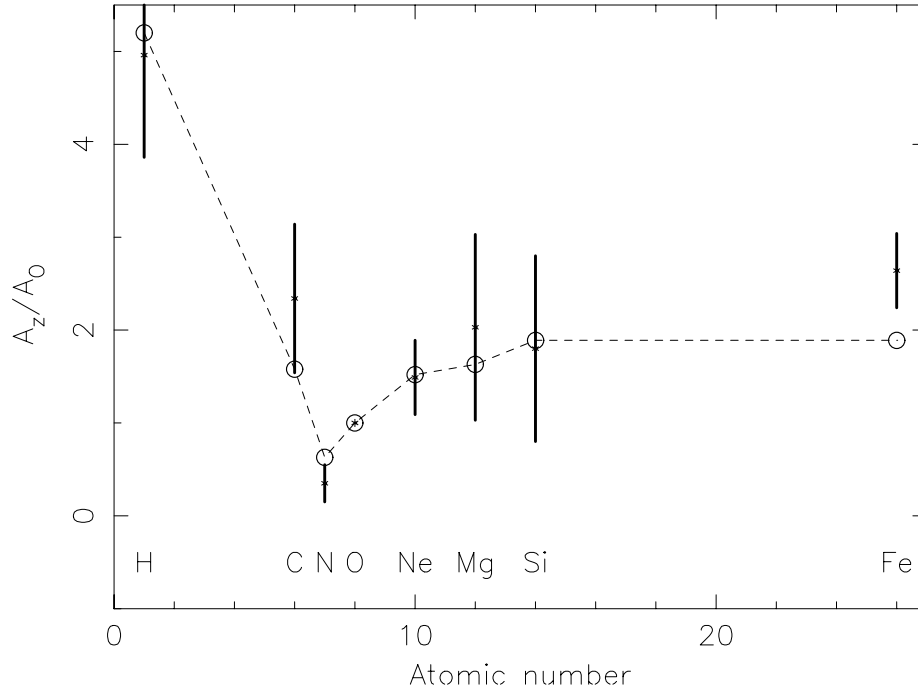


Figure 7.8: Elemental abundance ratios as derived from fits to the *RGS* data. The derived abundance values (crosses) are compared to the average LMC abundance values (open circles). The ratios are all relative to solar (Anders & Grevesse 1989) and normalised to O. The LMC values are from Hughes et al. (1998).

reduction in this line is a factor ~ 3 less than for $O\text{ VII-}r$. The $O\text{ VIII Ly}\alpha$ and $O\text{ VII-}f$ line profiles in Fig. 7.6 are quite similar, while most of the deviation is seen in $O\text{ VII-}r$. This suggests that the high f/r ratio is brought about by a reduction in the $O\text{ VII-}r$ line rather than an enhancement of the $O\text{ VII-}f$ lines. This is exactly what we would expect in the presence of resonance scattering.

7.4.2 Abundances & Morphology

Fig. 7.8 displays the elemental abundance ratios as derived from fits to the *RGS* data. The abundances are all relative to solar (Anders & Grevesse 1989) and normalised to O. The derived abundances are also compared to the average LMC ratios (Hughes et

al. 1998). The plot shows that the observed abundance values are in good agreement with the LMC values. Most of the emission seen by the *RGS* arises from the shell. This is clear from the morphology of the monochromatic line images. The shell also dominates the emission in the *EPIC* images. The outer shell is thus interpreted as being emission from a blast wave which is sweeping up and shock heating ISM material. The idea that the rim emission is from a blast wave heated ISM is supported by the fact that the optical spectrum of DEM L 71 is Balmer-dominated. Balmer-dominated optical spectra can be interpreted well in the context of a model in which a high-velocity interstellar shock overtakes at least partially neutral interstellar gas (Chevalier & Raymond 1978). Analysis of the high spatially resolved *Chandra* ACIS-S CCD image shows that the X-ray outer rim matches the optical H α image nearly perfectly (Hughes 2001).

The inner region is Fe rich. This is evident from the fits to the *EPIC-pn* spectra which give Fe/O \sim 1.6 and Fe/O \sim 6.0 for the shell and inner regions respectively. This Fe enrichment is also visible in the *RGS* results, which show a higher Fe/O ratio as compared to the LMC value. The higher Fe abundance has also been noted in previous ASCA observations (Hughes et al. 1998). This indicates that the inner shell structure seen in the *Chandra* images is (reverse shock heated) Fe-rich SN ejecta. Fe-rich SN ejecta in the inner regions of SNRs is typical for remnants produced by type Ia SN explosion.

7.4.3 Mass estimates

The results of the line ratios show that the two NEI component model used to fit the entire spectrum is highly simplified. These temperature and ionisation age variations in the plasma are probably also the reason why we need at least two components to model the spectra. Despite our simplified model, we can still use the results of the full spectral fits to estimate parameters such as the mean electron densities and emitting masses. We can infer these parameters from the emission measures, but to do this we need to make a volume estimate. The *Chandra* images show that the X-ray emission from both regions originate from limb brightened shells. The inner shell has an average radius of $\sim 23''$ while the outer shell has an average radius of $\sim 37''$. We assume that the outer shell has a thickness of $R_s/12$. We use the radius and shell thickness assumption to estimate the volume, which in turn is used to calculate the electron density and masses. We estimate the outer shell to have an electron density $n_e = 3.2 \times 10^6 / \sqrt{f} \text{ m}^{-3}$ which yields a swept up mass of $M_{shell} \sim 80 M_{\odot} \sqrt{f}$, where f is the (shell) volume filling factor.

The mass estimate of the ejecta (central) region depends on the amount of H mixed into the ejecta during its evolution (see Hughes et al. 2003 for complete explanation). We thus, following the example of Hughes et al. (2003), compute the masses for two astrophysically plausible scenarios; 1) We assume that metals are the sole source of electrons 2) assume that a comparable amount (in mass) of hydrogen has been mixed

into the metal rich ejecta. We use the volume estimate for a spherically symmetric shell. The *Chandra* images indicate an average radius of $\sim 23''$ and a shell thickness of $\sim 11''$ for the central region. A pure metal composition yields $1.1 M_{\odot}$ of Fe and $0.15 M_{\odot}$ of Si, while an admixture of H yields $0.7 M_{\odot}$ of Fe and $0.1 M_{\odot}$ of Si. These values are similar to and confirm the results of Hughes et al. (2003).

There are observational and theoretical indications that type Ia SNe are thermonuclear explosion of accreting white dwarfs (e.g. Nomoto et al. 1994), however, the exact binary evolution has not been identified. Nomoto et al. (1997) provided some constraints on the progenitor system from the viewpoint of nucleosynthesis. They presented nucleosynthesis results for various deflagration speeds to constrain the rate of accretion from the companion star. The measurement of the Si/Fe, S/Fe, Ar/Fe and Ca/Fe mass ratios would be useful to distinguish the type Ia models (Nomoto et al. 1997). We are only able to derive mass estimates for Fe and Si. Nomoto et al. (1997) predicts a Si/Fe mass ratio of ~ 0.25 for the classical (W7) type Ia model and ~ 0.44 for a delayed detonation (WDD2) model. The present data do not allow us to discriminate between models. Deeper observations of DEM L 71 could detect S, Ar and Ca emission which would be useful in identifying the type Ia SNe model.

7.5 Summary & Conclusions

The high resolution *XMM-Newton* emission line spectra of DEM L 71 can be fitted with two NEI plasma components. The *RGS* spectra are dominated by emission from the SNR shell, so the two NEI components needed to fit these spectra indicate a range of temperatures and ionisation ages present in the shell. The temperatures ($kT_e \sim 0.2$ & 0.8 keV) are consistent with the shock temperature ($kT_s = 0.11 - 0.75$ keV) obtained from optical results (Smith et al. 1994). Temperature and ionisation age variations are also evident from the difference in morphology between the O VII *f* & *r* lines. These lines show an anomalously high ratio ($f/r \sim 1.2$) in the East. This ratio could imply that in this region the plasma is cooling and recombining. However, an alternative, and equally interesting, possibility is that the variation in f/r ratios is due to resonance scattering, which would reduce O VII-*r* line emission along lines of sight with a high O VII column density.

The *Chandra* images reveal a double shock structure in DEM L 71. The *EPIC-pn* spectral analysis of these two regions indicates that the inner region ($kT_e \sim 1.1$ keV) is hotter than the shell ($kT_e \sim 0.2 - 0.8$ keV). The abundance ratios of the outer shell is consistent with the average LMC values, while the inner region shows a much higher Fe/O abundance ratio. The outer shell has a much higher mass ($\sim 80 M_{\odot}$) compared to the inner shell ($\sim 2 M_{\odot}$). The image and spectral analysis of DEM L 71 thus suggests that the remnant has a structure consisting of a hot centre surrounded by a cooler shell. This is in agreement with shock models like Truelove & McKee (2001), which predict a hotter interior. The outer rim represents a blast wave moving out

into the ISM, while the interior emission is from reverse-shock-heated Fe-rich stellar ejecta material. The morphology, mass estimates and abundances strongly suggest that DEM L 71 is the result of a type Ia explosion as previously thought. Our analysis also confirms the recent results of Hughes et al. (2003).

DEM L 71 is a good candidate object to study in order to discriminate between the various type Ia supernovae models (e.g. Nomoto et al 1997). However, the current data do not allow for this. Deeper observations would provide better statistics to study the ejecta material in more detail, particularly the density profile of the ejecta plasma and the possible detection of Ar, Ca and Fe-K emission.

Acknowledgements. We thank Ehud Behar for the valuable discussions we had. We also thank the referee J. Ballet for his detailed comments. The results presented are based on observations obtained with XMM-Newton, an ESA science mission with instruments and contributions directly funded by ESA Member States and the USA (NASA). JV acknowledges support in the form of the NASA Chandra Postdoctoral Fellowship grant nr. PF0-10011, awarded by the Chandra X-ray Center. SRON is supported financially by NWO, the Netherlands Organisation for Scientific Research.

References

- Anders, E., & Grevese, N., 1989, *Geochimica et Cosmochimica Acta*, 53, 197
- Bleeker, J.A.M., Willingale, R., van der Heyden, K.J., 2001, *A&A*, 365, L225
- Brickhouse, N. S., Dupree, A. K., Edgar, R. J., et al., 2000, *ApJ*, 530, 387
- Chevalier, R. A., Raymond, J. C, 1978, *ApJ*, 225, L27
- Dorfi, E. A., Böhringer, H., 1993, *A&A*, 273, 251
- Falle, S.A.E.G., 1981, *MNRAS*, 195, 1011
- Feast, M., Whitelock, P., & Menzies, J., 2002, *MNRAS*, 329, L7
- Ghavamian P., Hughes J.P., Rakowski C.E., Williams T.B., 2000, *AASM*, 197.820
- den Herder, J.W., Brinkman, A.C., Kahn, S.M., et al., 2001, *A&A*, 365, L7
- van der Heyden, K.J., Behar, E., Vink, J., et al. 2002, *A&A*, 392, 955
- Hughes, J.P., 2001, in *Young Supernova Remnants Eleventh Astrophysics Conference*, eds., S. S. Holt and U. Hwang, AIP Conference Proceedings, 565, 419
- Hughes, J.P., Hayashi, I., & Koyama, K., 1998, *ApJ*, 505, 732
- Hughes, J.P., Ghavamian P., Rakowski C.E., & Slane, P., 2003, *ApJ*, 582, L95
- Kaastra, J.S., & Jansen, F.A., 1993, *A&AS*, 97, 873
- Kaastra, J.S., Mewe, R., 1995, *A&A*, 302, L13

- Kaastra, J.S., Mewe, R., & Nieuwenhuijzen, H. 1996, in *UV and X-ray Spectroscopy of Astrophysical and Laboratory Plasmas*, p. 411, eds. K. Yamashita and T. Watanabe, Tokyo, Univ. Ac. Press
- Mewe, R., Kaastra, J.S., & Liedahl, D.A., 1995, *Legacy* 6, 16
- Nomoto, K., Hashimoto, M., Tsujimoto, T., et al, 1997, *Nucl. Phys.A*, 616, 79
- Nomoto, K., Yamaoka, H., Shigeyama, S., Kumagai, S. Tsujimoto, T., 1994, in *Supernovae*, p. 199, ed. S. Bladman et al., Elsevier Sci. Publ.
- Smith, R.C., Raymond J.C., & Laming J.M., 1994, *ApJ*, 420, 286
- Strüder, L., Briel, U.G., Dennerl, K., et al., 2001, 365, L18
- Truelove, J. K., & McKee, C. F., 1999, *ApJS*, 120, 299
- Turner, M.J.L., Abbey, A., Arnaud, M., et al., 2001, 365, L27

Chapter 8

Synoptic study of the SMC SNRs using *XMM-Newton*

K.J. van der Heyden, J.A.M. Bleeker, J.S. Kaastra

Submitted to *Astronomy & Astrophysics*

Abstract

We present a detailed X-ray spectral analysis of 13 supernova remnants (SNR) in the Small Magellanic Cloud (SMC). We apply both single-temperature non-equilibrium ionisation models and models based on the Sedov similarity solution, where applicable. We also present detailed X-ray images of individual SNRs, which reveal a range of different morphological features. Eight remnants, viz DEM S32, IKT 2, HFPK 419, IKT 6, IKT 16, IKT 18 and IKT 23, are consistent with being in their Sedov evolutionary phase. IKT 6 and IKT 23 both have a clear shell like morphology with oxygen-rich X-ray emitting material in the centre. We draw attention to similarities between these two remnants and the well studied, oxygen-rich remnant IKT 22 (SNR 0102-72.3) and propose that they are more evolved versions of IKT 22. IKT 5, DEM S 128 and IKT 25 are evolved remnants which are in, or in the process of entering, the radiative cooling stage. The X-ray emission from these three remnants is possibly from the ejecta remains of type Ia SNe. Our modeling allows us to derive estimates for physical parameters, such as densities, ages, masses and initial explosion energies. Our results indicate that the average SMC hydrogen density is a factor of ~ 6 lower as compared to the Large Magellanic Cloud. This has obvious implications for the evolution and luminosities of the SMC SNRs. We also estimate the average SMC gas phase abundances for the elements O, Ne, Mg, Si and Fe.

8.1 Introduction

The low interstellar absorption and relative closeness of the Large and Small Magelanic Clouds (LMC and SMC) allows for the study of individual X-ray sources in these galaxies. For supernova remnants (SNRs) in particular, the low absorption makes it possible to detect X-rays in the important 0.5–3.0 keV energy band, which includes emission lines from highly ionised elements such as O, Ne, Mg, Si, S and Fe. The well known distance of the SMC allows for good estimates of quantities such as physical size, mass, age and so on.

While the LMC SNRs have been relatively well studied, the remnants in the SMC have not received much attention. For example, Hughes et al. (1998) conducted a systematic study of ASCA-SIS spectra of 7 SNRs in the LMC, while Nishiuchi (2001) analysed 9 fainter remnants. They were able to derive good estimates for the physical parameters of individual SNRs. In contrast, while individual or small samples of SNRs in the SMC have been studied (e.g. Mathewson et al. 1983;1984, Yokogawa et al. 2002, Hughes & Smith 1994, Nazé et al. 2002), a detailed synoptic X-ray spectral study has not been carried out. This is mainly because SNRs in the SMC are fainter than their LMC counterparts.

To date a total of 16 SNRs have been identified from a number of extensive X-ray surveys with the instruments aboard the *Einstein*, *ASCA* and *ROSAT* Observatories (e.g. Inoue et al. 1983; Wang & Wu 1992; Haberl et al. 2000). The availability of the *Chandra* and *XMM-Newton* Observatories now provides an opportunity to study these remnants with far greater sensitivity and spatial/spectral resolution than before.

We present *XMM-Newton* observations of 13 SNRs in the SMC. Three remnants, viz. SNR 0039-73.9 (Filipovic et al. 1998), SNR 0050-72.8 and SNR 0058-71.8 (last two both Mathewson et al. 1984), have not yet been covered by the *XMM-Newton* SMC observation fields and are thus not included in this paper. The major emphasis of this work is on the spectral analysis of the CCD-resolution data obtained with the European Photon Imaging Cameras (*EPIC*) (Turner et al. 2001; Strüder et al. 2001). In addition, we also present high resolution spectra of IKT 22 and IKT 23 as measured by the Reflection Grating Spectrometers (*RGS*) (den Herder et al. 2001).

8.2 Observations and Reduction

Our data are extracted from five pointings towards the SMC. The log of the observations are given in Table 1. The pointings, as listed in Table 1, are centred on the remnants IKT 5, IKT 18, IKT 23 and IKT 22 respectively.

The raw *EPIC* data were initially processed with the *XMM-Newton* Science Analysis System (SAS) version 5.4. This involved the subtraction of hot, dead, or flickering pixels, and the removal of events due to electronic noise. The spectra were extracted using the SAS task EVSELECT. We used the standard redistribution matrices available on the VILSPA site, while the ancillary matrices were created using the SAS task

Table 8.1: *XMM-Newton EPIC* observation log.

Rev Nr	Obs ID	Mode		Filt.	Exp. (ks)		RA		DEC	
		pn	MOS		pn	MOS	(J2000)		(J2000)	
156	0110000101	EF	FF	M	23	27	00 49 07	-73 14 06		
157	0110000201	EF	FF	M	16	20	00 59 26	-72 10 11		
157	0110000301	EF	FF	M	31	35	01 04 52	-72 23 10		
247	0135720601	FF	LW	T	16	33	01 03 50	-72 01 55		
433	0135720901	FF	LW	T	14	13	01 04 01	-72 01 51		

Abbreviations used

EF	Extended Full Frame
FF	Full Frame
LW	Large Window
T	Thin filter
M	Medium Filter

ARFGEN. Background subtraction was done by selecting blank sky regions within the same observation.

Mosaic images of the SMC fields were created using our own image and mosaicing software. The image extraction programme selects the photons with the appropriate grades and quality flags and saves the images in FITS file format. The latter is necessary in order to use the standard SAS EEXMAP programme to make exposure maps for each extracted image. EEXMAP produces exposure maps normalized to the on axis exposure time, so each exposure map was multiplied with the appropriate *EPIC-pn* or *EPIC-MOS* effective area by the mosaicing programme. The routines were called from a script that applied those programmes to each event-list and each channel range.

We also have high resolution spectra of IKT 22 and IKT 23 in addition to the CCD-resolution spectra. *RGS* spectra of IKT 22 and IKT 23 were obtained with effective exposure times of 70 and 37 ks respectively. The *RGS* data were processed with SAS version 5.4.

8.3 Analysis and Results

8.3.1 Images

In Fig. 8.1 we present a mosaic of our observations. The left image is a mosaic of *XMM-Newton* revolutions 157, 247 and 433, while the right image shows the southwestern part of the SMC (Rev 156). We are able to identify 13 SNRs in our field, these are indicated in Fig. 8.1 and listed in Table 8.1. All the remnants are quite soft

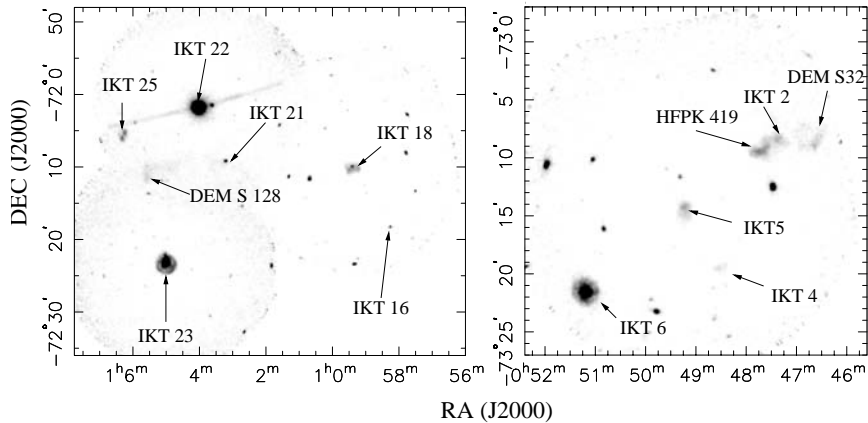


Figure 8.1: Mosaic images of the SMC region. The left image is the combined observations of *XMM-Newton* Rev’s 157, 247 and 433, while the right panel is an image of Rev 156. Individual remnants are indicated. The out-of-time events from IKT 22 can be seen .

X-ray sources, with the peak of their emission in the 0.5–1.0 keV band. A number of point sources, which generally display much harder spectra than the remnants, are also visible in the field-of-view. We present detailed colour coded maps of each remnant in Fig. 8.2. It is clear from Fig. 2 that the remnants exhibit a range of different morphological features. The physical interpretation of these morphologies will be discussed in more detail in Sect. 8.4.1.

8.3.2 Spectral Analysis

The spectral analysis was performed using the SRON SPEX package (Kaastra et al. 1996), which contains the MEKAL atomic database (Mewe et al. 1995) for thermal emission. Also contained in SPEX are a number of plasma models appropriate for SNR analysis.

We extracted spectra from the entire region of each SNR, while the background spectra were taken from nearby blank-sky regions. The extraction regions were constructed so as to exclude possible point source contamination, where applicable. Broad band *EPIC-pn* count rates are given in Table 8.2. The estimated percentage point source or possible residual point source contamination (due to the *XMM-Newton* PSF) is also listed in Table 8.2. The spectra of individual remnants are shown in Figs. 8.3 and 8.4. A typical background spectrum is also displayed in Fig. 8.4. All our

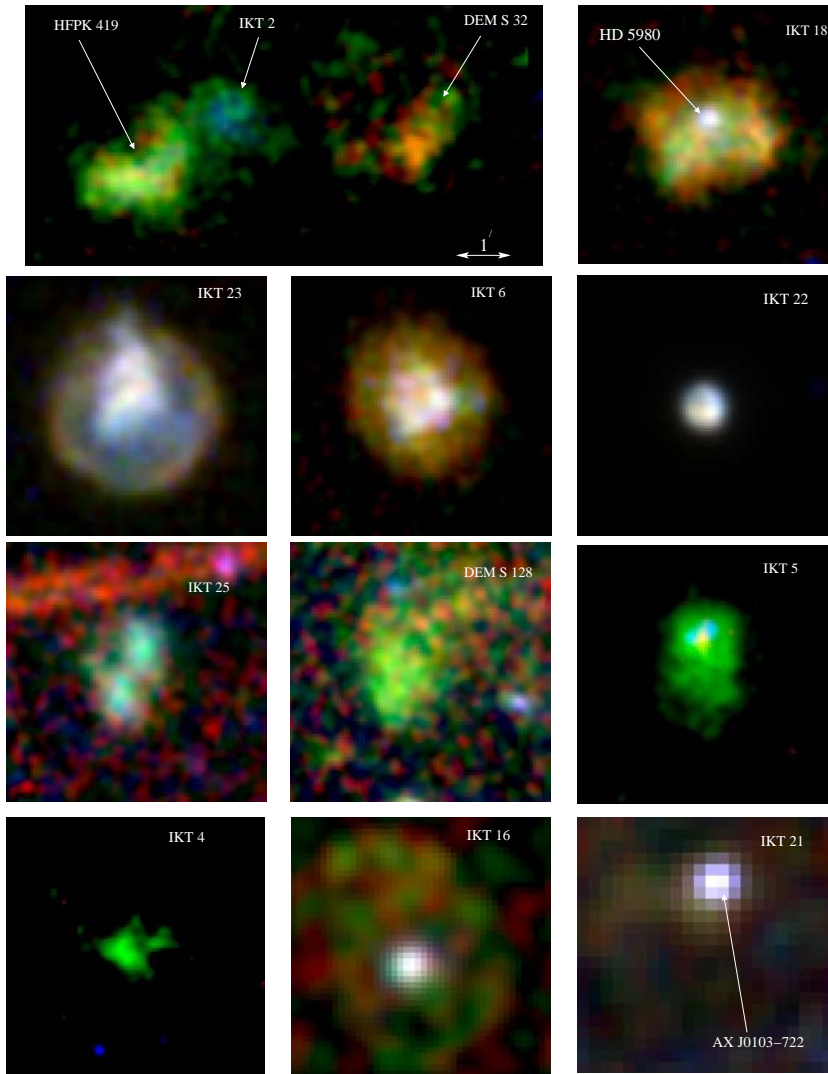


Figure 8.2: Details of the remnants in our sample. Red, green and blue represents the 0.5–0.7 keV, 0.7–1.0 and 1.0–3.0 keV energy bands. All the images are on the same plate scale, as indicated in the upper left image.

Table 8.2: Log of the SNRs in our field.

Object *	SNR Cat.	Obs. ID	RA (J2000)	DEC (J2000)	Count Rate (PN) counts/s	Pnt. src. %
DEM S 32	0044-73.4	0110000101	00 46 39.1	-73 08 39	0.034±0.002	-
IKT 2	0045-73.4	0110000101	00 47 12.2	-73 08 26	0.034±0.002	-
HFFPK 419	(0045.8-73.4)	0110000101	00 47 40.6	-73 09 30	0.087±0.003	-
IKT 4	0046-73.5	0110000101	00 48 24.8	-73 19 24	0.03±0.002	-
IKT 5	0047-73.5	0110000101	00 49 06.9	-73 14 05	0.124±0.004	-
IKT 6	0049-73.6	0110000101	00 51 06.5	-73 21 26	0.482±0.006	-
IKT 16	0056-72.5	0110000201	00 58 16.4	-72 18 05	0.088±0.005	2
IKT 18	0057-72.2	0110000201	00 59 25.4	-72 10 10	0.383±0.007	1
IKT 21	0101-72.4	0123110201	01 03 12.8	-72 08 59	0.120±0.006	35
IKT 22	0102-72.3	0123110201	01 04 02.0	-72 01 48	18.78±0.04	-
IKT 23	0103-72.6	0110000301	01 05 03.5	-72 22 56	2.40±0.01	-
DEM S 128	(0103-72.4)	0123110201	01 05 23.2	-72 09 26	0.042±0.005	3.5
IKT 25	0104-72.3	0123110201	01 06 14.3	-72 05 18	0.092±0.006	15

* Abbreviations used

DEM S H α catalogue of emission nebulæ (Davies et al. 1976)

IKT X-ray catalogue (Inoue et al. 1983)

HFFPK X-ray catalogue (Haberl et al. 2000)

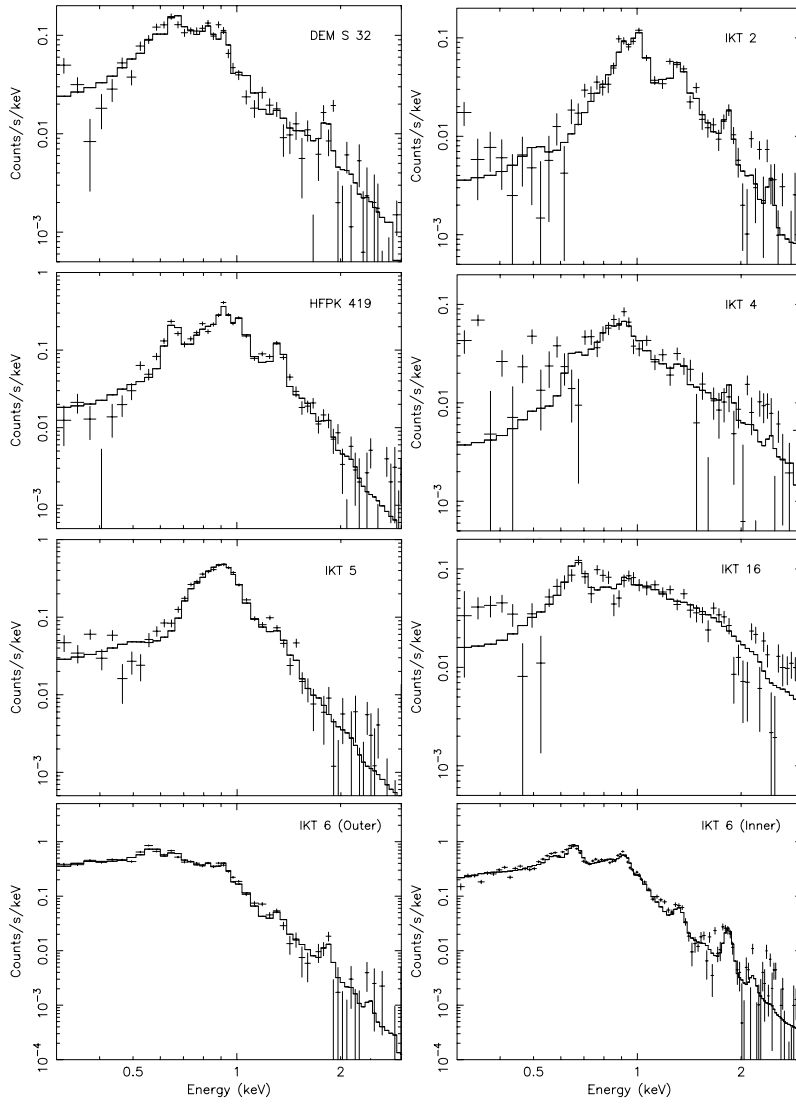


Figure 8.3: Combined *EPIC* (i.e. *EPIC-pn+EPIC-MOS*) background-subtracted spectra of individual SNRs. The crosses represent the data points and error bars and the solid histogram represent the best fit models.

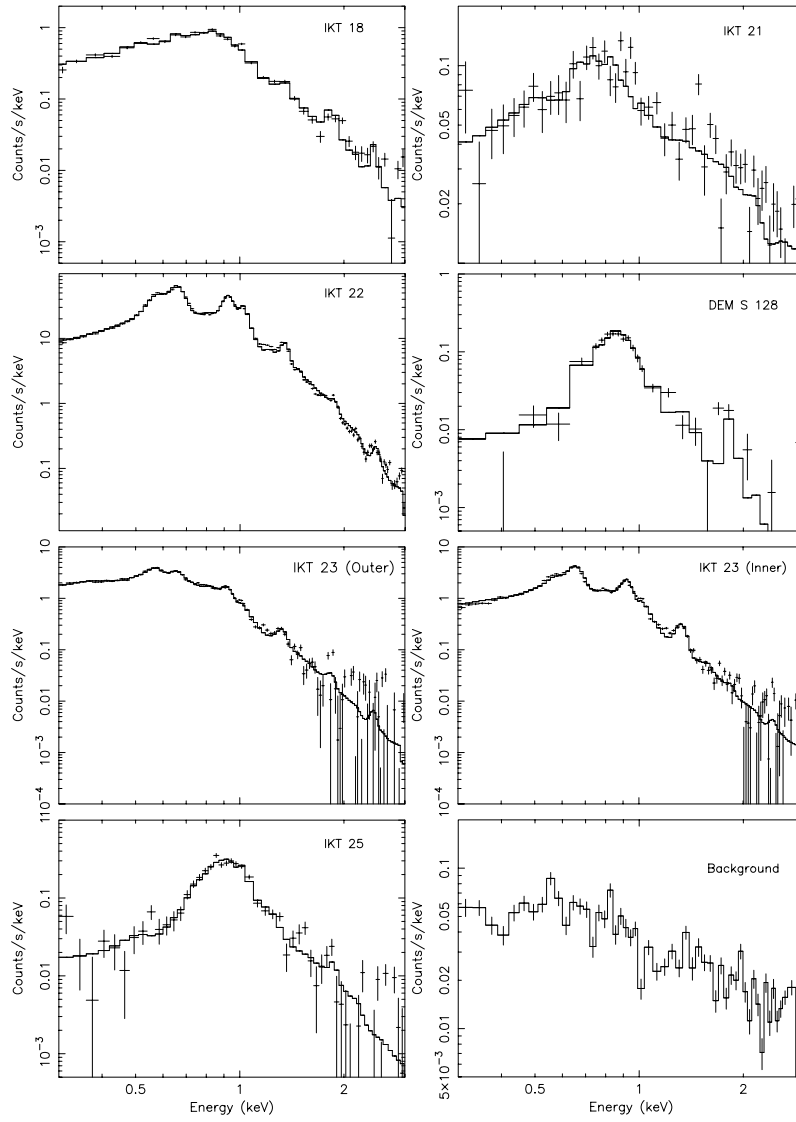


Figure 8.4: Same as for Fig. 8.3. The lower right panel represents a typical background spectrum.

SNR spectra are thermal in nature and show emission from highly ionised atoms of O, Ne, Mg, Si and Fe.

We first attempted to fit all the spectra with a single temperature non-equilibrium ionisation (NEI) model. This assumes that the plasma has been instantly shock-heated to a temperature T_e some time (t) ago. The NEI model does not contain any dynamical model for SNR evolution. In this model we fit the volume emission measure ($n_{es}n_{Hs}V$), the electron temperature (kT_e), the ionisation parameter ($n_{es}t$), the elemental abundances and the column density N_H of absorbing gas along the line of sight. n_{es} and n_{Hs} are the electron and hydrogen density of the shocked gas, respectively and V is the volume of emitting gas. A distance of 60 kpc to the SMC is assumed (Westerland 1990). Both IKT 21 and IKT 25 have point sources in the field which could not be unambiguously excluded in the spectrum extraction. Here we have added power-law components to account for the point emission.

During the fitting procedure we initially kept the abundances fixed at the mean SMC ISM value of 0.2 solar (Russel and Dopita 1992). We started by allowing only the normalisations of the plasma components to vary and subsequently we also allowed the temperature, ionisation age, absorption and abundances (where necessary) to vary. The spectra from *EPIC-pn* and *EPIC-MOS* were fitted simultaneously. The results of the fits are given in Table 8.3. The abundances are all relative to their solar values (Anders & Grevese 1989). We give the unabsorbed luminosities in the 0.5–2.0 keV band.

We also estimated the electron density and radiating mass based on the best-fit emission measure. Here it is provisionally assumed that the emitting gas is confined to shells of a typical thickness $R/12$. The radii were estimated from the X-ray images. The mass estimates indicate that most of the sources are evolved remnants that have swept-up a considerable amount of mass and should thus be emitting in their Sedov phases. Moreover, a number of remnants could not be adequately described by the simple NEI model, in particular, the spectra with higher statistics (viz, IKT 6, IKT 22, IKT 23). These spectra appear to show an ionisation and/or temperature distribution. We thus consider a Sedov model to be the most appropriate for fitting the data. This model is based on the Sedov solution (Sedov 1959) which describes the self-similar expansion of an adiabatic blast wave in a homogeneous medium.

We proceed to fit the IKT 6, IKT 18, IKT 22 and IKT 23 spectra with a Sedov model, based on unacceptable χ^2 's and large swept-up mass, obtained from the NEI model fits. IKT 6 and IKT 23 have a shell and centrally filled morphology. We extract and fit only the shell part of the spectra of these two remnants with a Sedov model. The *Chandra* data reveal that IKT 22 has a blastwave and reverse shock structure (Hughes et al. 2000), however, *XMM-Newton* cannot resolve these two regions so we fit the spectrum extracted from the entire remnant. Even though IKT 22 is clearly less evolved than IKT 6 and IKT 23 (for example), we do find that the Sedov model provides a much better fit to the data. Hayashi 1997 also found that Sedov model fits to the *ASCA* data of IKT 22 gave the most reliable results. We also fit, based on the

high mass estimates for the NEI fits, the DEM S 32, IKT 2, HFPK 419, and IKT 16 spectra with a Sedov model.

The free parameters of the Sedov model are the normalisation ($n_e n_H R^3/d^2$), shock temperature (T_s), ionisation parameter ($I_t = n_e t_i$), elemental abundances and the column density N_H of absorbing gas. Here n_e is the pre-shock electron density, t_i is the ionisation age of the remnant, R is the SNR shock radius and d is the distance to the source. The fitting procedure for the Sedov models is the same as in the case of the NEI models. The fit results are summarised in Table 8.4.

From these fits, we can estimate several physical parameters for the SNRs in question. If n_e is the electron density, n_H is the hydrogen density, n_m is the total number density of protons+neutrons (including those bound up in nuclei), then, using the elemental abundances and assuming a fully ionised plasma we can calculate the number of electrons per hydrogen atom $r_e = n_e/n_H$ and the effective number of protons and neutrons (baryon mass) per hydrogen atom $r_m = n_m/n_H$. By adopting the values of the parameters mentioned above we estimate the electron density (n_e), the hydrogen density (n_H), the Sedov dynamical age (t_{dyn}), the effective ionisation age (t_i), the total emitting mass (M) and initial explosion energy (E_0) by using:

$$n_e = \sqrt{N r_e d^2 / R^3}, \text{ m}^{-3} \quad (8.1)$$

$$n_H = \sqrt{N d^2 / (R^3 r_e)}, \text{ m}^{-3} \quad (8.2)$$

$$t_{dyn} = 1.3 \times 10^{-14} R / \sqrt{T_s}, \text{ yr} \quad (8.3)$$

$$t_i = 3.17 \times 10^{-8} I_t / n_e, \text{ yr} \quad (8.4)$$

$$M = 5 \times 10^{-31} m_p r_m n_H V, \text{ M}_\odot \quad (8.5)$$

$$E_0 = 2.64 \times 10^{-15} T_s R^3 n_H, \text{ J} \quad (8.6)$$

Here m_p (kg) is the proton mass, R (m) is the shock radius, T_s (keV) is the shock temperature, I_t ($\text{m}^{-3} \text{s}$) is the ionisation parameter and $V (= 4/3\pi R^3)$ is the total volume. We do not apply a volume filling factor to our estimates (eqs. 8.1–8.6) as it is already implicitly contained within the Sedov model. We assume that the remnants are spherically symmetric. The results are given in Table 8.5. The mass estimates based on the NEI fits compare well to those obtained from the Sedov model fits. However, any deviation from symmetry (e.g. fragmentary shells) or sphericity will, of course, affect the volume estimates which in turn influences the estimates of derived parameters such as densities, explosion energy and mass. The effect of an incorrect volume estimate on the derived parameters can be estimated by applying a volume factor $f = \sqrt{V_t/V_s}$, where V_t is the true emitting volume and V_s is the estimated volume for spherical symmetry. The following corrections would then hold: $(n_e, n_H, E_0) \times 1/f$ and $(M, t_i) \times f$. For example, an ellipsoidal morphology with one axis 20% larger than the radius of a sphere would give $f \sim 1.1$.

We also fit the spectra from the inner regions of IKT 6 and 23. As a model we use one NEI component to account for emission from the central region. In addition to

this, we added the same plasma component and parameters as derived from the fits to the outer region, only the normalisations from these components were allowed to vary. This method accounts for any projected fore/background shell emission. The fit results supplied in Table 8.3, are very similar between the two remnants.

The best fit models generally provides good fits to the data, though a few discrepancies exist. Uncertainties in the modeling of the data include the calibration differences between the *EPIC-pn* and *EPIC-MOS* and incompleteness of the atomic database. For example, the most prominent residual is the underestimation of the spectra at ≈ 1.2 keV. This is a known problem and is probably due to missing high excitation lines of Fe XVII-XIX in the plasma code (see Brickhouse et al.2000).

Shock waves in the shells of SNRs are thought to be collisionless because at the low densities encountered in remnants the shock front is thinner than the mean free path for collisions. The actual heating mechanism in collisionless shocks is not straightforward and needless to say, not well understood. The heating of particles at the shock-front is thought to be produced by collective processes, such as plasma waves (for a review see for instance, Draine & McKee 1993; Laming 2000). Since the heating is not collisional the plasma can be regarded as a two fluid system consisting of electrons and ions. There is no guarantee that there will be equilibration between the electron and ion temperature. We therefore investigated the effect of non-equipartition on our derived parameters, as our model fits assume equilibration between electron and ion temperatures. We fitted a sample of our brighter remnants with a Sedov model in which the electron temperature lags the shock temperature (see Borkowski et al. 2001). We initially left both the shock and electron temperature free, but both these values tracked each other. We then imposed fixed shock to electron temperature ratios of 0.5 and 0.2. We found that the derived parameters, except for the ionisation parameter and emission measure, did not differ significantly from the electron-ion temperature equilibration models. In fact, we obtained slightly better fits (in terms of reduced χ^2) with the equilibration models. This could be because most of our remnants are evolved and have already attained or are approaching electron-ion temperature equilibration.

8.4 Discussion

8.4.1 Progenitor Types

Core–Collapse candidates

IKT 6 and IKT 23 are remarkably similar remnants, both morphologically and spectrally (Figs. 8.3 and 8.4). IKT 23 has a clear shell and a centrally filled morphology. The colours in Fig. 8.2 indicate that the outer region is softer than the inner region. IKT 6 exhibits a similar morphology, although it is not as clearly resolved. IKT 6 is located towards the edge of the detector where the effective area and spatial resolution is lower. The other remnant in our sample with a clear shell structure is IKT 22. This

Table 8.3: NEI model spectral fitting results. The fit errors (1σ) are given in brackets. The abundances are all relative to their solar values (Anders & Grevese 1989).

SNR	Radius (arcsec)	N_{H} (10^{25} m^{-2})	$n_e n_{\text{H}} V$ (10^{64} m^{-3})	kT_e (keV)	$n_e t$ ($10^{16} \text{ m}^{-3} \text{ s}$)	n_e (10^6 m^{-3})	Mass M_{\odot}
DEM S 32	68	2.4(0.7)	0.60(0.25)	1.51(0.48)	1.0(4.5)	0.18	39
IKT 2	33	3.9(1.5)	1.5(1.4)	0.77(0.59)	>20.0	0.84	21
HFPK 419	45	3.9(1.5)	1.21(1.1)	0.62(0.39)	>13.0	0.48	30
IKT 4	42	6.2(0.9)	0.14(0.03)	3.5(1.4)	2.1(0.2)	0.18	9
IKT 5	58	1.1(0.9)	0.47(0.23)	0.71(0.04)	>48.0	0.20	27
IKT 6	74	0.6(0.2)	5.9(0.8)	0.54(0.03)	3.5(0.4)	0.50	139
IKT 16	100	0.6(0.5)	1.9(0.4)	1.6(0.4)	0.37(0.07)	0.17	104
IKT 18	79	2.5(0.5)	9.1(3.5)	0.57(0.12)	2.7(+100)	0.56	190
IKT 21*	31	2.0(0.8)	0.48(0.31)	0.58(0.40)	4.3(+100)	0.53	11
IKT 22	24	1.1(0.1)	73.2(5.6)	0.38(0.01)	>600	9.62	93
IKT 23	99	0.4(0.1)	9.3(1.3)	0.68(0.04)	2.5(0.4)	0.41	270
DEM S 128	62	1.8(1.2)	0.17(0.12)	0.61(0.13)	>200	0.11	18
IKT 25	55	4.8(1.7)	1.2(0.5)	0.60(0.11)	38(20.0)	0.36	40
IKT6-inner	30	0.8(0.1)	0.13(0.06)	0.89(0.16)	5.4(2.1)	0.29	5
IKT23-inner	40	1.1(0.1)	0.22(0.08)	0.92(0.12)	2.8(0.5)	0.25	11

* plus power-law component, norm. $\sim 2.2 \times 10^{43} \text{ phs}^{-1} \text{ keV}^{-1}$ and $\gamma \sim 0.9$
+f - fixed

continued ...

Table 8.3 continued :

SNR	O	Ne	Mg	Si	Fe	$L_x(0.5-2 \text{ keV})$ (10^{27} W)	$\chi^2/\text{d.o.f}$
DEM S 32	0.20(0.06)	0.23(0.08)	<0.10	0.29(0.21)	0.08(0.05)	19	190/151
IKT 2	<0.10	0.81(0.42)	0.72(0.35)	0.41(0.13)	0.13(0.09)	14	152/155
HFPK 419	1.2(0.9)	1.9(1.5)	1.6(1.4)	0.24(0.19)	0.39(0.34)	42	192/155
IKT 4	0.2(f)	0.2(f)	0.2(f)	0.2(f)	0.2(f)	18	205/155
IKT 5	<0.1	0.92(0.65)	0.93(0.45)	<0.1	0.91(0.35)	9.6	340/320
IKT 6	0.11(0.01)	0.24(0.03)	0.17(0.04)	0.42(0.2)	0.09(0.01)	66	610/320
IKT 16	0.2(f)	0.2(f)	0.2(f)	0.2(f)	0.2(f)	61	162/109
IKT 18	0.06(0.02)	0.09(0.04)	0.07(0.03)	0.25(0.1)	0.07(0.1)	62	333/153
IKT 21	0.20(f)	0.20(f)	0.20(f)	0.20(f)	0.20(f)	8.0	416/361
IKT 22	2.0(0.1)	2.5(0.2)	1.5(0.1)	0.65(0.09)	0.10(0.01)	150	3043/212
IKT 23	0.14(0.01)	0.28(0.02)	0.21(0.02)	<0.1	0.07(0.01)	150	1103/320
DEM S 128	<0.1	<0.1	2.6(1.1)	2.4(1.6)	2.34(1.1)	7.8	125/115
IKT 25	<0.1	3.0(1.2)	<0.1	<0.1	1.5(0.4)	45	139/156
IKT6-inner	2.0(0.6)	2.3(0.8)	1.6(0.9)	2.7(1.2)	0.87(0.31)	17	180/155
IKT23-inner	2.1(0.5)	4.7(1.2)	3.3(1.3)	0.2(f)	0.55(0.15)	37	410/320

Table 8.4: Sedov model spectral fitting results. The fit errors (1σ) are given in brackets. The abundances are all relative to their solar values (Anders & Grevesse 1989).

SNR	N_{H} (10^{25} m^{-2})	$n_e n_{\text{H}} R^3 / d^2$ (10^{20} m^{-5})	kT_e (keV)	$n_e t$ ($10^{16} \text{ m}^{-3} \text{ s}$)	$L_x(0.5 - 2 \text{ keV})$ (10^{27} W)
DEM S 32	1.9(0.6)	1.70(0.7)	1.29(0.46)	2.5(1.1)	16
IKT 2	5.1(1.2)	16.3(9.3)	0.39(0.05)	>220	20
HFPK 419	4.4(0.9)	12.7(5.2)	0.28(0.03)	>360	57
IKT 6-outer	0.7(0.2)	22.5(7.5)	0.27(0.05)	11.1(0.5)	39
IKT 16	5.1(0.6)	4.32(1.8)	1.76(0.65)	0.51(0.1)	39
IKT 18	1.3(0.2)	15.4(5.1)	0.51(0.06)	20.0(10.1)	39
IKT 22	0.60(0.06)	99.3(11)	0.78(0.08)	9.0(+1.7)	1.3×10^3
IKT 23-outer	0.5(0.1)	51.9(5.8)	0.26(0.03)	20.0(0.4)	85

SNR	O	Ne	Mg	Si	Fe	$\chi^2/\text{d.o.f}$
DEM S 32	0.28(0.15)	0.17(0.14)	0.19(0.14)	0.45(0.26)	0.23(0.1)	164/149
IKT 2	<0.08	0.89(0.39)	0.51(0.23)	0.33(0.17)	<0.1	152/149
HFPK 419	1.25(0.45)	2.19(0.74)	1.65(0.54)	0.13(0.1)	0.25(0.1)	193/150
IKT6-outer	0.13(0.03)	0.28(0.08)	0.3(0.12)	0.4(0.3)	0.15(0.04)	223/155
IKT 16	0.2(f)	0.2(f)	0.2(f)	0.2(f)	0.2(f)	199/165
IKT 18	0.14(0.07)	0.11(0.07)	0.22(0.09)	0.44(0.13)	0.17(0.03)	253/153
IKT 22	0.87(0.05)	1.99(0.10)	1.32(0.09)	0.21(0.03)	0.29(0.02)	841/211
IKT23-outer	0.17(0.02)	0.28(0.04)	0.35(0.07)	0.36(0.15)	0.11(0.02)	460/320

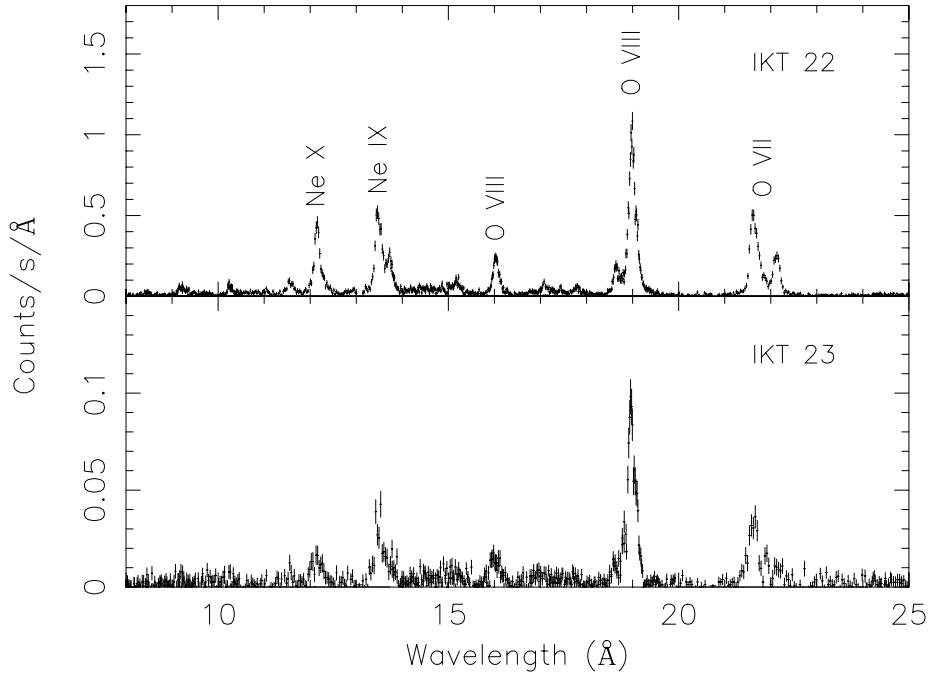


Figure 8.5: *RGS* spectrum of IKT 22 (top) and IKT 23 (bottom). The most prominent emission lines are labeled.

Table 8.5: Physical parameters derived from the best fit Sedov model results.

SNR	n_e (10^6 m^{-3})	n_H (10^6 m^{-3})	t_i (10^3 yrs)	t_{dyn} (10^3 yrs)	Mass (M_{\odot})	E_0 (10^{44} J)
DEM S 32	0.05	0.05	15	6	43	0.9
IKT 2	0.45	0.44	>34	5.4	47	0.3
HFPK 419	0.26	0.25	>50	8.5	64	0.6
IKT 6-outer	0.21	0.17	18	14	180	0.8
IKT 16	0.05	0.04	3.5	7.5	124	3.4
IKT 18	0.13	0.11	23	11	196	1.2
IKT 22	2.03	1.68	1.4	2.7	84	0.8
IKT 23-outer	0.19	0.16	30	19	424	1.8

remnant is quite striking since it is orders of magnitude more luminous than the other SNRs in the field.

The spectra extracted from the two regions (i.e. outer and inner) of IKT 6 and IKT 23 (see Figs. 8.3 and 8.4) are distinctly different. However, the spectra are remarkably similar between the two remnants. The spectral fitting results given in Tables 8.3 and 8.4 also yield similar parameters for the two remnants. Although not clearly visible in the *XMM-Newton* data (because of the lower spatial resolution), the *Chandra* data do reveal that IKT 22 has a blastwave and reverse shock structure (Hughes et al. 2000). The spectra from these two regions are also distinctly different.

The abundance derived from the fits to the outer regions of IKT 6 and IKT 23 are consistent with the SMC ISM abundances, while the inner regions reveal much higher abundance values. We propose, based on the abundance profiles, that the inner region represents reverse shock heated ejecta material while the outer region represents a blastwave moving through the ISM/CSM. The fit results also show that the inner (ejecta-rich) regions are hotter ($kT \sim 0.9$ keV) than the outer regions ($kT \sim 0.27$ keV). This is expected from models such as proposed by Truelove and McKee 2001, which predict that the blastwave in more evolved remnants eventually attains a lower velocity than the reverse shock.

The spectra extracted from the inner regions of IKT 6 and IKT 23 are also similar to the IKT 22 spectrum. All three remnants show enhanced O, Ne and Mg abundances with respect to Fe. The abundance values of these elements (w.r.t. solar) are also an order of magnitude larger than their SMC ISM values. We also obtained *RGS* spectra of IKT 22 and IKT 23. The spectra were extracted from the entire remnants. The high-resolution *RGS* spectra of IKT 22 and IKT 23, displayed in Fig. 8.5, again bear striking similarities and reveal prominent emission lines of O and Ne species. The emission lines in both these spectra are dominated by reverse-shock heated ejecta. The most obvious difference between the two spectra is in the count rate. The flux in the emission lines of IKT 22 are an order of magnitude larger than compared to IKT 23. Much of this flux difference can be attributed to the differences in volume. The ejecta material in IKT 22 is contained in a much smaller volume than compared to IKT 23. The higher density in IKT 22 leads to a higher emission measure. A more detailed *RGS* analysis of IKT 22 is provided by Rasmussen et al. (2001).

The similarities between IKT 6, IKT 22 and IKT 23 suggests that these three remnants have common progenitors. IKT 22 is a well studied remnant that has been classified as being the result of a type II SN. IKT 6 and IKT 23 should thus also be the remnants of type II SNe. Both the derived abundances and masses for the inner regions of IKT 6 and IKT 23 are consistent with this interpretation. These remnants represent very different stages of SNR evolution. IKT 22 is a ~ 2000 yr old remnant (Blair et al. 1989) while IKT 6 and IKT 23 are much more evolved (14 000–20 000 yr). We propose that IKT 6 and IKT 23 are evolved versions of IKT 22 and studying these remnants in more detail presents a unique opportunity to probe the evolution of oxygen-rich remnants in the SMC. It is also interesting to note that the ejecta are

still visible in remnants as evolved as IKT 6 and IKT 23.

IKT 2 and HFPK 419 are located in the large emission nebulae N19. These remnants have rather irregular and complicated X-ray morphologies. For example, it is not clear whether IKT 2 and HFPK 419 are indeed two separate remnants or part of a larger SNR. However, the spectra from these remnants are rather different, which indicate that they might actually be two separate objects. IKT 2 and HFPK 419 both show high metal abundances, which indicate that much of the X-ray emission is from ejecta enriched material. Their abundance profiles show a similar pattern in that the Ne and Mg abundances are higher than Fe (see Table 8.4). While the Ne and Mg abundances are enhanced above the SMC mean by only 2–3 σ , the combined abundances are enhanced at the 5 σ level. Furthermore, the Si and Fe abundances are lower and in line with their SMC values. The enhanced Ne and Mg abundances, as compared to the Si and Fe values, indicate a core-collapse origin (e.g. Nomoto et al. 1997; Woosley & Weaver 1995). We thus suggest, based on their abundance profiles, that these remnants are the results of core-collapse SNe. This is also in agreement with their surroundings which suggest recent, at least modest, starburst activity (Dickel et al. 2001). Yokogawa et al. (2002) analysed *ASCA* and *ROSAT* data of IKT 2 and also find enhanced abundances, even though their age estimate is rather large. They suggest that IKT 2 is the result of a core collapse SN with a progenitor mass of $\lesssim 20 M_{\odot}$.

IKT 16 is one of the weaker X-ray sources in our sample. The X-ray morphology appears consistent with the radio and H α classification of it being a shell like SNR (Mathewson et al. 1984). A harder emission spot can be seen in the centre of the X-ray image. We attempted to extract a separate spectrum from this region, but the data is of insufficient quality to speculate on the X-ray nature of this region. A longer exposure observation is needed to investigate whether this source is thermal or non-thermal in nature.

Also interesting is the high explosion energy ($\sim 3.3 \times 10^{44}$ W) and low ionisation age ($t_i \sim 3500$ yr) associated with IKT 16. The fit parameters are not very well constrained due to the low count rate so the discrepancies might originate from statistical limitations. However, in their analysis of the LMC remnants, Hughes et al. (1998) found a connection between low ionisation age (as compared to the dynamical age) and high explosion energy. They explain this connection as SNRs which exploded within pre-existing low-density cavities in the ISM. The remnant expands rapidly to the cavity wall, where it then encounters denser gas and begins to emit X-rays. This results in a lower dynamical age and explosion energy than that inferred from the Sedov model. A similar scenario could thus be applicable to IKT 16. If this is the case, then IKT 16 would be the result of the core-collapse of a massive star whose stellar wind has caused a low density circumstellar cavity.

Type Ia candidates

The images in Fig. 8.2 show that IKT 5, DEM S 128 and IKT 25 have similar diffuse X-ray morphologies with no clear shell like structure. The emission peaks in the 0.7–1.0 keV band. This indicates that the flux of these sources are dominated by emission from Fe-L transitions. The X-ray sizes of IKT 5, DEM S 128 and IKT 25 are much smaller than their optical or radio diameters (see Mathewson et al. 1983; Mathewson et al. 1984; Filipovic et al 2000). The large optical diameters imply that they are evolved remnants. Mathewson et al. (1984) also attributes the high S II emission detected in IKT 5 and IKT 25 to the onset of radiative cooling due to the evolved nature of these remnants. In this scenario IKT 5, DEM S 128 and IKT 25 would have evolved to such a degree that the shells have eventually become too faint or too cool to be seen in X-rays and we only see the hotter Fe-rich ejecta remains. The morphologies and temperature structure of IKT 6 and IKT 23 also add credence to such a scenario.

We fitted the spectra of these three remnants with NEI models. Hughes & Smith 1994 reported a point source, possibly a Be-binary system, with a power law spectrum in the field of IKT 25. We thus added a power-law component to the NEI model of IKT 25. We fixed the photon index of the powerlaw to 1.5 and flux to $1 \times 10^{-16} \text{ W m}^{-2}$ (Hughes et al. 1994), since we could not constrain any power-law parameters in our data. The best fit parameters are given in Table 8.3. These fits also show enhanced Fe abundances. Although the spectra of IKT5, DEM S 128 and IKT 25 were well fitted with an NEI model with free abundances, we could not constrain the abundances very well due to the limited statistics. What is obvious, though, is that the Fe abundance values were consistently, and at least 3σ , above the SMC mean metallicity. We also tried to fix the abundances, except for Fe, to the SMC mean, but here it is also clear that we need an enhanced Fe abundance. It has been argued (e.g. Nishiuchi et al. 2001; Hughes et al. 1995) that the excess of emission around 1 keV, interpreted as an overabundance of iron, may suggest that the progenitor of the SNR origin was a type Ia SN. The apparent excess emission around ~ 0.9 keV and the high Fe abundance in these remnants suggests that these remnants are the result of type Ia supernovae. A possible interpretation is that these remnants are much more evolved versions of SNR DEM L 71 in the LMC (Hughes et al. 2003; van der Heyden et al. 2003). Here we see a bright ISM dominated shell with fainter Fe-rich ejecta material in the centre. However, higher resolution spectroscopy is necessary to investigate the abundance profiles of these remnants in more detail. It should also be noted that an association between IKT25 and the Be-binary system would imply that this SNR would be the remnant of a massive star rather than a type Ia SN.

The cases of IKT 18, DEM S 32, IKT 21 and IKT 4

IKT 18 has a rectangular shape. The emission is diffuse with no obvious limb brightening. The *Chandra* data (Nazé et al. 2002) do reveal a few bright or dark arcs, but apart from these, the brightness is rather uniform. The luminous blue variable

(LBV) HD 5980 can also be seen in the centre of IKT 18. The spatial coincidence of IKT 18 with the peculiar binary system HD 5980 suggests an association with this system. The possible association was recently investigated by Nazé et al. (2002). They drew attention to similarities between IKT 18 and the Carina nebula. However, they concluded that based on the non-thermal radio emission (Ye et al. 1991) and a high velocity expansion (Chu & Kennicutt 1988), IKT 18 should be regarded as a SNR with HD 5980 located behind the remnant.

The results of our NEI model fits differ from those obtained by Nazé et al. (2002) (Mekal model fits to the *Chandra* data) and Yokogawa et al. (2002) (NEI model fits to the ASCA data) in that our column density is a factor of 2 higher and our abundances are generally lower. However, Yokogawa et al. (2002) fixed their abundance values to 0.2 times solar while the model used by Nazé et al. (2002) only gives a mean metallicity. It should be noted that the results obtained from fits to the *XMM-Newton*, *Chandra* and ASCA data set are generally consistent within the errors. All three spectral analyses give a total X-ray emitting mass estimate of 100-200 M_{\odot} , which indicate that this remnant is in the Sedov evolutionary stage. We thus proceeded to fit our data with a Sedov model. This model gave abundances profiles which are very much in line with the SMC ISM abundances of Russel & Dopita (1992). The low SMC-like abundances and high mass (196 M_{\odot}) and age estimate (11 000 yr) derived from our fits are also consistent with the picture of an evolved SNR which has swept-up ISM material. While the low abundances do not allow for a progenitor typing, Yokogawa et al. (2002) argue that the location in a giant H II region prefers a type II origin. More *XMM-Newton* data will be available in the near future, which will allow for a more detailed assessment of the nature of this object.

DEM S 32 is another remnant, as is IKT 2 and HFPK 419, in the vicinity of N19. It has a shell-like structure with enhanced emission towards the southwestern limb. The abundance yields from DEM S 32 are lower than for IKT 2 and HFPK 419 and no clear distinction in progenitor type can be inferred from these yields. The environment (N19), however, might suggest that DEM S 32 has a massive star progenitor and is thus possibly the result of a core-collapse SN explosion.

There is no clear X-ray emission associated with the optical emission from IKT 21. The X-ray emission from the vicinity of the optical remnant is dominated by the Be-pulsar binary system AX J0103-722 (Hughes & Smith 1994; Israel et al. 2000). We extracted our spectrum from the region containing the optical emission, which includes the pulsar system. Although not visible in Fig. 8.4, the spectrum clearly extends above 3 keV. Our model for IKT 21 thus consists of a NEI component for thermal emission from the SNR and a power-law component to account for the pulsar emission. The power-law component normalisation and photon index were initially fixed to values obtained from Hughes and Smith (1994) and were subsequently allowed to vary. The best fit model gives a power-law component normalisation of $\sim 2.2 \times 10^{43}$ phs $^{-1}$ keV $^{-1}$, a photon index of ~ 0.9 and a luminosity of $\sim 5.5 \times 10^{27}$ W(0.5-2.0 keV band). Our results for the thermal emission indicate a temperature of $kT_e \sim 0.58 \pm 0.40$

and a luminosity of $\sim 8 \times 10^{27}$ W (0.5–2.0 keV band). These results compare well with estimates obtained by Hughes and Smith (1994). It is not clear whether the pulsar AX J0103-722 is associated with the SNR as it is not near the centre of the remnant. An association would mean that IKT 21 would be the remnant of a massive-star SN (Hughes and Smith 1994).

IKT 4 has a very similar morphology to IKT 5, DEM S 128 and IKT 25. Its X-ray emission, which peaks in the Fe-L band, lies inside its optical emission. The spectrum is too weak to constrain the abundance, so we cannot speculate on its progenitor based on the spectrum. However, the morphology does argue for a type Ia SN origin.

8.4.2 SMC Abundances

The abundance values for the swept-up matter dominated SNRs (Table 8.4) show some spread among the remnants and also between different elemental species. The general trend is that the larger remnants have lower abundance values while the smaller ones have larger values. The interpretation is that the older remnants have swept-up so much ISM material that the abundances are approaching the ISM values. The abundance yields from the older remnants with larger swept-up masses could thus be used to probe the ISM abundance distribution.

We use the abundances derived from the spectral fits to IKT 6 (outer region), IKT 18 and IKT 23 (outer region) to determine the gas-phase abundances of the SMC. These remnants are selected because of their high (swept-up) masses. We average, for each elemental species, the fitted abundances from the three remnants. In Fig. 8.6 we plot the error weighted average abundances versus elemental species. The uncertainties represent the rms-scatter among the remnants. The derived abundances are also compared to the average SMC abundance values presented by Russel & Dopita (1992). The work of Russel & Dopita (1992) is based on the spectral analysis of F supergiants for heavier elements ($Z > 12$) and H II regions and SNRs for lower Z elements. However, they only have 1 SMC SNR in their studies. Our average abundance values for the low-Z elements appear slightly higher than those obtained by Russel & Dopita (1992), but are in good agreement within the uncertainties.

8.4.3 Physical parameters

The ionisation ages given in Table 8.5 are generally consistent with the dynamical age within a factor 2, the exceptions being IKT 2 and HFPK 149. The factor of 2 difference can be easily explained invoking fragmentary shells or clumping of the X-ray emitting gas. This would increase the electron density and thus reduce the ionisation age estimates. The possibility of fragmentary shells or clumping means that the initial explosion energy E_0 and mass estimates should be regarded as lower and upper bounds respectively.

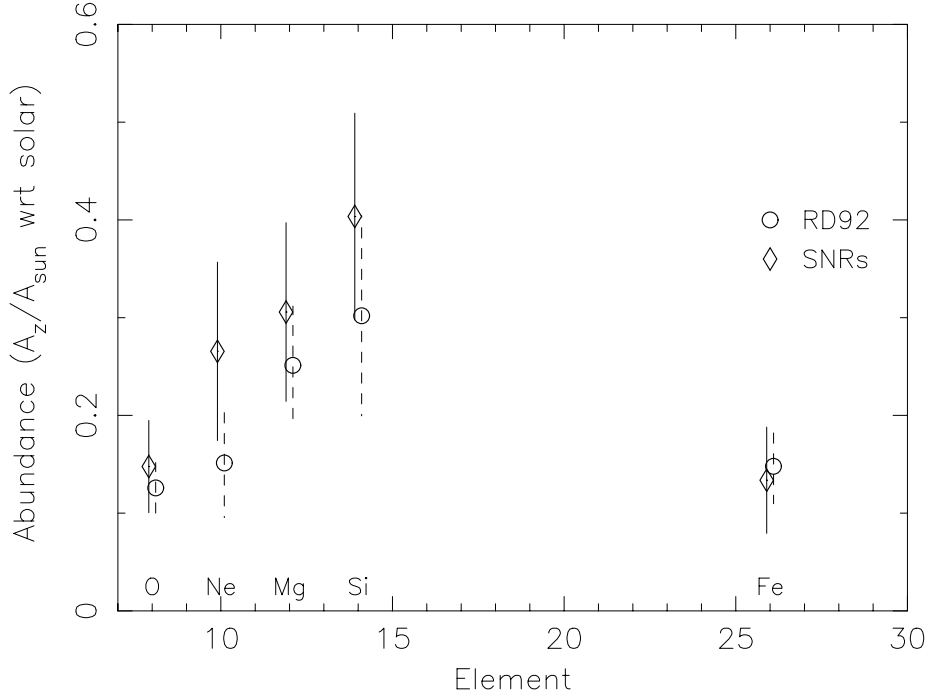


Figure 8.6: Average SMC abundances. The average abundance values obtained from fits to IKT 6, IKT 18 and IKT 23 are represented by diamonds. Results from Russel & Dopita (1992) are indicated with circles.

In the case of IKT 2 and HFPK 149 the plasma has reached ionisation equilibrium. In this regime the ionisation parameter becomes insensitive as an age indicator since the spectrum changes very slowly with increasing ionisation parameter.

The mean SMC ISM hydrogen density derived from the Sedov model fits is $\sim 0.32 \times 10^6 \text{ m}^{-3}$. This is nearly an order of magnitude lower than the mean density of $\sim 1.8 \times 10^6 \text{ m}^{-3}$ derived from Sedov fits to a sample of LMC remnants by Hughes et al. 1998. The lower SMC abundance and densities easily explains the lower SNR luminosities compared to their LMC counterparts, as the X-ray emission scales with the square of the densities. The lower abundances and densities also have implications for the dynamical evolution of SNRs in the SMC. Cox (1972) predicts that the onset of radiative cooling occurs at a time $t_{\text{cool}} = 2.5 \times 10^{-2} E_{44}^{2/11} L^{-5/11} n_{\text{H}}^{-7/11} \text{ yr}$ where E_{44} is the explosion energy in 10^{44} J , L is the cooling coefficient in W m^3 and n_{H} is in m^{-3} .

The onset of radiative cooling will be governed by L and the hydrogen density, since the explosion energies derived from the SMC and LMC samples are similar. L is a strong function of elemental abundance. The SMC/LMC ratio of this coefficient is ≈ 0.6 , assuming average metallicity of 0.2 and 0.35 solar for the SMC and LMC respectively. The lower hydrogen density and metallicity means that the SMC remnants take ~ 4 times longer to reach the radiative cooling stage, compared to the LMC remnants. The SMC remnants should thus be radiating X-rays for a longer time than in the LMC. This point is illustrated by the fact that the oldest remnant in our sample is $\sim 20\,000$ yr while the oldest remnant in the LMC sample analysed by Hughes et al. (1998) is 10 000 yr.

Note that the derived average SMC ISM hydrogen density is even lower if we exclude the results derived from the fits to the IKT 22 spectra. The IKT 22 spectrum is dominated by emission from ejecta material so the Sedov results probably does not represent the ISM density, which is reflected in the larger hydrogen density as compared to the other remnants in our sample.

8.4.4 Comments on SMC SN rates

A number of conflicting SMC SN rate estimates have been made. For example, Mathewson et al (1983) gave a birth rate of one SNR per 800 yr, while Filipovic et al. (1998) gives a birth-rate of one SNR per 350 yr. Both these estimates are higher than a rate of one in every 1100–2500 yr invoked by van den Berg & Tammann (1991), which is derived from the star formation rate inferred from the total $H\alpha$ luminosity of the SMC.

If we follow the arguments from the previous section (Section 8.4.3) then we estimate that the onset of the radiative cooling stage commences at $\sim 30\,000$ yr. Now if we consider that 16 X-ray emitting SNRs have been detected, to date, then the SN rate in the SMC should be closer to one per ~ 1800 yr. This rate is in line with the rate inferred from van den Berg & Tammann (1991). The derived rate is also consistent with our age estimate ($\sim 2\,700$ yr) of the youngest SMC SNR (viz. IKT 22).

Acknowledgements. We thank Jacco Vink for the use of and help with his image processing software and for valuable discussions. The results presented are based on observations obtained with XMM-Newton, an ESA science mission with instruments and contributions directly funded by ESA Member States and the USA (NASA). SRON is supported financially by NWO, the Netherlands Organisation for Scientific Research.

References

- Anders, E., & Grevese, N., 1989, *Geochimica et Cosmochimica Acta*, 53, 197
 van den Berg, S., & Tammann, G., 1991, *ARA&A*, 29, 363

- Blair, W.P., Raymond, J.C., Danziger, J., Matteucci, F., 1989, *ApJ*, 338, 812
- Borkowski, K.J., William, J.L., & Reynolds, S.P., 2001, *ApJ*, 548, 820
- Brickhouse, N. S., Dupree, A. K., Edgar, R. J., et al., 2000, *ApJ*, 530, 387
- Cappellaro, E., Evans, R., & Turrato, M., 1999, *A&A*, 351, 459
- Chu, Y.-H., & Kennicutt, R.C., 1988, *AJ*, 95, 1111
- Cox, D.P., 1972, *ApJ*, 178, 159
- Davies, R.D., Elliot, K.H., & Meaburn, J., 1976, *Royal Astronomical Society, Memoirs*, 81, 89.
- Dickel, J.R., Williams, R.M., Carter, L.M., Milne, D.K., Petre, R., Amy, S.W. 2001, *AJ*, 122, 849
- Draine, B.T., & McKee, C.F., 1993, *ARA&A*, 31, 373
- Filipovic, M.D., Pietsch, W., Haynes, R.F., et al., 1998, *A&ASS*, 127, 119
- Filipovic, M.D., Haberl, F., Pietsch, W., and Morgan, D.H. , 2000, *A&A*, 353, 129
- Haberl, F., Filipovic, M.D., Pietsch, W., & Kahabka, P., 2000, *A&ASS*, 142, 41
- Hayashi, I., 1997, PhD thesis, Graduate School of Science, Kyoto University
- den Herder, J.W., Brinkman, A.C., Kahn, S.M., et al., 2001, *A&A*, 365, L7
- van der Heyden, K.J., Bleeker, J.A.M, Kaastra, J., & Vink, J., 2003, *A&A*, 406, 141
- Hughes, J.P., Smith, R.C., 1994, *AJ*, 107, 1363
- Hughes, J.P., Hayashi, I., Helfand, D.J., et al, 1995, *ApJ*, 444, L81
- Hughes, J.P., Hayashi, I., & Koyama, K., 1998, *ApJ*, 505, 732
- Hughes, J.P., Rakowski, C.E., & Decourchelle, A., 2000, *ApJ*, 543, L61
- Hughes, J.P., Ghavamian P., Rakowski C.E., & Slane, P., 2003, *ApJ*, 582, L95
- Inoue, H., Koyama, K., & Tanaka, Y., 1983, in *IAU Symposium 101, Supernova Remnants and Their X-ray Emission*, ed. P. Gorenstein & J. Danziger (Dordrecht; Reidel), p535
- Israel, G.L., Campana, S., Covino, S., et al., 2000, *ApJ*, 531, L131
- Kaastra, J.S., Mewe, R., & Nieuwenhuijzen, H. 1996, in *UV and X-ray Spectroscopy of Astrophysical and Laboratory Plasmas*, p. 411, eds. K. Yamashita & T. Watanabe, Tokyo, Univ. Ac. Press
- Laming, J. M., 2000, *ApJS*, 127, 409
- Massey, P., Lang, C.C., DeGioia-Eastwood, K., Garmany, C.D., 1995, *ApJ*, 438, 188
- Mathewson, D.S., Ford, V.L., Dopita, M.A., Tuohy, I.R., Long, K.S., & Helfand, D.J., 1983, *ApJS*, 51, 345

- Mathewson, D.S., Ford, V.L., Dopita, M.A., Tuohy, I.R., Mills, B.Y., & Turtle A.J., 1984, ApJS, 551, 189
- Mewe, R., Kaastra, J.S., & Liedahl, D.A., 1995, Legacy 6, 16
- Nazé, Y., Hartwell, J. M., Stevens, I. R., et al., 2002, ApJ, 580, 225
- Nishiuchi, M., 2001, PhD Thesis, Kyoto University
- Nishiuchi, M., Yokogawa, J., Koyama, K., & Hughes J.P., 2001, PASJ, 53, 99
- Nomoto, K., Iwamoto, K., Nakasato N., et al., 1997, Nucl. Phys. A, 621, 467
- Rasmussen, A., Behar, E., Kahn, et al., 2001, A&A, 365, L231
- Russel, S.C., & Dopita, M.A., 1992, ApJ, 384, 509
- Sedov, L.I., 1959, Similarity and Dimensionless Methods in Mechanics (New York:Academic)
- Strüder, L., Briel, U.G., Dennerl, K., et al., 2001, 365, L18
- Truelove, J. K., & McKee, C. F., 1999, ApJS, 120, 299
- Turner, M.J.L., Abbey, A., Arnaud, M., et al., 2001, 365, L27
- Wang, & Q., Wu, X., 1992, ApJS, 78, 391
- Westerland, B.E., 1990, A&ARv, 2, 29
- Woosley, S.E., & Weaver, T.A., 1995, ApJS, 101, 181
- Ye, T., Turtle, A.J., & Kennicutt, R.C., 1991, MNRAS, 249, 722
- Yokogawa, J., Imanishi, K., Koyama, K., Nishiuchi, M., Mizuno, N., 2002, PASJ, 54, 53

Chapter 9

Summary & Outlook

9.1 Synopsis

Supernova remnants are at the nexus of many important, contemporary, astrophysical problems: the late stage of stellar evolution, supernovae, the formation of compact objects, nucleosynthesis, collisionless shocks, particle acceleration and possibly gamma-ray bursts (McKee 2001). High resolution and imaging spectroscopy, as highlighted in this thesis, are invaluable tools in unraveling SNR properties. Spatially resolved spectroscopy with high resolution and throughput, as is available with *Chandra* and *XMM-Newton*, also offers an opportunity to investigate a host of physical effects in greater detail than before.

The intrinsic brightness of the young Galactic SNR Cas A, coupled to the high sensitivity of the solid state (*EPIC-MOS* and *EPIC-pn*) X-ray camera's of *XMM-Newton*, make it possible to perform a detailed, spatially resolved, spectral analysis of the thermal emission of Cas A on a $20'' \times 20''$ pixel scale. The bandwidth (up to 15 keV) offers an unique opportunity to assess the origin of the hard X-ray continuum. Detailed electron temperature, ionisation age and Doppler maps of Cas A have been derived for the first time, providing a wealth of information on the remnant's dynamics and details of the shock heating process. Observations with the *RGS* of SNR B 0540-69.3, N 103B and DEM L 71 in the Large Magellanic Cloud are among the first highly resolved X-ray spectra of SNRs. The capability of the *RGS* for high resolution spectroscopy of sources of moderate angular extent is well matched to the typical angular sizes of SNRs in the LMC. The high dispersion of the RGS allows almost all of the X-ray spectral features emitted by these remnants to be resolved. Detailed spectroscopic modeling permits independent measurements of astrophysical quantities that affect line shape and production, such as electron temperature, density and elemental abundance profiles. Previous X-ray analysis of SNRs in the SMC have been limited to detections

only, except for the bright IKT 22 (SNR 1E0102-72). The large bandwidth and sensitivity of *XMM-Newton* is a crucial aspect for a spectroscopic assesment of SNR properties in the SMC. We presented a synoptic study of 13 SNRs in the SMC. A summary of the work done in this thesis is given in the following subsections.

9.1.1 Cassiopeia A

The hard X-ray continuum maps from XMM-Newton indicate that the 8.0–15.0 keV flux, predominantly due to the previously reported high-energy spectral tail, does not originate from a few localized regions such as X-ray bright knots and filaments, nor does it originate from a limb brightened (fractionary) shell close to the shock front generated by the primary blast wave. Therefore the hard X-ray image does not support the interpretation of the hard X-ray continuum in terms of simple synchrotron emission models. Non-thermal Bremsstrahlung, produced by a population of suprathermal electrons, is a plausible alternative.

Moreover, a recent 500 ks deep observation of the hard X-ray continuum by BeppoSAX has revealed the positive detection of the ^{44}Sc nuclear decay lines at 67.9 and 78.4 keV (Vink et al. 2001). Fitting of the hard X-ray continuum with a non-thermal Bremsstrahlung model yielded an initial ^{44}Ti mass of $(0.8 - 2.5) \times 10^{-4} M_{\odot}$. This implies a progenitor mass of $\sim 30 M_{\odot}$. The relatively high ^{44}Ti abundance can also be explained by one of the few available SN Type Ib models of a star with a ZAMS mass of $60 M_{\odot}$ (Woosley et al. 1993) that suffered significant wind-loss before explosion. The abundance ratios obtained from the XMM-Newton analysis are also more consistent with ratios predicted by this particular model (see Fig. 9.1) than the yields from lower mass stars.

The tight correlation between the variation in abundance of Si, S, Ar, Ca over an absolute abundance range of two orders of magnitude is strong evidence for the nucleosynthesis of these ejecta elements by explosive O-burning and incomplete explosive Si-burning due to the shock heating of these layers in the core collapse supernova. However the Fe emission, both in the Fe-K and the Fe-L lines, does not show this correlation. A significant fraction of the Fe-K emission is seen at larger radii than Si-K and S-K as convincingly demonstrated in our Doppler derived 3-D reprojection. The 3-D reprojection also shows a largely bi-polar distribution of the Fe-K emission which may indicate that the original explosion was aspherical, possibly with axial symmetry. Willingale et al. (2003) performed further analysis of the X-ray spectroscopy results obtained in chapter 4. They derived the differential mass distribution as a function of ionisation age for the hot and cool X-ray emitting components. They calculate a swept up mass of $7.9 M_{\odot}$ in the emitting plasma and estimate that the total mass lost from the progenitor prior to the explosion could be as high as $\sim 20 M_{\odot}$. This is in agreement with the $60 M_{\odot}$ plus wind-loss model.

Maeda & Nomoto 2003 recently examined the hydrodynamics and explosive nucleosynthesis in bipolar supernova explosions to account for peculiar properties of hyper-

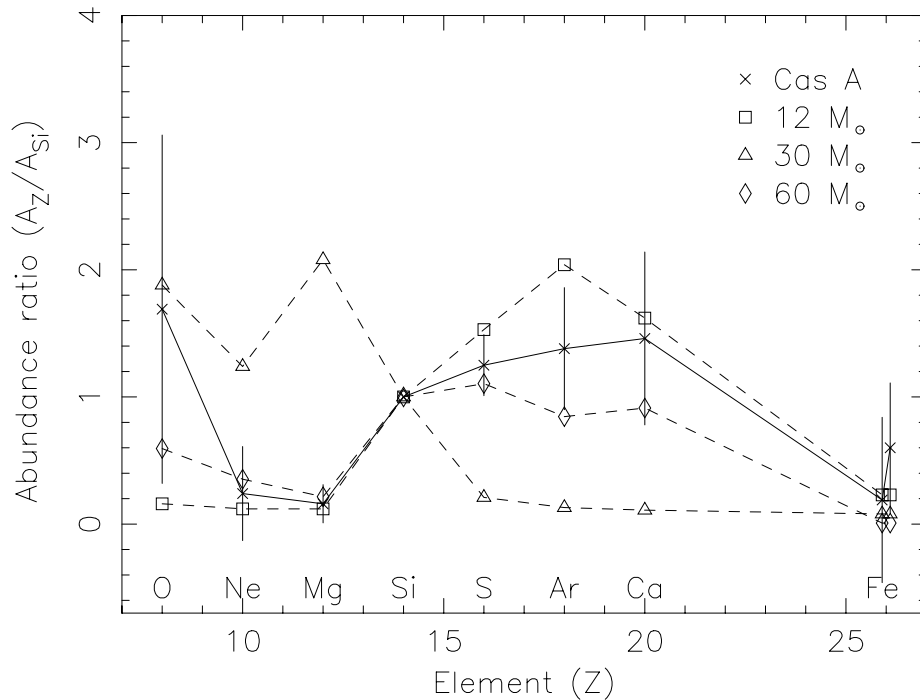


Figure 9.1: Mean measured Cassiopeia A abundance ratios (crosses) and rms scatter compared with theoretical predictions for progenitor masses of 12 (square), 30 (triangle) and 60 M_{\odot} (including wind-loss) (diamond). Abundance values for the 12 and 30 M_{\odot} progenitors are taken from Woosley & Weaver (1995), while those for the 60 M_{\odot} progenitor are taken from Woosley et al. (1993).

novae. In bipolar models the Fe-rich materials are ejected at high velocities along the jet axis, while O-rich material occupy the central region. They also found that ejected isotopes are distributed as follows in order of decreasing velocities: ^{64}Zn , ^{59}Co , ^{56}Fe , ^{44}Ti and ^{64}He at highest velocities, ^{55}Mn , ^{52}Cr , ^{32}S and ^{28}Si at intermediate velocities and ^{24}Mg and ^{16}O at the lowest velocities. Our Fe-K, Si and S velocity profiles are in line with this model. Determining the O velocity and morphology from the present X-ray data is, however, difficult. There are indications in *RGS* data that the O emission morphology differs from that of Si, S and Fe-K, but a detailed comparison will only be possible from observations with future missions such as *XEUS* and *Constellation-X*.

9.1.2 The LMC SNRs

SNR B 0540-69.3 is regarded as the LMC counterpart of the Crab Nebula. No clear emission corresponding to the shock advancing through ejecta has been detected in the Crab Nebula and thus no significant ejected mass or energy from the original explosion has been measured. The detection of the X-ray line emission emanating from the shell makes SNR B 0540-69.3 an important object for studying the link between young energetic pulsars and massive stars that form them in core collapse SNe. This work also highlights the capability to infer the spatial location of the line emitting source from the *RGS* data.

Identifying the explosion type of a supernova remnant, i.e. between thermonuclear (type Ia) and core-collapse (type II, Ib & Ic) is important, but is not always straightforward. Distinction between thermonuclear and core-collapse SNe can be made on the basis of the nucleosynthesis products of these explosions. Type Ia explosions produce Fe rich ejecta material, while core-collapse SNe produce ejecta material which is enhanced in O, Ne and Mg. The absence of features from these elements in a previous *ASCA* observation led to this remnant being designated as the result of a type Ia SN explosion. The presence of O, Ne and Mg emission lines in the *RGS* data suggest that N 103B might actually be the result of a type II SNe. Indeed, the abundance patterns obtained from our model fits agree more closely to those of a type II SN. The absolute O mass is also higher than predicted by type Ia SNe models, while the Fe mass is much lower than would be expected if N 103B was the result of a type Ia SN.

The analysis of DEM L 71 presented in chapter 7, indicates that the rim emission represents a blast wave moving out into the ISM, while the interior emission is from Fe-rich stellar ejecta material. The morphology, mass estimates and abundances strongly suggest that DEM L 71 is the result of a type Ia supernova explosion.

RGS single ion analysis shows that temperature and ionisation age variations exist in DEM L 71. This is evident from the difference in morphology between the O VII forbidden and resonance lines. These lines show an anomalously high ratio ($f/r \sim 1.2$) along the eastern rim of the remnant. This ratio could imply that the plasma is cooling and recombining in this region. However, an alternative, and equally interesting, possibility is that the variation in f/r ratios is due to resonance scattering, which would reduce the O VII- r line emission along lines of sight with a high O VII column density. We could not distinguish between the effects of resonance scattering and recombination because we were unable to extract spatially resolved spectra from the rims and central region. However, a *RGS* observation has now been scheduled, which will allow us to extract spectra from the rims and central region. Having access to a broader spectral range will allow us to easily distinguish between the effects of recombination and resonance scattering. A recombination X-ray spectrum would be interesting, as radiative shocks are not normally expected to be important in relatively young (or Sedov phase) remnants, such as DEM L 71. The detection of resonance scattering, on the other hand, will add weight to the argument that this process could

be important in SNRs.

DEM L71 is an important object to study in order to discriminate between the various type Ia supernovae models (e.g. Nomoto et al. 1997), since we see the Fe rich ejecta nested inside the outer shell. Deeper observations will facilitate the search for, among other things, Ar and Ca emission. The measurement of the Si/Fe, S/Fe, Ar/Fe and Ca/Fe mass ratios would be useful to distinguish the type Ia models (see Table 2.1; Nomoto et al. 1997). The identification of type Ia SN progenitor evolution is important for understanding the origin of some systematic variations of light curves, which is critical for the determination of cosmological parameters, H_0 and q_0 .

9.1.3 The SMC SNRs

We performed X-ray spectral analysis of 13 SNRs in the SMC. IKT 6, IKT 22 (SNR 1E 0102-72) and IKT 23 are oxygen rich remnants which are most likely the result of type II SNe. They represent very different ages (~ 2000 – 19000 yr) and studying these remnants in more detail presents a unique opportunity to probe the evolution of oxygen-rich remnants in the SMC. We also designate a core collapse origin to DEM S 32, IKT 2, HFPK 419, IKT 16 and IKT 21. The spectra and derived abundance profiles suggest that the remaining four remnants, viz. IKT 4, IKT 5, DEM S 128 and IKT 25, have type Ia SNe progenitors. An interesting point to note is that the ejecta material is still visible in many older remnants.

The mean SMC ISM hydrogen density derived from the Sedov model fits is $\sim 0.32 \times 10^6 \text{ m}^{-3}$, which is much lower than the corresponding LMC value of $\sim 1.8 \times 10^6 \text{ m}^{-3}$, inferred by Hughes et al. 1998. The lower density not only accounts for the lower SNR luminosities observed in the SMC, but also implies that SNR evolution proceeds at a slower rate as compared to remnants in the LMC. This might be one of the reasons why we still see emission from ejecta material in many of the more evolved SMC remnants. Our estimate of the mean SMC gas-phase elemental (O, Ne, Mg, Si and Fe) abundances are in agreement with the estimate of Russell & Dopita 1992.

This work illustrates how SNRs can be used to probe conditions in external galaxies. The ability to designate SN explosion types to SNRs have important consequences in the study SNe rates and star formation histories. The progenitors of the various types of SNe evolve on different timescales and thus contribute to the chemical enrichment at different stages of galactic evolution. Type II and type Ib/Ic SNe cause the heavy-element enrichment in the early phase of galactic evolution because the lifetime of their massive progenitors ($\sim 10^{6-7}$ yr) are much shorter than the age of their host galaxies. In contrast, type Ia supernovae produce heavy elements on a much longer time scale and contribute to the chemical enrichment in the later phase of galactic evolution.

9.2 Outlook

The combination of high spectral and 2D-spatial resolution is the holy grail of future X-ray astrophysical missions. Micro-calorimeters are (currently) the best option as detector technology to achieve this. The Japanese *Astro-E2* observatory will be the first to launch this technology. The microcalorimeters used in the X-ray Spectrometer (*XRS*) aboard *Astro-E2* have a spectral resolution of ~ 10 eV over the 0.4–10 keV energy band. It will measure the spectrum of celestial objects in the X-ray range 0.2–10 keV to ~ 10 times better than current solid-state detectors, but will have a spatial resolution of only $\sim 2'$. The X-Ray Evolving Universe Spectroscopy mission (*XEUS*) and *Constellation-X*, which could be launched in the next decade, will be more suited for high resolution spatially resolved spectroscopy. *XEUS*, for example, will be 200 times more sensitive than *XMM-Newton*. The spatial resolution of the *XEUS* optics should be of order $2''$ and the microcalorimeters are expected to provide a spectral resolution of 1–2 eV.

The analysis of Cas A with the solid state (*EPIC-MOS* and *EPIC-pn*) X-ray camera's of XMM-Newton (chapter 4) shows the power of medium resolution spatially resolved spectroscopy. A similar analysis at $2''$ spatial and 1–2 eV spectral resolution, however, has distinct advantages. Firstly, an analysis could be done on a spatial scale comparable to the size of the individual knots and filaments seen in the high resolution *Chandra* image (Fig. 9.2). A simulated *XEUS* spectrum for a typical bright knot ($3'' \times 3''$) is displayed in Fig. 9.2. Individual emission lines would be well resolved, as opposed to the blended line complexes seen in the *EPIC* data. Doppler velocities can therefore be measured directly (down to tens of km s^{-1}), and in a model independent way, by comparing the emission line centroids to the expected laboratory wavelengths. Velocity profiles will not be limited to the strongest line complexes (viz Si, S and Fe-K), but Doppler velocities can potentially be measured from emission lines of various ionized elemental species ranging from C through Ni. The abundances could be determined to much higher accuracy. The whole analysis procedure can be done on a smaller grid size ($\sim 3'' \times 3''$) giving much higher spatially resolved velocity, elemental abundance, temperature and ionisation maps.

Various SN models exist that predict distinct kinematics and explosive nucleosynthesis products. For example, Kifonidis et al. (2003) predict that dense “bullets” and clumps of Ni, Si and O-rich material propagate ballistically following the core collapse SN explosion. They also predict different metal velocities in the remnants of type II and Ib SNe. Models for asymmetric explosions by Maeda & Nomoto (2003) also give different velocity profiles for different elements. Measuring the kinematics and nucleosynthesis products will help to discriminate between different type Ia models (e.g. Nomoto et al. 1997; Iwamoto et al. 1999). The combination of elemental velocity profiles and abundances will be extremely useful to investigate SN progenitor evolution, explosion energy and nucleosynthesis.

The high throughput of future missions will allow for the observations of fainter

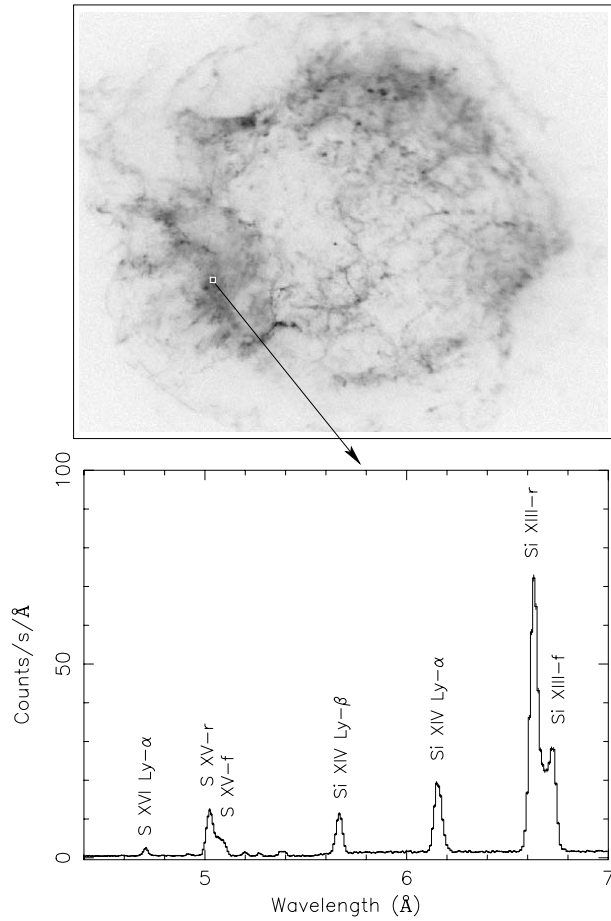


Figure 9.2: A high spatial resolution *Chandra* image of Cassiopeia A. The white box is a $3'' \times 3''$ region around one of the (many) knots seen in the image. A simulated, 10ks exposure, *XEUS* spectrum for such a $3'' \times 3''$ region is shown below. The quality and resolution of the spectrum will potentially allow for the measurement of Doppler velocity shifts of $\gtrsim 20 \text{ km s}^{-1}$. Only a small part of the entire spectrum is shown to highlight the diagnostic capabilities for the elements Si and S.

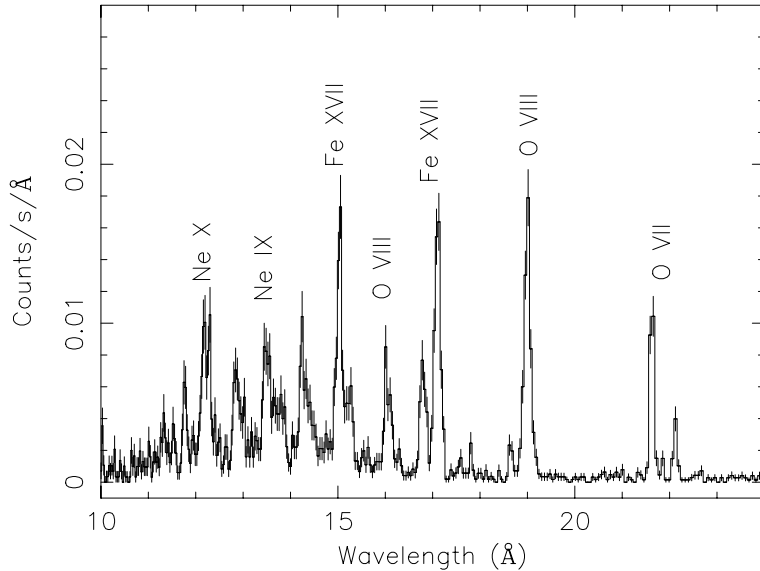


Figure 9.3: A simulated, 100 ks exposure, *XEUS* spectrum of the SNR N 103B placed at the distance of the Virgo cluster (20 Mpc).

objects. An obvious next step then would be to study objects in external galaxies, beyond the Magellanic Clouds. The abundances of elements can be measured from observations of SNRs in Local Group galaxies. Even at the distance of the Virgo cluster (see Fig. 9.3), spatially resolved spectroscopy of galaxies will allow for the determination of temperature and chemical composition of SNRs and the ISM.

Physical processes connected to shock heating by collisionless shocks are also an important topic that can be addressed with high resolution spectroscopy. The electron-ion thermal equilibration is one of the major uncertainties in the physics of strong collisionless shocks. A 1 eV spectral resolution would allow one to measure ion temperatures $\gtrsim 7$ keV, from the thermal Doppler broadening of emission lines. Other physical processes affecting line shape and production that are likely to be important, e.g. resonance scattering and charge exchange, could be studied in much greater detail.

References

- Hester, J.J., Scowen, P.A., & Sankrit, R., et al., 1995, *ApJ* 448, 240
 Hughes, J.P., Hayashi, I., & Koyama, K., 1998, *ApJ*, 505, 732

- Iwamoto, K., Brachwitz, F., & Nomoto, K. et al., F. 1999, ApJS, 125, 439
- Kifonidis, K., Plewa, T., Janka, H.-Th., & Müller, E., 2003, A&A, 408, 621
- McKee, C.F., 2001, in Young Supernova Remnants, ed S.S. Holt, & U. Hwang, (AIP), p. 17
- Maeda, K., & Nomoto, K., 2003, astro-ph/0304172
- Nomoto, K., Yamaoka, H., Shigeyama, T., Kumagai, S., & Tsujimoto, T. 1994, in Supernovae (Les Houches, Session LIV), ed. S. Bludman et al., (Elsevier Sci. Publ.), p. 199
- Nomoto, K., Hashimoto, M., & Tsujimoto, T., et al., 1997, Nucl. Phys.A, 621, 467
- Russell, S.C., & Dopita, M.A., 1992, ApJ, 384, 508
- Vink, J., Laming, J.M., Kaastra, J.S., Bleeker, J.A.M., Bloemen, H., 2001, ApJ, 560, L79
- Willingale, R., Bleeker, J.A.M., van der Heyden, K.J., & Kaastra, J.S., 2003, ApJ, 398, 1021
- Woosley, S.E., Langer, N., & Weaver, T.A., 1993, ApJS, 411, 823
- Woosley, S.E., & Weaver, T.A., 1995, ApJS, 101, 181

Hoofdstuk 10

Nederlandse Samenvatting

10.1 Supernova's en Supernovarestanten

Vanaf de tweede eeuw na Christus registreerden Chinese astronomen zogenaamde “gaststerren”. Dit waren objecten die plotseling aan de hemel verschenen, zichtbaar waren gedurende een korte tijdsspanne en daarna langzaam verdwenen. De “gaststerren” die gedurende een jaar of langer zichtbaar waren, waren waarschijnlijk supernova's. Supernova's zijn enorme explosies die hele sterren uit elkaar rukken. Supernova's behoren tot de meest energetische explosies in de kosmos. 99 % van de energie die bij de explosie vrijkomt, wordt in de vorm van subatomaire deeltjes, bekend onder de naam neutrino's, uitgestraald. De resterende één procent, ongeveer 10^{44} Joule (dit komt overeen met 10^{28} kernbommen), wordt omgezet in mechanische energie. Wanneer een ster een supernova wordt, stijgt zijn helderheid met meer dan een factor honderd miljoen, waarna het licht langzaam zwakker wordt. De explosie is zo helder dat het supernova alle sterren in het betreffende melkwegstelsel overstraalt.

Supernova's worden verdeeld in twee fundamentele fysische types. Het type Ia is het eindproduct van sommige dubbelstersystemen met een rode reus en een witte dwerg. In een dergelijk systeem stroomt massa van de rode reus naar de witte dwerg. Uiteindelijk stapelt zich zoveel massa op de witte dwerg dat deze onder het gewicht ineenstort. Tijdens het instortingsproces loopt de temperatuur zo hoog op dat koolstof- en zuurstoffusie in de ster kan optreden en een onstabiel thermonucleair proces in gang wordt gezet. Hierbij ontstaat een “ontbrandingsgolf”, d.w.z. een explosie die zich ontwikkelt zonder te zijn gestart door een schokgolf. De “ontbrandingsgolf” plant zich in enkele seconden voort door de kern. Tengevolge van kernfusie ontstaat hierbij ongeveer één zonsmassa aan radioactief nikkel dat later weer vervalt tot ijzer.

Type II supernova's zijn zware sterren die aan het eind van hun leven ineenstorten. Aan het eind van zijn leven is een zware ster opgebouwd uit lagen materiaal, zoals

schillen bij een ui. De centrale kern bestaat uit ijzer, deze wordt omgeven door een schil bestaande uit zwavel en silicium, daarom heen ligt weer een schil van neon en zuurstof, en vervolgens de buitenste lagen van koolstof, helium en waterstof. Doordat in de ijzerkern het fusie proces stopt, heeft de ster geen energiebron meer om de zwaartekracht te weerstaan. De ster stort in en bereikt in enkele milliseconden dichtheden vergelijkbaar met die in atoomkernen. Alleen de afstotende kracht tussen kerndeeltjes kan de instorting stoppen zodat er zich vanuit de kern een buitenwaarts gerichte schokgolf ontwikkelt. Door deze schokgolf wordt het ster materiaal in de buitenlagen verhit waardoor opnieuw kernfusie mogelijk is, waarbij vervolgens nieuwe elementen en radioactieve isotopen worden gevormd. Dit proces wordt explosieve nucleosynthese genoemd. Door de schok wordt het materiaal van de ster weg geslingerd in de omliggende interstellaire ruimte. Het stellaire overblijfsel in de kern wordt een neutronenster of een zwart gat.

Zoals gezegd wordt in beide types van explosie nieuwe materiaal gevormd tengevolge van kernfusie. In thermonucleaire supernova's bestaat dit hoofdzakelijk uit ijzerrijk materiaal, bij supernovae van het tweede type (kernineenstorting bij zware sterren) wordt er een grote hoeveelheid zuurstof, neon en magnesium geproduceerd. Deze twee types explosie (type Ia en II) kunnen dus onderscheiden worden door de waargenomen nucleosynthese producten.

Een supernovarestant is het overblijfsel van een supernova explosie. Supernovas en supernovarestanten zijn belangrijke objecten omdat zij een grote invloed hebben op de ecologie en de energie huishouding van melkwegstelsels, dus ook op ons eigen Melkwegstelsel. Het gas dat de ruimte tussen sterren vult wordt het interstellaire medium genoemd. Op plaatsen in een melkwegstelsel waar het interstellaire medium een grote dichtheid heeft, kan het gas instorten en brokken vormen. De brokken die een bepaalde kritische massa teboven gaan zullen sterren vormen en kernfusie op gang brengen. De ineerstorting van deze brokken wordt gedreven door de zwaartekracht. Hierdoor wordt de chemische samenstelling van het interstellaire medium de chemische samenstelling van de volgende generatie sterren. Alle elementen zwaarder dan boor worden gemaakt in een ster of in een supernova explosie. De supernova ontploffing mengt supernova-ejecta, met inbegrip van de onlangs gevormde elementen, met het interstellaire medium. Supernovarestanten verrijken dus het interstellaire medium met zware elementen ("sterstof") en dus ook de volgende generatie sterren. Zodoende kan ons zonnestelsel met zijn rotsachtige planeten (zoals de aarde), nooit gevormd zijn zonder voorafgaande supernova explosies.

Naast het verrijken van onze Melkweg met zwaardere elementen, voegen de supernovarestanten heel wat energie aan het interstellaire medium toe. Door een supernova explosie plant zich een drukgolf naar buiten voort, die vervolgens een groot volume van het interstellaire medium opveegt. Het interstellaire medium wordt op twee verschillende manieren beïnvloed: de drukgolf verhit het gas dat het ontmoet, zodat de temperatuur van het interstellaire medium wordt verhoogd. Supernovarestanten spelen dus een belangrijke rol bij de energiebalans van een melkwegstelsel. De drukgolf

versnelt daarnaast elektronen, protonen en ionen tot snelheden nabij de lichtsnelheid. Dit verschijnsel is zeer belangrijk, omdat de oorsprong van de kosmische straling een van de grote onopgeloste problemen in de astrofysica is. De meeste astronomen denken dat bijna alle kosmische straling in onze Melkweg deel uitmaakt van het interstellair medium, en ooit door een supernova drukgolf versneld werden. Door afwisselend over drukgolf aan beide kanten te passeren, winnen deze deeltjes energie en worden kosmische straling. Dit deeltjesversnellingsproces staat bekend als Fermi versnelling. Toch is het nog niet duidelijk tot welke maximum energie supernovarestanten kosmische straling kunnen versnellen.

10.2 Dit proefschrift: Röntgenstraling van supernovarestanten

De schok die door de supernova wordt gevormd, verhit het omringende interstellair medium en het materiaal dat in de supernova ontploffing wordt uitgestoten tot temperaturen boven de 10^7 K. Bij deze hoge temperaturen straalt het door de schok verwarmde gas in het röntgengebied van het spectrum. Het is daarom belangrijk om deze objecten in het röntgen golflengtegebied te bestuderen.

Sinds de ontdekking van kosmische röntgenstraling in 1962 is het vakgebied snel gegroeid, voor een belangrijk deel door de steeds grotere gevoeligheid van röntgen instrumentatie. De recente lancering van de *Chandra* (juli 1999) en *XMM-Newton* (december 1999) observatoria hebben een nieuw tijdperk in de röntgen-sterrenkunde ingeluid. Zij zijn de krachtigste röntgentelescopen die ooit in een baan om de aarde werden geplaatst en hebben de mogelijkheid om een grote verscheidenheid aan fysische eigenschappen via spectroscopisch onderzoek te bestuderen.

De traliespectrometers van deze observatoria scheiden röntgenlicht van individuele bronnen in een gedetailleerd spectrum. De Reflectie Tralie Spectrometer (*RGS*) van *XMM-Newton* is bijzonder geschikt voor de studie van supernovarestanten. Het gemeten spectrum, dat zich tussen röntgen golflengten van 5 Å tot 38 Å uitstrekt (vergelijk: het zichtbare licht ligt tussen 4000 Å en 8000 Å), toont een gedetailleerde “vingerafdruk” van het zeer hete gas. Elk element zendt heel specifieke spectraallijnen uit. De analyse van deze spectra levert informatie over de temperatuur, de druk, de chemische samenstelling en de snelheden in supernovarestanten.

In dit proefschrift zijn de hoge gevoeligheid en de spectrale resolutie, die bereikt worden met de instrumenten van *XMM-Newton*, specifiek benut om de fysische eigenschappen en dynamica van supernovarestanten te bestuderen. De hoge resolutie van de *RGS* laat toe dat bijna elke röntgenspectraallijn die door deze restanten wordt uitgezonden, kan worden opgelost. De gedetailleerde spectroscopische modellering laat onafhankelijke metingen toe van astrofysische grootheden die de lijnvorm en productie bepalen, zoals elektronentemperatuur, dichtheid en element-abondanties. Deze diagnostiek was niet mogelijk met eerdere instrumenten met lagere spectrale resolutie.

De intrinsieke helderheid van het jongste Galactische supernovarestant Cassiopeia A (Cas A), gekoppeld met de hoge gevoeligheid van de vaste stof sensoren (*EPIC-MOS* en *EPIC-pn*) van *XMM-Newton*, maakt het mogelijk om een gedetailleerde, ruimtelijk opgeloste spectrale analyse van de thermische emissie van Cas A op een $20'' \times 20''$ pixelschaal uit te voeren. De bandbreedte (tot 15 keV) biedt een unieke kans om de oorsprong van het eerder gevonden harde röntgencontinuum te onderzoeken. De gedetailleerde elektronentemperatuur, de ionisatieleef tijd en de Dopplerkaarten zijn hier voor Cas A voor het eerst afgeleid. Deze verstrekken een rijkdom aan informatie over de dynamica van deze restant en details over het schokverhittingsproces. Het werk dat in hoofdstuk 4 wordt behandeld toont een sterke correlatie tussen de variatie in abundanties van Si, S, Ar, Ca over een absoluut abundantiebereik van twee ordes van grootte. Dit is sterk bewijsmateriaal dat nucleosynthese van deze ejecta het resultaat is van explosieve zuurstofverbranding en onvolledige explosieve siliciumverbranding van dit gas tijdens het instorten van de kern. Daarentegen vertoont de emissie van ijzer deze correlatie niet. Een significante fractie van de Fe-K emissie is zichtbaar op grotere afstanden van het centrum dan Si-K en S-K. Dit is overtuigend aangetoond in onze Doppler afgeleide 3-D herprojectie. 3-D herprojectie toont ook een grotendeels tweepolige verdeling van de Fe-K emissie, dit kan erop wijzen dat de originele explosie asymmetrisch was (niet-sferisch).

De waarnemingen met de *RGS* van SNR B 0540-69.3, N 103B en DEM L 71 in de Grote Magelhaense Wolk behoren tot de eerste röntgen spectra van supernovarestanten met hoge spectrale resolutie. Het vermogen van de *RGS* voor hoge resolutie spectroscopie van bronnen met een zekere hoekgrootte past goed bij de typische hoekgrootte van supernovarestanten in de Grote Magelhaense Wolk. Een eerdere waarneming met de Japanse *ASCA* satelliet leidde tot de conclusie dat N 103B het resultaat is van een SN explosie van type Ia, door het ontbreken van zuurstof, neon en magnesium emissie in de gemeten lage resolutie CCD-spectra. Explosies van type Ia produceren ejecta rijk aan ijzer, terwijl ejecta van een type II supernova een overvloed geeft aan zuurstof, neon en magnesium zoals reeds gemeld in de vorige paragraaf. De aanwezigheid van emissielijnen van zuurstof, neon en magnesium in het *RGS* spectrum toont dus aan dat N 103B hoogstwaarschijnlijk het resultaat van een type II SN is. De absolute massa van zuurstof is ook hoger dan voorspeld door modellen van type Ia SN, terwijl de massa van ijzer veel lager is dan verwacht zou worden als N 103B het resultaat is van een type Ia SN.

De analyse van DEM L 71 die in hoofdstuk 7 wordt behandeld, wijst erop dat de emissie van de rand veroorzaakt wordt door een schokgolf die zich door het interstellair medium beweegt. De emissie binnen deze rand bevat stellair ejecta die rijk zijn aan ijzer. De morfologie, de massaschattingen en de overvloed aan ijzer geven sterk aanwijzingen dat DEM L 71 het resultaat is van een type Ia supernova explosie.

Röntgenanalyse van supernovarestanten in de Kleine Magelhaense Wolk was tot nu toe tamelijk beperkt, met uitzondering van de heldere bron IKT 22 (SNR 1E 0102-72). De grote bandbreedte en de gevoeligheid van *XMM-Newton* zijn een noodzakelijke

voorwaarde voor een spectroscopische bestudering van de eigenschappen van supernovarestanten in dit dwergmelkwegstelsel. Wij hebben een synoptische spectrale studie van 13 supernovarestanten in de Kleine Magelhaense Wolk uitgevoerd. Zij vertegenwoordigen zeer verschillende leeftijden ($\sim 2000\text{--}19000$ jaar) en het bestuderen van deze restanten in meer detail biedt een unieke kans om de evolutie van zuurstofrijke supernovarestanten in de Kleine Magelhaense Wolk te bestuderen. Wij concluderen dat DEM S 32, IKT 2, HFPK 419, IKT 16 en IKT 21 een kernineenstorting als oorsprong hebben. Voor IKT 5, DEM S 128 en IKT 25, wijzen de spectra en de afgeleide abundantieprofielen op SN type Ia. De gemiddelde waterstofdichtheid in het interstellair medium van de Kleine Magelhaense Wolk die uit de analyse wordt afgeleid is $\sim 0.32 \times 10^6 \text{ m}^{-3}$, welke veel lager is dan de overeenkomstige waarde voor de Grote Magelhaense Wolk van $\sim 1.8 \times 10^6 \text{ m}^{-3}$. De lagere dichtheid verklaart de lagere helderheid van supernovarestanten in de Kleine Magelhaense Wolk, en impliceert ook dat de evolutie van supernovarestanten langzamer is in vergelijking tot supernovarestanten in de Grote Magelhaense Wolk.

Curriculum Vitae

I was born on 30 October 1971 in Kimberley, South Africa. I completed my secondary education at William Pescod Senior Secondary School in 1989. I obtained a BSc. degree in physics from the University of South Africa in 1996 and completed my BSc honours year at the University of Cape Town in 1997. Here I did a mini-project measuring the lifetime of an excited state of Neptunium-237 which results from the alpha decay of Americium-241. In 1998 I switched to astronomy and took up a MSc position at the South African Astronomical Observatory under the guidance of Dr. D. Buckley and promotorship of Prof. B. Warner (UCT). The topic of my thesis was optical spectroscopic studies of magnetic cataclysmic variables. The work involved searching for cyclotron features and doing Doppler tomographic imaging of these systems.

I began my PhD. studies at the SRON National Institute for Space Research in February of 2000. My work involved the X-ray spectroscopic study of Supernova Remnants and the work was done under the supervision of Dr. J.S. Kaastra and Prof.Dr.Ir. J.A.M Bleeker. This thesis is the culmination of 4 years of research done at SRON.

I was afforded the opportunity to attend a number of conferences and workshops over the duration of my PhD. studies. I gave talks at conferences held in Noordwijk (Netherlands), Houston (USA) and a workshop held at the Mullard Space Science Laboratory (UK). I also attended a conference in Palermo (Sicily) and presented posters presentations in Minneapolis (USA) and Valencia (Spain).

Acknowledgements

This thesis is not only the culmination of four years of my own work, but is also due, in no small part, to the interaction, assistance and friendship of many people. I take this opportunity to thank them.

Ik dank in eerste instantie mijn promotor Prof. Dr. Ir. J.A.M. Bleeker en copromotor Dr. J.S. Kaastra voor hun begeleiding bij dit project.

Ik dank J.W. den Herder en W. Hermsen voor de steun en kansen zij me gaven (wetenschappelijk, administratief en anders). Ik uit mijn dank aan de *RGS* groep, waarin ik onschatbare ervaringen opdeed, en de mogelijkheid gaf om met bekwame en gemotiveerde mensen samen te werken. In bijzonder dank ik: Bert Brinkman, Jacco Vink, Cor de Vries, Takayuki Tamura, Jelle de Plaa, Rolf Mewe, Ton den Boggende, Ton Raassen en Mariano Mendez. Aan mijn kamergenoot, Katrien Steenbrugge dank voor alle gesprekken en het helpen met de Nederlandse (of eerder Vlaamse) vertaling van mijn thesissamenvatting. Dank ook aan Joeri van Leeuwen, Rémon Cornelise en Eric van der Swaluw.

Ik dank Liddy Negenborn en Gerjo Pijpers voor het helpen om vergaderingen met een altijd drukke Johan op te zetten en voor hun hulp in invullen van allerlei bescheiden nodig voor het behalen van dit diploma.

I thank our (international) *RGS* consortium group colleagues for their help and interaction, especially : Frits Paerels, Steve Kahn, Jean Cottom, Andy Rasmussen, Ehud Behar, John Peterson, Graziella Branduardi-Raymont, Manuel Güedel and Mark Ardaud.

While the quality of my work is ultimately only judged on the science, if I was not able to adapt to this new country then this thesis would certainly not have materialised. For their friendship and help in adapting to life in the Netherlands we thank the following people. Ronald & family; Rob, Bernadette & kids; Taka & Erico; and the mafiosos Giuseppe and Carlo.

A special thanks to my wife and daughters: Colleen and Kirsten (and recent addition Chelsea) I dearly appreciate all the support you gave and the sacrifices you made, even if you might not see it this way.

I am grateful for the financial support received from NWO, NRF, SRON and Leids Kerkhoven-Bosscha Fonds.